

# MeteorNews

ISSN 2570-4745

VOL 7 / ISSUE 3 / MAY 2022



*December psi Cassiopeiid fireball recorded at  $22\text{h}39\text{m}04.4 \pm 0.1\text{s}$  UTC on 2021 November 28 from the SWEMN meteor-observing stations located at La Hita, La Sagra, Calar Alto, Sevilla, Huelva, and Sierra Nevada, Spain. It reached a peak absolute magnitude of  $-12 \pm 1$ . Read more about this meteor shower and the Andromedid complex in this issue.*

- Andromedid complex
- CAMS reports
- Meteor light curves
- New meteor showers
- Fireballs
- Radio meteor work

# Contents

2021 Andromedid complex by Global Meteor Network <i>P. Roggemans, P. Cambell-Burns and D. Vida</i> .....	159
A statistical analysis of BRAMON TV meteors light curve data obtained in 2014 and 2015 <i>A. S. Betzler and O. F. de Sousa</i> .....	181
Discovery of a shower associated with comet 197P/LINEAR in UKMON Meteor Orbit Data <i>J. Greaves</i> .....	188
A potential new summer shower in Lacerta <i>J. Greaves</i> .....	195
The Southwestern Europe Meteor Network: development of new artificial intelligence tools and remarkable fireballs observed from January to February 2022 <i>J. M. Madiedo, J. L. Ortiz, J. Izquierdo, P. Santos-Sanz, J. Aceituno, E. de Guindos, P. Yanguas, J. Palacián, A. San Segundo, D. Ávila, B. Tosar, A. Gómez-Hernández, J. Gómez-Martínez and A.I. Aimee</i> .....	199
February 2022 report CAMS BeNeLux <i>C. Johannink</i> .....	209
March 2022 report CAMS BeNeLux <i>C. Johannink</i> .....	211
Radio meteors February 2022 <i>F. Verbelen</i> .....	213
Radio meteors March 2022 <i>F. Verbelen</i> .....	219

# 2021 Andromedid complex by Global Meteor Network

Paul Roggemans<sup>1</sup>, Peter Cambell-Burns<sup>2</sup> and Denis Vida<sup>3</sup>

<sup>1</sup> Pijnboomstraat 25, 2800 Mechelen, Belgium

paul.roggemans@gmail.com

<sup>2</sup> UKMON, Cavendish Gardens, Fleet, Hampshire, United Kingdom

peter@campbell-burns.com

<sup>3</sup> Department of Earth Sciences, University of Western Ontario, London, Ontario, N6A 5B7, Canada

denis.vida@gmail.com

A study of the 2021 Andromedids is presented based on the Global Meteor Network results. Andromedid orbits were identified during the interval in solar longitude  $206^\circ$  to  $278^\circ$ . Although rates were very low, three intervals with enhanced activity could be distinguished, a first dispersed at  $\lambda_\odot \sim 234^\circ$ , a second more compact at  $\lambda_\odot \sim 239.4^\circ$  and a final short enhancement at  $\lambda_\odot \sim 246.0^\circ$ . The usual radiant drift caused by the rotation of the Earth around the Sun is partly compensated by the drift of the orbital elements. This explains the disagreement in radiant drift between different sources as these depend on the activity interval taken into consideration for the radiant drift. The orbital elements show a distinct evolution in time, the longitude of perihelion  $\varPi$ , the inclination  $i$ , and especially the perihelion distance  $q$  increase during the activity period. The eccentricity  $e$  decreases and the semi major axis  $a$  remains constant.

## 1 Introduction

The Andromedids have an impressive record in history books with most impressive meteor storms in the 19<sup>th</sup> century. During the 20<sup>th</sup> century this meteor shower seemed to have vanished and it was assumed that the dust had spread and did no longer cross the Earth orbit.

The parent comet 3D/Biela is a Jupiter-family comet first discovered in 1772 by Montaigne in France and at a later return in 1805 by Pons in France. It was Wilhelm von Biela at a later return in 1826 who obtained enough observations to prove this was a new periodic comet which had been observed before in 1772 and 1805. In 1846 the comet was observed with two separated nuclei. It was a last time seen in 1852 and all later attempts to rediscover it failed (Kronk, 1988).

The earliest known appearance of the Andromedids was witnessed by H.W. Brandes in the evening of 6 December 1798 when he counted about 100 meteors an hour for 4 hours. No information was mentioned about the radiant, but this outburst concerned most likely the Andromedids. Also on 7 December 1830, Abbe Raillard in France mentioned many meteors were seen without giving any further details. More information was obtained by Herrick in 1838 when large and splendid fireballs were seen on both December 6 and 7. Additional observing reports revealed that the radiant position was not far from Cassiopeia or perhaps near the cluster in the sword of Perseus with rates between 125 and 175 per hour. Eduard Heis observed the Andromedids on 6 December 1847 in Germany and obtained a radiant position at R.A.  $21^\circ$  and declination  $+54^\circ$  (Kronk, 1988).

In the 1860s the link was made between comets and meteor showers. Edmond Weiss, Heinrich Louis d'Arrest and Johann Galle found independently that the meteoroids that

caused the activity outbursts in 1798 and 1838 were associated with comet 3D/Biela. Edmond Weiss computed further and noticed the drift of the ascending node of the comet's orbit and predicted that meteor activity caused by debris of this comet might be seen around 28 November 1872 from a radiant at R.A.  $23.4^\circ$  and declination  $+43.0^\circ$  (Kronk, 1988).

The big surprise came in the evening of 27 November 1872 with a most spectacular meteor storm, described as a rain of fire with about 400 meteors every 1.5 minutes. The radiant could be precisely determined at R.A.  $26.6^\circ$  and declination  $+43.8^\circ$ . The time of the maximum was estimated to be at November 27.84 UT when the meteors were too numerous to count. Predicted outbursts for 1878 and 1879 did not take place or went by unnoticed. Another possible outburst was predicted on short notice for 27 November 1885 and did materialize as observers with clear sky noticed immediately an acceptable activity. William Denning had observed meteor activity from the Andromedids with rates of about 100 per hour one night earlier. The evening of 27 November the number of meteors was too high and impossible to count them all with about one meteor every second. At the next expected passage of the parent comet, no such spectacular meteor storm was seen but rates were still several hundreds of meteors per hour on November 24. Andromedids displayed rates of about 100 meteors per hour on 24 November 1899 and about 20 per hour on 21 November 1904. No more activity from this shower was seen until 1940 when R.M. Dole in Maine, USA, reported an outburst with 30 meteors an hour on 15 November and J.P.M. Prentice reported rates of 5 meteors an hour between 27 November and 4 December (Kronk, 1988). No further visual activity from this shower was reported in the 20<sup>th</sup> century and the dust released by comet 3D/Biela was assumed no longer to intersect with the Earth orbit. Past

Andromedid outbursts were modelled and described by Jenniskens and Vaubaillon (2007).

The Andromedids surprised with hourly rates of about 50 during the nights 3–5 December 2011 with a radiant at R.A.  $18^\circ$  and Declination  $+56^\circ$ , the best activity in more than a century and again from the radiant position in Cassiopeia as it was in the beginning of the 19<sup>th</sup> century. The unexpected return was covered by the meteor radar CMOR in Canada (Wiegert et al., 2013) and the CAMS project (Jenniskens et al., 2016). A weak to moderate activity predicted to occur in 2018 did not materialize but the Andromedids surprised unexpectedly in 2021 with significant above normal Andromedid rates observed around 20 November by CAMS networks at the northern hemisphere (Jenniskens, 2022a). This broad activity enhancement was followed by a sharp peak on 28 November at  $\lambda_o = 245.887 \pm 0.007^\circ$  (Jenniskens, 2022b).

The Global Meteor Network (Vida et al., 2021) also recorded the 2021 Andromedid activity, and these results are presented in this analysis.

## 2 GMN 2021 Andromedid results

The Global Meteor Network identified 1034 orbits as Andromedids. This identification has been made based on a list of known meteor showers (Jenniskens et al., 2018) for orbits recorded within  $1^\circ$  in solar longitude of the known activity period, with the radiant within  $3^\circ$  relative to the known radiant position and with a geocentric velocity  $v_g$  within an interval of 10% relative to the reference geocentric velocity (Moorhead et al., 2020).

Using an existing list of meteor showers with earlier determined radiant positions, activity periods and geocentric velocity, is helpful for a preliminary classification of shower meteor meteors, but this approach also creates a bias as the radiant positions, activity period and velocity range obtained will just confirm the reference that has been used for classification.

To consider all the orbits with the same criteria the author applied an iterative procedure starting from some initial reference orbit to identify all orbits that form a concentration of similar orbits which define the meteor shower. This method has been described before (Roggemans et al., 2019).

To identify all possible Andromedid orbits in an independent way all Andromedid orbits according to the GMN identification have been used to obtain a mean orbit according to the method described by Jopek et al. (2006). This mean orbit has then been used to run an iterative procedure to select all similar orbits, recompute the mean orbit and repeat this procedure until the iteration converges at a selection of similar orbits with the most representative mean orbit. To compare orbits on similarity mathematicians established different discrimination criteria, often abbreviated as D-criteria. The D-criteria that we use are these of Southworth and Hawkins (1963), Drummond (1981) and Jopek (1993) combined. The oldest and most

popular D-criterion  $D_{SH}$ , established by Southworth and Hawkins, proves often too tolerant and unsuitable for short period orbits near the ecliptic. It is not unusual that orbits which are very similar according to  $D_{SH}$ , fail for another D-criteria such as that of Drummond or  $D_D$ .

To distinguish dispersed and compact orbits we define five classes with different threshold levels of similarity, groups of orbits with comparable degree of dispersion. These should help to visualize the degree of dispersion and compactness within the meteoroid stream. The different classes of similarity are defined as follows:

- Low:  $D_{SH} < 0.25$  &  $D_D < 0.105$  &  $D_H < 0.25$ ;
- Medium low:  $D_{SH} < 0.2$  &  $D_D < 0.08$  &  $D_H < 0.2$ ;
- Medium high:  $D_{SH} < 0.15$  &  $D_D < 0.06$  &  $D_H < 0.15$ ;
- High:  $D_{SH} < 0.1$  &  $D_D < 0.04$  &  $D_H < 0.1$ ;
- Very high:  $D_{SH} < 0.05$  &  $D_D < 0.02$  &  $D_H < 0.05$ .

The low threshold class with  $D_D < 0.105$  represents the most dispersed particles which may include sporadics with pure chance similarity. The very strong threshold class with  $D_D < 0.02$  represents the core of the dust trail with almost identical orbits. For readability reasons we refer to these classes using only the Drummond  $D_D$  notification.

To limit the dataset in volume all 2021 GMN orbits were chosen between 20 October 2021 and 31 December 2021, in total 76570 orbits. 1954 orbits were identified to fulfill the low threshold criteria, registered between 20 October 2021 ( $\lambda_o = 207.3^\circ$ ) and 29 December 2021 ( $\lambda_o = 278.0^\circ$ ). 195 of these fulfilled the very high threshold criteria, registered between 13 and 26 November 2021

For a better comparison between results based on orbit similarity criteria and the shower identification based on the GMN identification method (radiant position and velocity), the similarity criteria were applied on the dataset with the 1034 preliminary GMN identified Andromedids. The mean orbit of these 1034 Andromedids has been used as reference orbit. Four orbits failed to fulfill even the low threshold criteria, the remaining 1030 GMN Andromedids were classified according to the different similarity classes.

## 3 Activity profile

A simple approach to obtain an activity profile is to count the number of recorded Andromedid orbits per time interval. To eliminate the influence of variable weather circumstances and different camera coverage for different time zones, we use the number of sporadic orbits without shower meteors to calibrate the Andromedid number of orbits for each time interval. This leaves the influence of the zenith distance of the Andromedid radiant as only factor that influences the number of Andromedids per time interval. The zenith distance factor cannot be determined for a mixture of orbits obtained for many different geographic locations mixed in each time interval. Statically we can just assume that the mixture of radiant distances in each interval will tend to average out the influence of the zenith distance.

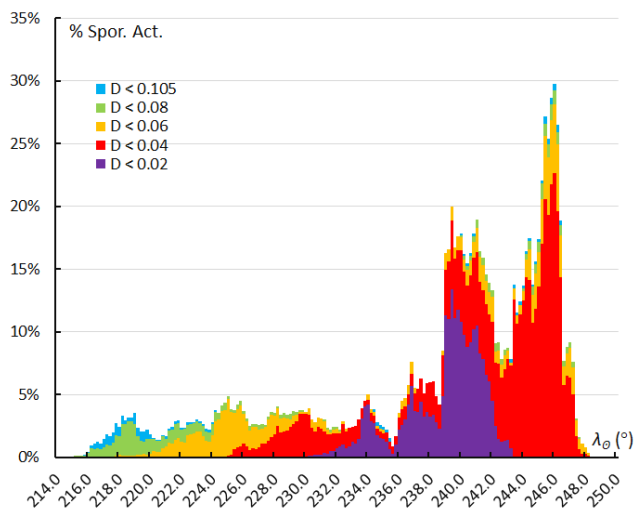


*Figure 1* – Activity profile with the number of Andromedid orbits defined by the GMN shower identification method, expressed as a percentage relative to the number of sporadic orbits recorded during the same interval. The different similarity classes are color coded.

*Figure 1* shows the resulting activity profile using a sampling interval of  $1.1^\circ$  in solar longitude, skipping  $0.2^\circ$  forward in solar longitude for each sampling interval. The width of the sampling interval has been chosen to smooth statistical fluctuations and still to maintain enough detail of the activity variation during the transit of the Earth through the Andromedid dust. The mean orbit used for the similarity criteria was obtained at the median value of the solar longitude of all GMN identified Andromedid orbits ( $\lambda_\odot = 240.6^\circ$ ). It is obvious that this mean reference orbit represents mainly the orbits around  $\lambda_\odot = 240.6^\circ$  with many very high threshold similarities marked in purple in *Figure 1*. The earliest recorded Andromedid orbits have low similarity with this reference orbit and the profile in *Figure 1* ends abruptly at about  $\lambda_\odot = 248^\circ$  before the last peak on 29–30 November was completely ended. It is obvious that the activity period defined in the GMN reference table for shower identification ends too soon.

The abrupt end of the Andromedid activity period in the GMN reference list of meteor showers is to some extent compensated by the recorded December psi Cassiopeiids (DPC#446) which are in fact nothing other than Andromedids which were renamed at the 2011 Andromedid outburst in early December when the radiant was situated in the constellation of Cassiopeia.

Looking at the same activity profile based on the shower identification with orbit similarity criteria (*Figure 2*), the first possible Andromedid orbits were detected ten days earlier than with the GMN shower identification. Possible Andromedid orbits were detected during one month after the last Andromedid orbit identified by GMN. The main shape of the activity profile is visible in the two graphs. A first enhanced Andromedid activity appeared roughly between  $227^\circ < \lambda_\odot < 236^\circ$  with a first modest peak at  $\lambda_\odot = 234^\circ$  (2021, November 16, 11<sup>h</sup> UT). A second component of enhanced activity can be seen in the interval  $236^\circ < \lambda_\odot < 242.6^\circ$  with a peak at  $\lambda_\odot = 239.4^\circ$  (2021,

November 21, 20<sup>h</sup> UT). The sharpest and highest activity occurred in the interval  $243^\circ < \lambda_\odot < 247.2^\circ$  with a sharp peak at  $\lambda_\odot = 246.0^\circ$  (2021, November 28, 08<sup>h</sup> UT). Before and after these three intervals only few and dispersed Andromedid orbits were recorded.

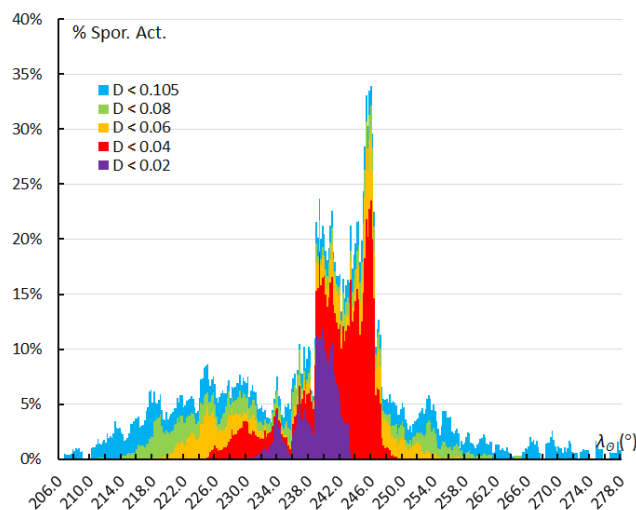


*Figure 2* – Activity profile with the number of Andromedid orbits according to the orbit similarity criteria, expressed as a percentage relative to the number of sporadic orbits recorded during the same interval. The different similarity classes are color coded.

The activity profile based on numbers of orbits provides no precise data on the level of the shower activity in terms of zenithal hourly rates but the shape of the profile provides sufficient evidence for the layered structure of the Andromedid meteoroid stream and the approximate times of the different maxima. It is obvious that the Andromedids are a complex meteoroid stream with multiple superimposed dust trails embedded among widely dispersed particles that encounter the Earth orbit during a period of more than two months.

## 4 Radiant structure

The long duration activity period of the Andromedids suggests a significant radiant drift in geocentric equatorial coordinates. However, the values quoted in literature are not in agreement. Jenniskens (2006) lists  $\Delta\alpha = 0.63^\circ$  and  $\Delta\delta = +0.33^\circ$ , SonotaCo (2009),  $\Delta\alpha = 0.12^\circ$  and  $\Delta\delta = +0.30^\circ$ , Jenniskens et al. (2016)  $\Delta\alpha = 1.00^\circ$  and  $\Delta\delta = +0.37^\circ$  and this study resulted in  $\Delta\alpha = 0.19^\circ$  and  $\Delta\delta = +0.75^\circ$ . Looking at *Figure 3* the radiant drift doesn't show up as expected. The pattern of the radiant drift during the Andromedid activity displays a shape of a crescent. During the first part of the Andromedid activity the radiant drift shows a normal increase in Right Ascension and declination, while the declination continues to increase the Right Ascension remains constant and decreases towards the end of the activity period. The large differences in radiant drift values found in literature can be simply explained as these values depend on the activity interval on which the radiant drift has been obtained. Looking at the 1954 Andromedid orbits identified with the orbit similarity criteria (*Figure 4*) this plot displays the same crescent shape. The December psi Cassiopeiids marked as triangles in *Figure 3* and many of

the sporadic orbits according to the GMN shower identification were identified as Andromedids by the orbit similarity method.

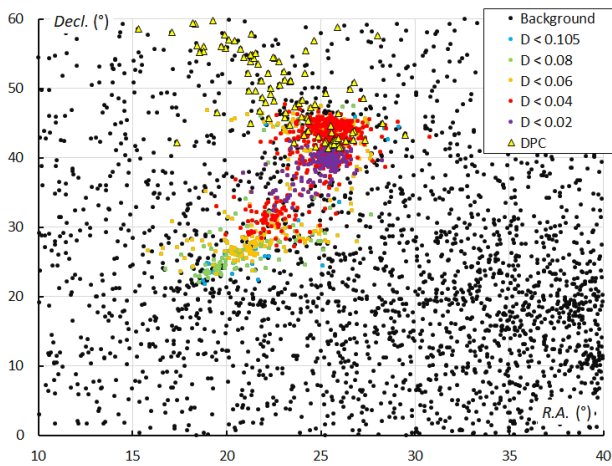


Figure 3 – The Andromedid radiants in equatorial geocentric coordinates based on the GMN shower identification, color coded according to the orbit similarity criteria. The triangles indicate the Andromedids which were identified as December psi Cassiopeids (DPC#446).

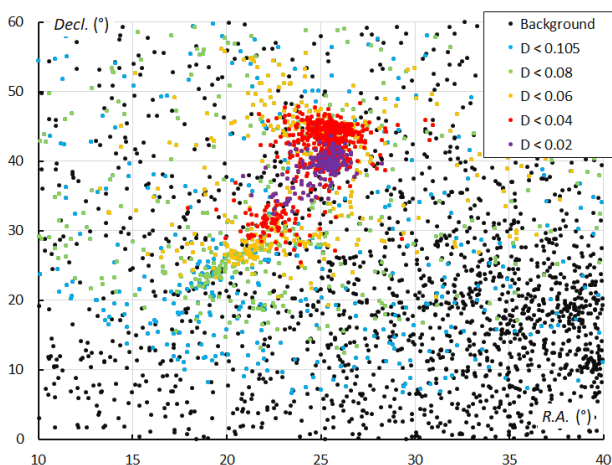


Figure 4 – The Andromedid radiants in equatorial geocentric coordinates based on the orbit similarity shower identification, color coded according to the orbit similarity criteria. The December psi Cassiopeids (DPC#446) orbits from Figure 3 are detected as Andromedids.

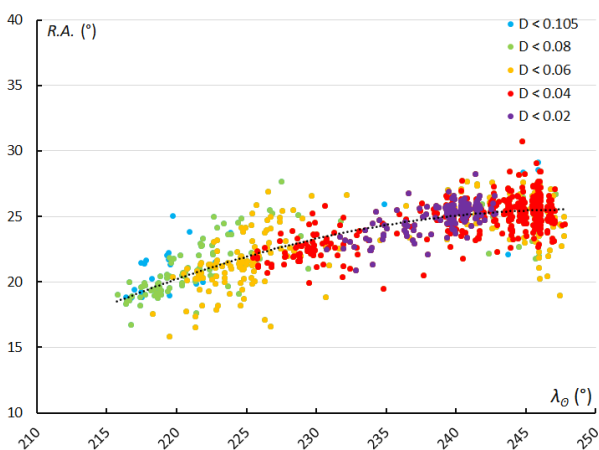


Figure 5 – The radiant drift in Right Ascension, based on the GMN shower identification.

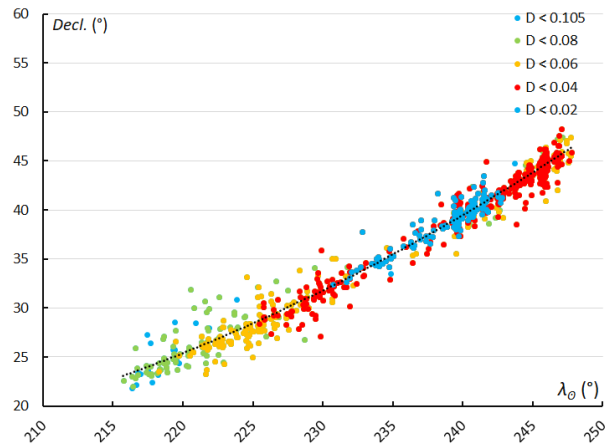


Figure 6 – The radiant drift in declination, based on the GMN shower identification.

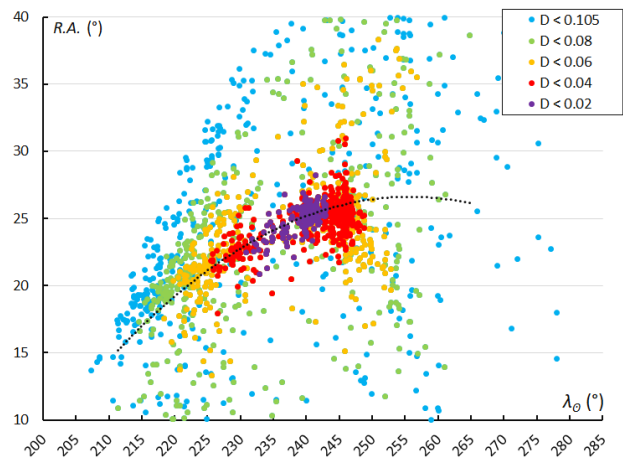


Figure 7 – The radiant drift in Right Ascension, based on the orbit similarity shower identification.

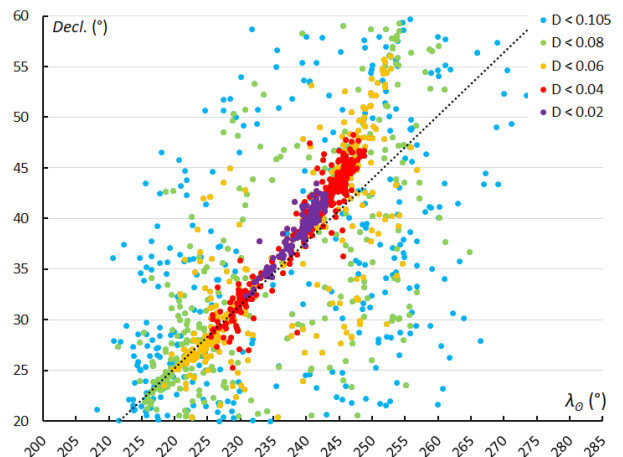


Figure 8 – The radiant drift in declination, based on the orbit similarity shower identification.

The radiant drift in Right Ascension in this case should not be described with an ordinary linear regression, but rather with a second order polynomial to fit the decreasing drift in function of the solar longitude (Figure 5). The radiant drift in declination shows an almost linear increase during the activity period (Figure 6). The unusual radiant drift behavior is even better visible in the plot with the orbit similarity shower identification with a longer activity period but ignoring the low similarity cases (Figure 7).

With the much longer activity period detected with the orbit similarity shower identification, the radiant drift in declination increases significantly in the second half of the activity period after a rather constant drift in declination during the first half (Figure 8). The third and last part of the activity period determined by orbit similarity identification, includes the orbits that were identified by GMN as December psi Cassiopeids (DPC#446).

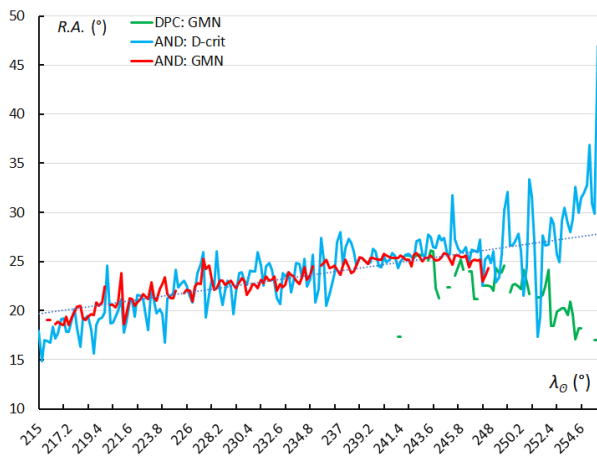


Figure 9 – The radiant drift in Right Ascension, using the sliding mean of the Right Ascension computed for a time interval of  $0.4^\circ$  in solar longitude in steps of  $0.2^\circ$ . The GMN shower identification is marked in red for the Andromedids and in green for the December psi Cassiopeids, the Andromedids according to the orbit similarity identification are marked in blue.

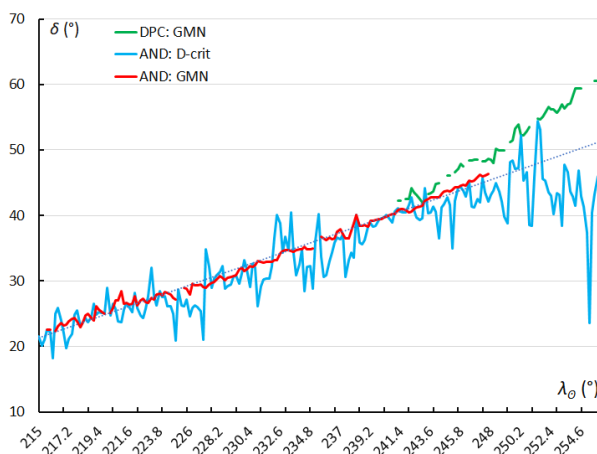


Figure 10 – The radiant drift in declination, using the sliding mean of the declination computed for a time interval of  $0.4^\circ$  in solar longitude in steps of  $0.2^\circ$ . The GMN shower identification is marked in red for the Andromedids and in green for the December psi Cassiopeids, the Andromedids according to the orbit similarity identification are marked in blue.

To reduce the scatter on the Right Ascension and declination for each interval in solar longitude, the average value has been calculated for intervals of  $0.4^\circ$  in solar longitude, using steps of  $0.2^\circ$ . The values for the radiant positions of Andromedids according to the GMN shower identification (red) display very little scatter compared to the values according to the orbit similarity identification (blue) (Figures 9 and 10).

The December psi Cassiopeids (DPC) identified by the GMN method display a deviant behavior as the radiant regresses in Right Ascension (Figure 9) and increases more in declination (Figure 10). These radiants were detected by the orbit similarity method as ordinary Andromedids among plenty of other Andromedids identified after the assumed activity period in the reference list used for the GMN identification. DPC orbits display a slightly different radiant drift compared to the ordinary Andromedids which appear with a very large scatter on the radiant positions.

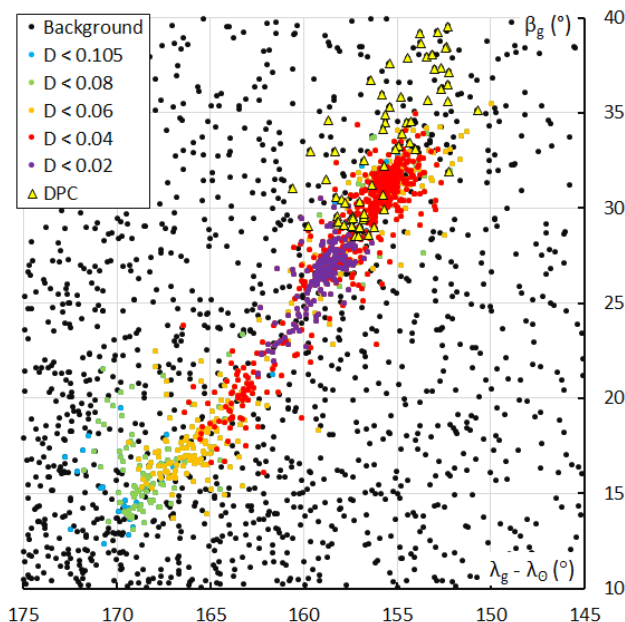


Figure 11 – The Andromedid radiants in Sun-centered geocentric ecliptic coordinates based on the GMN shower identification, color coded according to the orbit similarity criteria. The triangles indicate the Andromedids which were identified as December psi Cassiopeids.

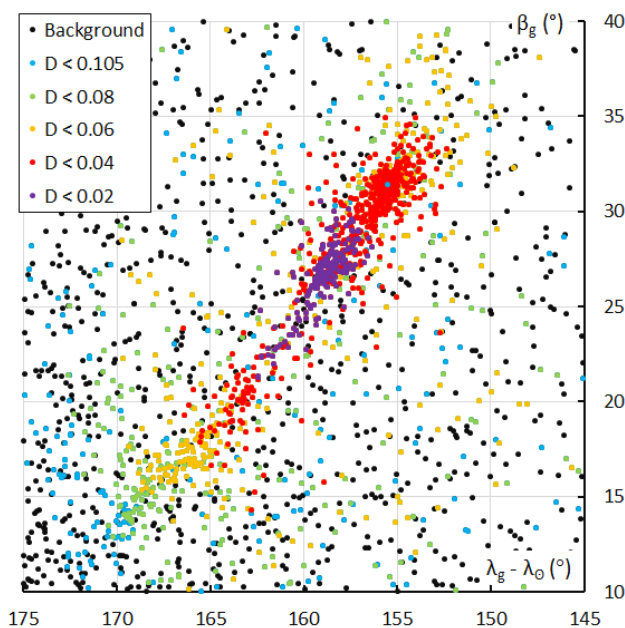
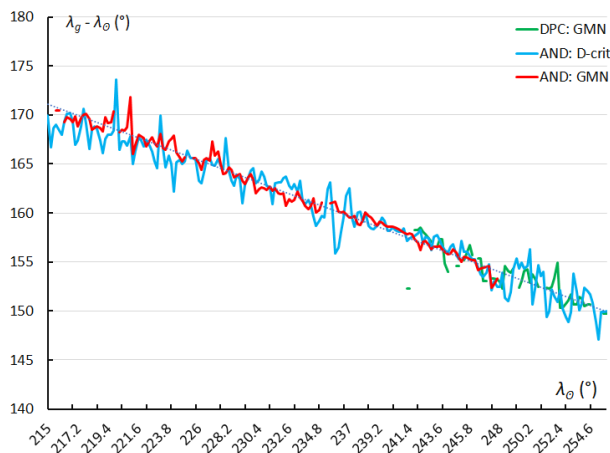
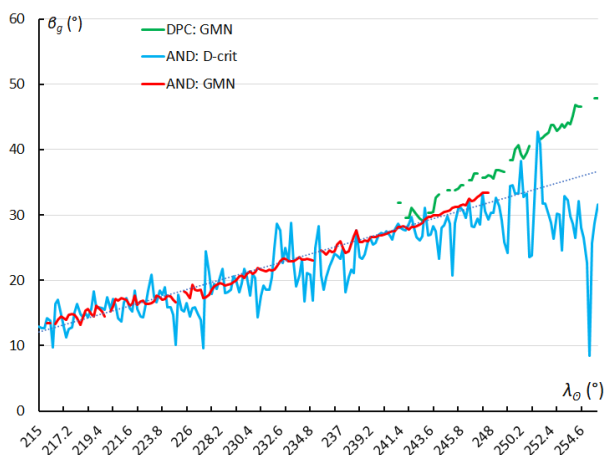


Figure 12 – The Andromedid radiants in Sun-centered geocentric ecliptic coordinates based on the orbit similarity shower identification, color coded according to the orbit similarity criteria. The December psi Cassiopeids (DPC#446) orbits from Figure 11 are detected as Andromedids.

The usual way to look at a radiant without the radiant drift caused by the rotation of the Earth around the Sun is to plot the Sun-centered geocentric ecliptic coordinates. For most showers this results in a compact concentration of radiant points. For the Andromedids this results in a completely different picture with a long stretched radiant area. This means that the particles don't move on parallel orbits but encounter the Earth at different angles to an extent that the usual radiant drift is compensated. The plots obtained with the GMN identification, and the orbit similarity identification can be compared in *Figures 11 and 12*.



*Figure 13* – The radiant drift in Sun-centered geocentric ecliptic longitude, using the sliding mean of the Sun-centered geocentric ecliptic longitude computed for a time interval of 0.4° in solar longitude in steps of 0.2°. The GMN shower identification is marked in red for the Andromedids and in green for the December psi Cassiopeiids, the Andromedids according to the orbit similarity identification are marked in blue.



*Figure 14* – The radiant drift in geocentric ecliptic latitude, using the sliding mean of the geocentric ecliptic latitude computed for a time interval of 0.4° in solar longitude in steps of 0.2°. The GMN shower identification is marked in red for the Andromedids and in green for the December psi Cassiopeiids, the Andromedids according to the orbit similarity identification are marked in blue.

The Andromedids are a very particular meteoroid stream with perturbed orbits in a way that it results in a mechanism compensating the usual radiant drift caused by the Earth's movement around the Sun. The degree that these orbits have been smeared out during the transit of the Earth is very well reflected in a drift of the Sun-centered geocentric ecliptic

coordinates. Most meteor showers do not display anything like this. *Figures 13 and 14* show this effect. The radiant drift due to the perturbed smeared out orbits in Sun-centered geocentric ecliptic coordinates equals  $\Delta(\lambda - \lambda_o) = -0.1^\circ$  and  $\Delta\beta = +0.12^\circ$ . The drift in geocentric ecliptic latitude for the December psi Cassiopeiids deviates slightly in ecliptic latitude as can be seen in *Figure 14*. The authors have no explanation for this remarkable anomaly.

Apart of the radiant position which indicates the direction from where the particles hit the planet, the velocity relative to the Earth is another very important property of a meteor shower. Measuring the velocity of a fast-moving object on a short trail at the sky introduces instrumental measurement errors. If all shower meteors would have the same velocity, we should see a nice symmetric Gaussian distribution representing the spread caused by measurement errors. This is not the case whether we look at the Andromedids identified by GMN (*Figure 15*) or identified by the orbit similarity method (*Figure 16*). The GMN identification has very little dispersed orbits, while the orbit similarity method picks up more dispersed particles.

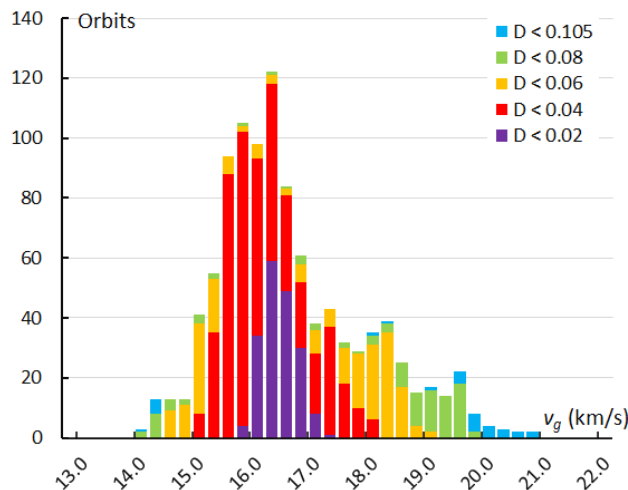


*Figure 15* – The histogram with the distribution of the geocentric velocity obtained for Andromedids identified by the GMN shower identification method.

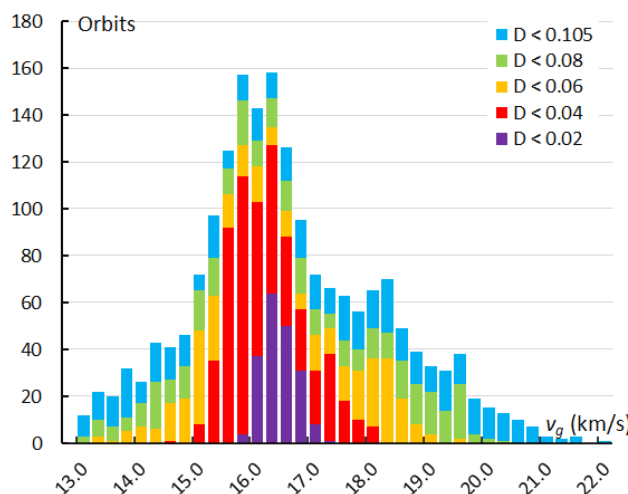


*Figure 16* – The histogram with the distribution of the geocentric velocity obtained for Andromedids identified by the orbit similarity shower identification method.

The profiles appear skew and show different peaks, suggesting that some components with slightly different geocentric velocity contributed to the 2021 Andromedid activity. The different classes of similarity show a concentration of almost identical orbits ( $D_D < 0.02$ ) at  $v_g = 16.3$  km/s which is the geocentric velocity of the reference orbit obtained as mean orbit for all GMN identified Andromedids. The orbits with  $D_D < 0.04$  which correspond mainly with the orbits of the second and the last peak, had a slightly lower velocity. Several lower similarity orbits had a significant faster velocity compared to the main bulk of Andromedids. This requires a look at the variation in velocity in function of time, in our case we use the solar longitude  $\lambda_\odot$ .

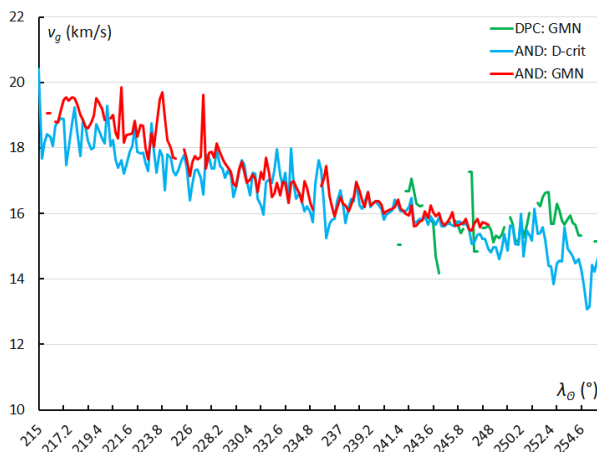


Figure 17 – The variation in geocentric velocity  $v_g$ , using the sliding mean of the geocentric velocity computed for a time interval of  $0.4^\circ$  in solar longitude in steps of  $0.2^\circ$ . The GMN shower identification is marked in red for the Andromedids and in green for the December psi Cassiopeiids, the Andromedids according to the orbit similarity identification are marked in blue.

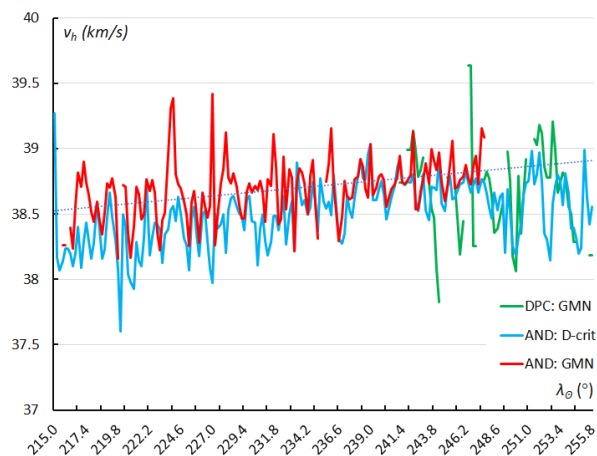


Figure 18 – The variation in heliocentric velocity  $v_h$ , using the sliding mean of the heliocentric velocity computed for a time interval of  $0.4^\circ$  in solar longitude in steps of  $0.2^\circ$ . The GMN shower identification is marked in red for the Andromedids and in green for the December psi Cassiopeiids, the Andromedids according to the orbit similarity identification are marked in blue.

The change in geocentric velocity  $v_g$  in function of the solar longitude is shown in Figure 17. The geocentric velocity is the result of the sum of the velocity vector of the Earth’s own movement around the Sun, about 29.8 km/s, and the

velocity vector of the particle in its orbit around the Sun. The heliocentric velocity  $v_h$  of the Andromedids appears to be constant, apart from a slight increase of 0.4 km/s between the start and then end of the activity period. The decrease in geocentric velocity is caused by the change in angle of entry of the Andromedids during the shower activity as the radiant moves towards the antapex. The different peaks in Figures 15 and 16 may be caused by the large input during the different peaks in the activity profile which appeared at different times with slightly different velocities.

Another interesting plot is the radiant distribution in Sun-centered geocentric ecliptic coordinates, color coded for the geocentric velocity (Figures 19 and 20). The Earth first encounters the fastest Andromedid particles and gradually intercepts Andromedid particles at lower geocentric velocity from more northern ecliptic latitudes and lower Sun-centered ecliptic longitude. Both shower identification methods show the same effect. The more scattered orbits defined by the orbit similarity method show the fastest Andromedids at higher Sun-centered ecliptic longitude at the beginning of the shower activity, the slowest particles appear towards the end of the activity.

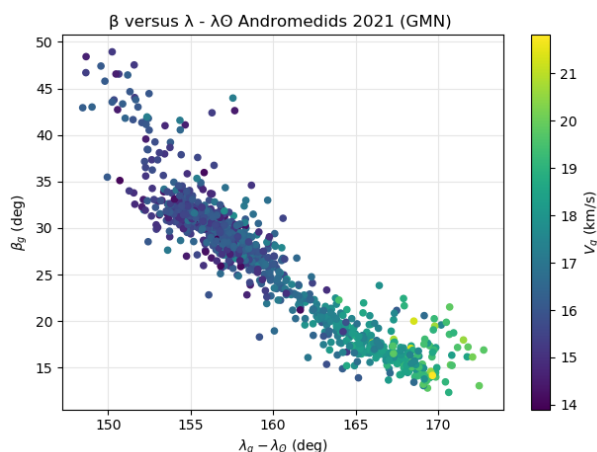


Figure 19 – The Andromedid radiants in Sun-centered geocentric ecliptic coordinates based on the GMN shower identification, color coded according to the geocentric velocity.

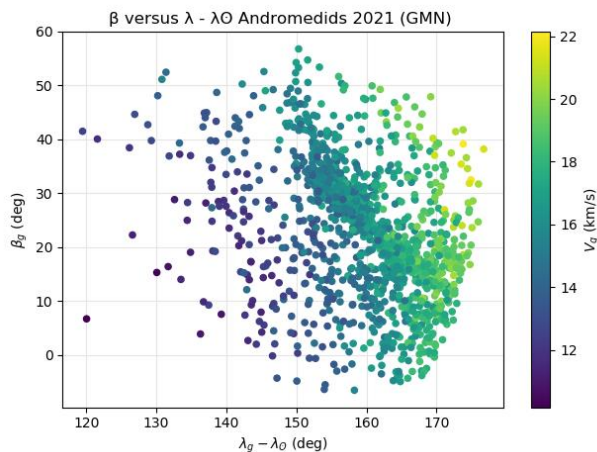


Figure 20 – The Andromedid radiants in Sun-centered geocentric ecliptic coordinates based on the orbit similarity shower identification, color coded according to the geocentric velocity.

## 5 The drifting in orbital elements

### Longitude of perihelion $\Pi$

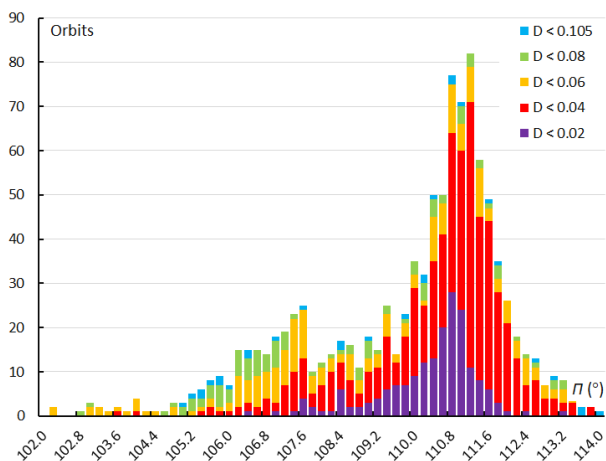


Figure 21 – The histogram with the distribution of the longitude of perihelion  $\Pi$  obtained for Andromedids identified by the GMN shower identification method.

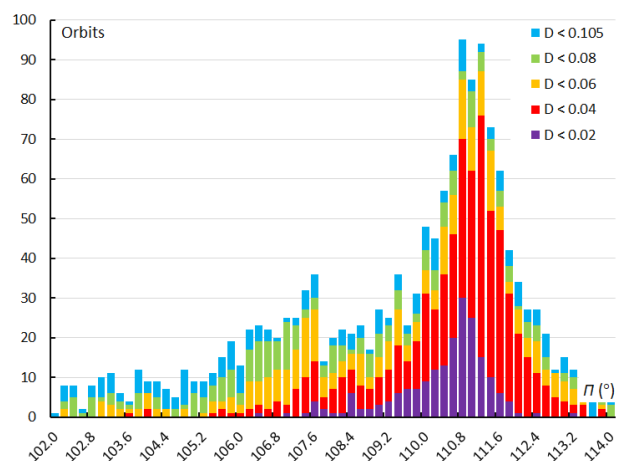


Figure 22 – The histogram with the distribution of the longitude of perihelion  $\Pi$  obtained for Andromedids identified by the orbit similarity shower identification method.

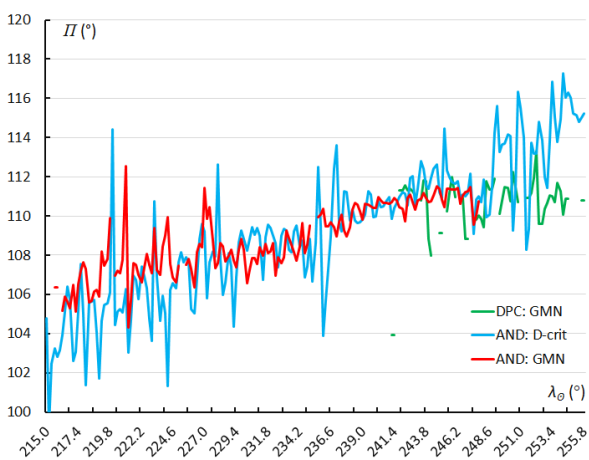


Figure 23 – The variation in longitude of perihelion  $\Pi$ , using the sliding mean of  $\Pi$  computed for a time interval of  $0.4^\circ$  in solar longitude in steps of  $0.2^\circ$ . The GMN shower identification is marked in red for the Andromedids and in green for the December psi Cassiopeiids, the Andromedids according to the orbit similarity identification are marked in blue.

The distribution of the longitude of perihelion  $\Pi$ , provides insight in the dispersion of the meteoroid stream at its perihelion which corresponds to its closest position to the Sun. The longitude of perihelion is composed by the time dependent longitude of the ascending node  $\Omega$  and the argument of perihelion  $\omega$ .

Both the GMN (Figure 21) and the orbit similarity shower identification (Figure 22) result in a similar asymmetric distribution with some peaks. The variation of the longitude of perihelion in function of the solar longitude  $\lambda_\odot$  indicates a slight increase for the Andromedids but remains rather constant for the December psi Cassiopeiids (Figure 23). The large scatter indicates that the positions of the perihelia of the Andromedids got very dispersed.

### The inclination $i$

The inclination  $i$  provides insight in the orientation of the meteor orbits relative to the ecliptic. Both the GMN (Figure 24) and the orbit similarity shower identification (Figure 25) result in a similar asymmetric distribution with at least two distinct peaks.

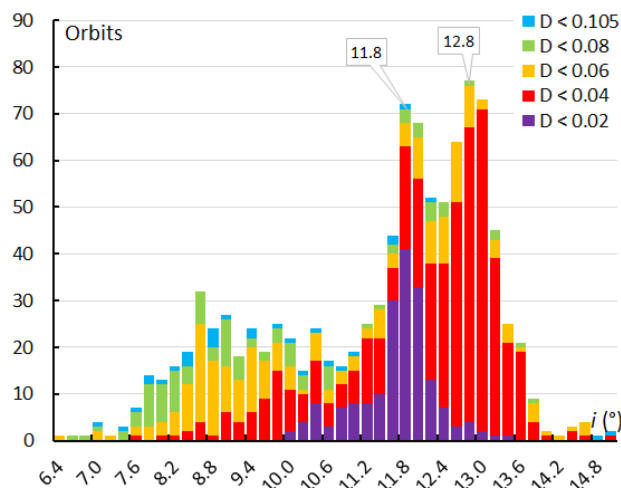


Figure 24 – The histogram with the distribution of the inclination  $i$  obtained for Andromedids identified by the GMN shower identification method.

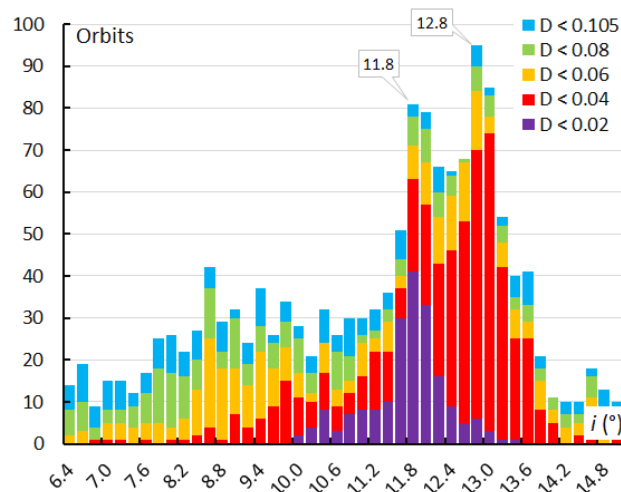


Figure 25 – The histogram with the distribution of the inclination  $i$  obtained for Andromedids identified by the orbit similarity shower identification method.

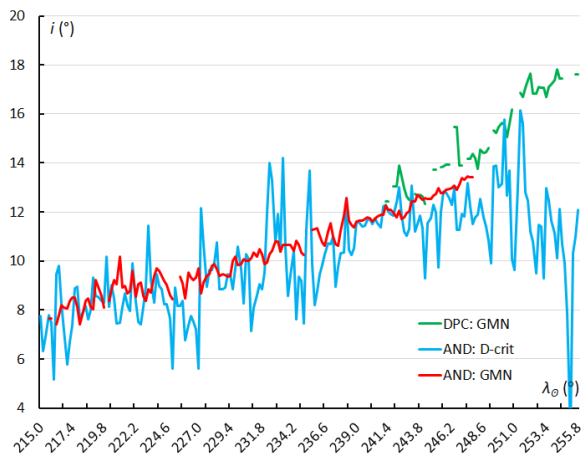


Figure 26 – The variation in inclination  $i$ , using the sliding mean of the inclination computed for a time interval of  $0.4^\circ$  in solar longitude in steps of  $0.2^\circ$ . The GMN shower identification is marked in red for the Andromedids and in green for the December psi Cassiopeids, the Andromedids according to the orbit similarity identification are marked in blue.

Figure 26 shows that the wide range in inclination shown in Figures 24 and 25, changes in time. The first Andromedids encountered by Earth have a lower inclination than during the activity maxima. The peaks in the histogram correspond to the maxima in the activity profile. The gradual increase in inclination during the activity is obvious for the Andromedids and the December psi Cassiopeids identified by GMN. The scatter at the end of the activity period for the orbit similarity identification is due to some outliers among fewer datapoints.

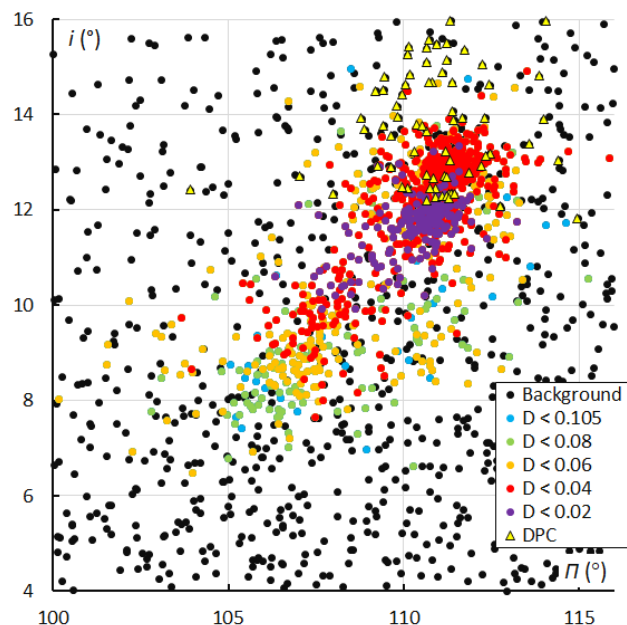


Figure 27 – The Andromedid orbits plotted as inclination  $i$  against the longitude of perihelion  $\Pi$  based on the GMN shower identification, color coded according to the orbit similarity criteria. The triangles indicate the Andromedids which were identified as December psi Cassiopeids.

The inclination  $i$  can be plotted against the longitude of perihelion  $\Pi$  to check for concentrations within the meteoroid stream. The graph with the inclination  $i$  plotted

against the longitude of perihelion  $\Pi$  shows two concentrations with the first modest peak at  $\lambda_\theta = 234^\circ$  containing lower inclination orbits around  $\Pi = 107.6^\circ$  with  $i = 10.6^\circ$ . The two other peaks at  $\lambda_\theta = 239.4^\circ$  and  $\lambda_\theta = 246.0^\circ$  include higher inclination orbits at  $\Pi = 110.8^\circ$  with  $i = 11.8^\circ$  and at  $\Pi = 111.2^\circ$  with  $i = 12.8^\circ$ . The December psi Cassiopeids at the end of the Andromedid activity appear with higher inclination and more dispersed in length of perihelion. The same picture appears in the plot with the GMN shower identification (Figure 27) as well as in the orbit similarity shower identification (Figure 28).

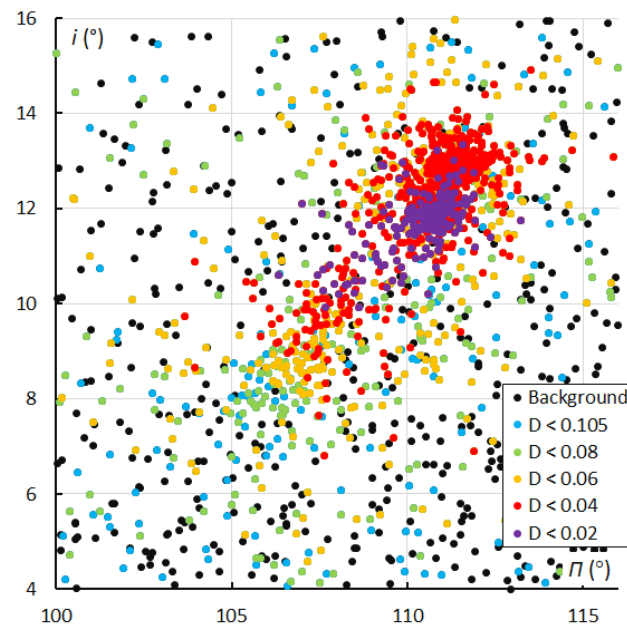


Figure 28 – The Andromedid orbits plotted as inclination  $i$  against the longitude of perihelion  $\Pi$  based on the orbit similarity shower identification, color coded according to the orbit similarity criteria. The December psi Cassiopeids (DPC#446) orbits from Figure 27 are detected as Andromedids.

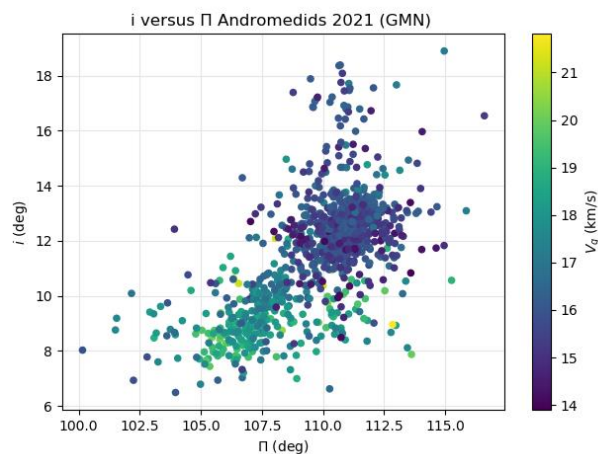
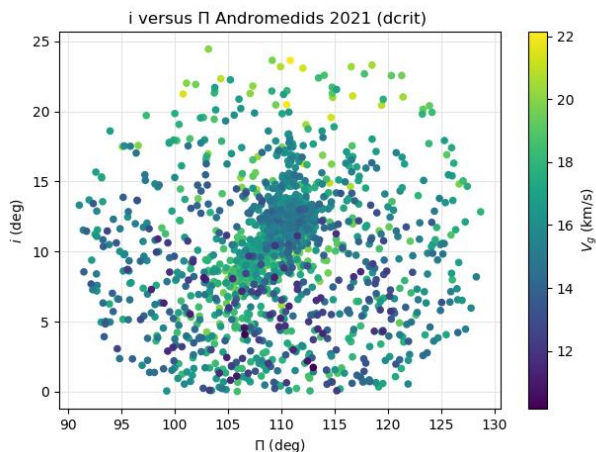


Figure 29 – The Andromedid orbits plotted as inclination  $i$  against the longitude of perihelion  $\Pi$  based on the GMN shower identification, color coded according to the geocentric velocity.

Looking at the distribution of the inclination against the longitude of perihelion color coded for the geocentric velocity, we see a concentration with at  $\Pi = 107.6^\circ$  at about  $9^\circ$  inclination with mainly fast Andromedids. Another concentration appears at  $\Pi = 111^\circ$  with an inclination of about  $13^\circ$  with significant slower Andromedids. The more

scattered dots at higher inclinations were all identified as December psi Cassiopeids (see *Figure 27*).



*Figure 30* – The Andromedid orbits plotted as inclination  $i$  against the longitude of perihelion  $\Pi$  based on the orbit similarity shower identification, color coded according to the geocentric velocity.

The same plot for the orbit similarity shower identification shows a much larger scatter in inclination and longitude of perihelion (*Figure 30*). The two concentrations seen in *Figure 29* are still visible but less distinct.

**The perihelion distance  $q$**

The perihelion distance gives insight in the dispersion in the closest approach to the Sun of meteoroid orbits. The closer the particles of a meteoroid stream get to the Sun, the more intense their exposure to the destructive forces of the Sun. For the fragile cometary dust of comet 3D/Biela these particles will suffer a significant stress at each perihelion passage. If the distance to the Sun differs a lot for different components of the shower, this effect will have a different result for these components.

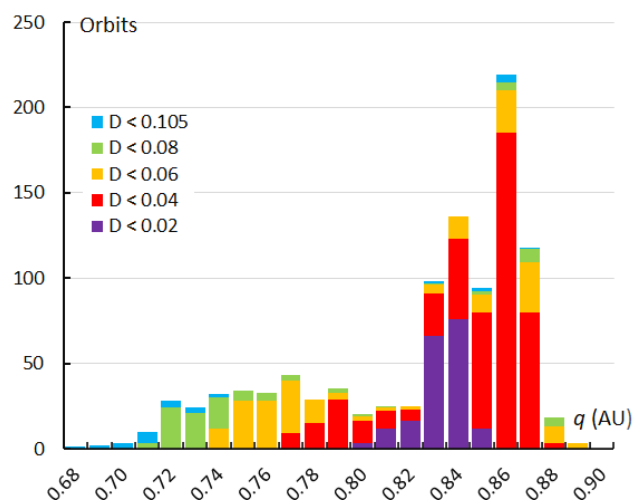


*Figure 31* – The histogram with the distribution of the perihelion distance  $q$  obtained for Andromedids identified by the GMN shower identification method.

Looking at the histogram with the perihelion distance distribution we see a very asymmetric distribution covering a wide range of perihelion distances  $q$  with at least two distinct peaks at  $q = 0.84$  A.U. and  $q = 0.86$  A.U. Within a

wide range from about 0.68 to almost 1.00 A.U. the registered Andromedid orbits undergo a significant different thermal stress at their perihelion passage. Both shower identification methods result in a similar histogram (*Figures 31 and 32*), with the orbit similarity method having more Andromedids at the beginning and the end of the activity period.

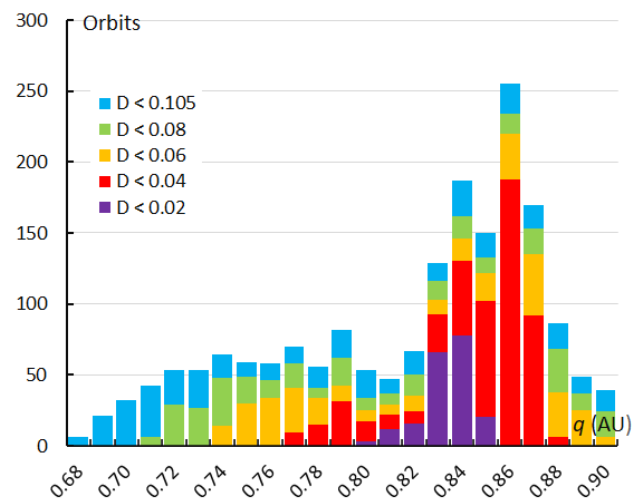


*Figure 32* – The histogram with the distribution of the perihelion distance  $q$  obtained for Andromedids identified by the orbit similarity shower identification method.

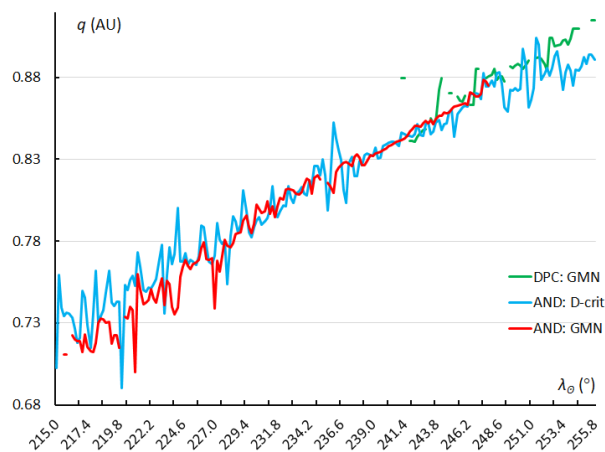


*Figure 33* – The variation in perihelion distance  $q$ , using the sliding mean of the perihelion distance computed for a time interval of  $0.4^\circ$  in solar longitude in steps of  $0.2^\circ$ . The GMN shower identification is marked in red for the Andromedids and in green for the December psi Cassiopeids, the Andromedids according to the orbit similarity identification are marked in blue.

Looking at the perihelion distance  $q$  in function of the solar longitude  $\lambda_\theta$ , a very distinct trend can be seen (*Figure 33*). The Andromedid activity starts with orbits with a perihelion distance closer to the Sun, gradually increasing the perihelion distance towards the Earth’s orbit during the Andromedid activity period. The December psi Cassiopeids are perfectly in line with this trend. The peaks in *Figures 31 and 32* correspond to the different maxima in the activity profile (*Figures 1 and 2*). The drift in perihelion distance during the transit of Earth through the stream is remarkable. The distribution of the perihelion distance in

function of the longitude of perihelion and inclination provides some more insight in the structure of the stream.

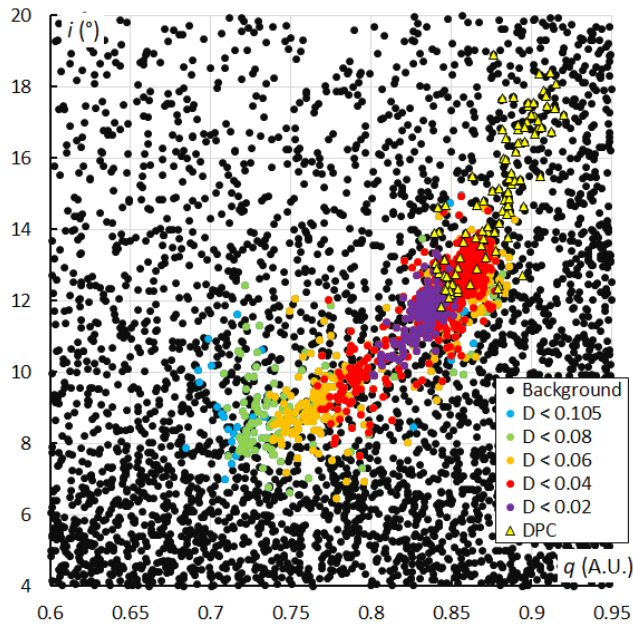


Figure 34 – The Andromedid orbits plotted as inclination  $i$  against the perihelion distance  $q$  based on the GMN shower identification, color coded according to the orbit similarity criteria. The triangles indicate the Andromedids which were identified as December psi Cassiopeids.

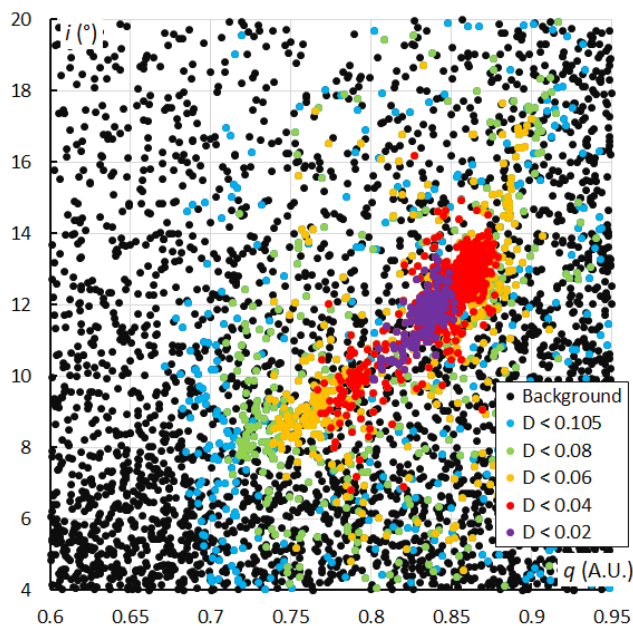


Figure 35 – The Andromedid orbits plotted as inclination  $i$  against the perihelion distance  $q$  based on the orbit similarity shower identification, color coded according to the orbit similarity criteria.

How does the inclination  $i$ , or the orientation of the Andromedid orbits relative to the ecliptic change with the perihelion distance  $q$ ? Figure 34 shows a clear trend with an increasing perihelion distance and increasing inclination. Figures 26 and 33 show how the inclination and perihelion distance increase in function of the solar longitude. The plot based on the orbit similarity shower identification (Figure 35) displays more scatter but confirms the pattern of Figure 34.

Taking the geocentric velocity  $v_g$  into account the fastest Andromedids appear at the lowest perihelion distances and lower inclination at the beginning of the activity period (Figure 36). The plot for the orbit similarity shower identification confirms this trend but appears more diffuse covering a wider range in inclination with mainly dispersed particles (Figure 37).

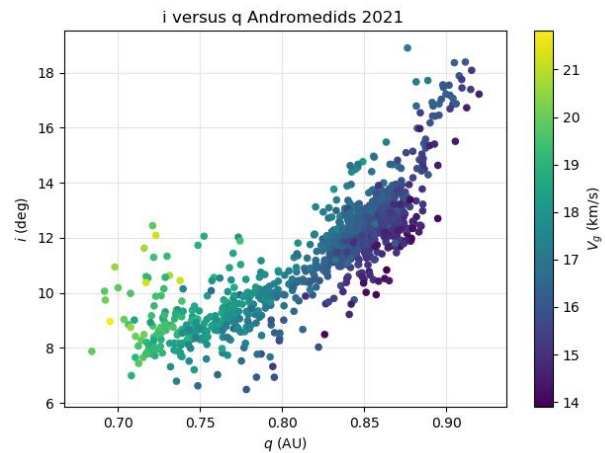


Figure 36 – The Andromedid orbits plotted as inclination  $i$  against the perihelion distance  $q$  based on the GMN shower identification, color coded according to the geocentric velocity.

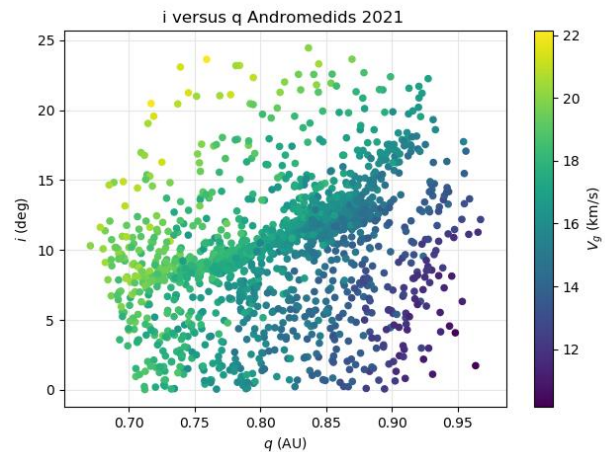
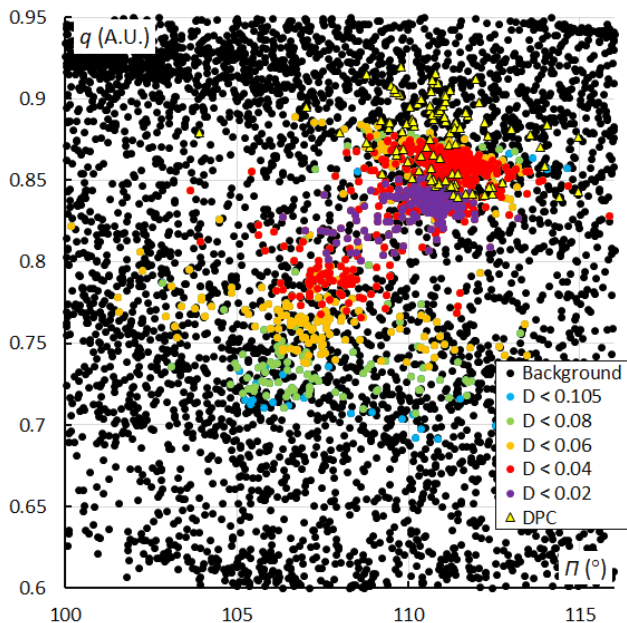


Figure 37 – The Andromedid orbits plotted as inclination  $i$  against the perihelion distance  $q$  based on the orbit similarity shower identification, color coded according to the geocentric velocity.

Looking at the distribution of the perihelion distance against the longitude of perihelion, we get a very good picture of the dispersion of the Andromedids at their perihelion in both longitude and distance to the Sun. Figure 38 shows this distribution where the first part of the activity period with the first moderate maximum appears separated from the dense concentration caused by the second and the third peak. The December psi Cassiopeids partly overlap with the last concentration. The plot for the orbit similarity shower identification (Figure 39) confirms this picture, although with a larger spread in longitude of perihelion.

Taking the geocentric velocity  $v_g$  into account, there is a clear trend with faster Andromedids at lower perihelion distances and slower meteors at higher perihelion distance (Figure 40). The orbit similarity shower identification

results in the same picture but with larger scatter in longitude or perihelion (*Figure 41*).



*Figure 38* – The Andromedid orbits plotted as perihelion distance  $q$  against longitude of perihelion  $\Pi$  based on the GMN shower identification, color coded according to the orbit similarity criteria. The triangles indicate the Andromedids which were identified as December psi Cassiopeids.

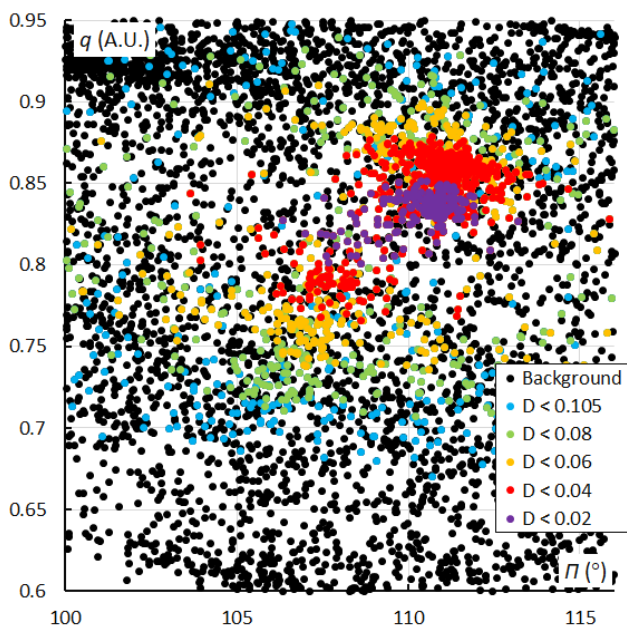


*Figure 39* – The Andromedid orbits plotted as perihelion distance  $q$  against longitude of perihelion  $\Pi$  based on the orbit similarity shower identification, color coded according to the orbit similarity criteria.

**The eccentricity  $e$**

The eccentricity describes the shape of the orbit, with  $e = 0$  for a perfect circle,  $e = 1$  for a parabolic orbit and  $e > 1$  for a hyperbolic orbit. The histogram for the eccentricities recorded for the Andromedids shows a slightly skew profile (*Figures 42 and 43*) for both shower identification methods.

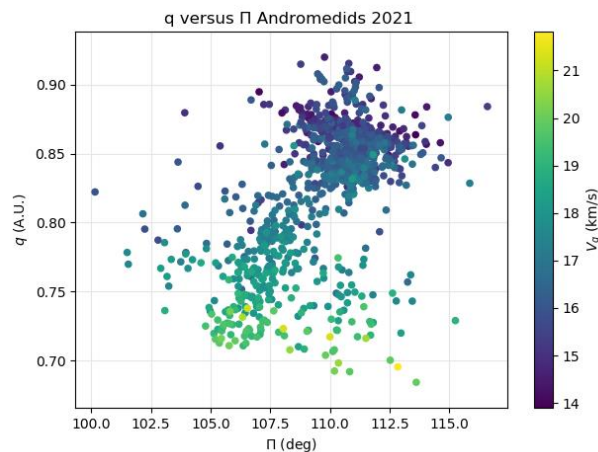


*Figure 40* – The Andromedid orbits plotted as perihelion distance  $q$  against the longitude of perihelion  $\Pi$  based on the GMN shower identification, color coded according to the geocentric velocity.

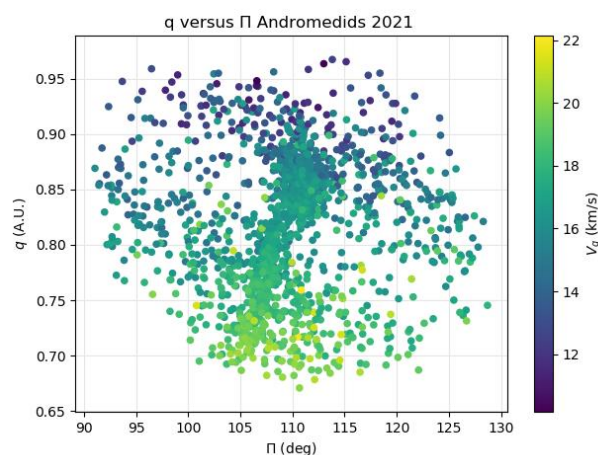


*Figure 41* – The Andromedid orbits plotted as perihelion distance  $q$  against the longitude of perihelion  $\Pi$  based on the orbit similarity shower identification, color coded according to the geocentric velocity.

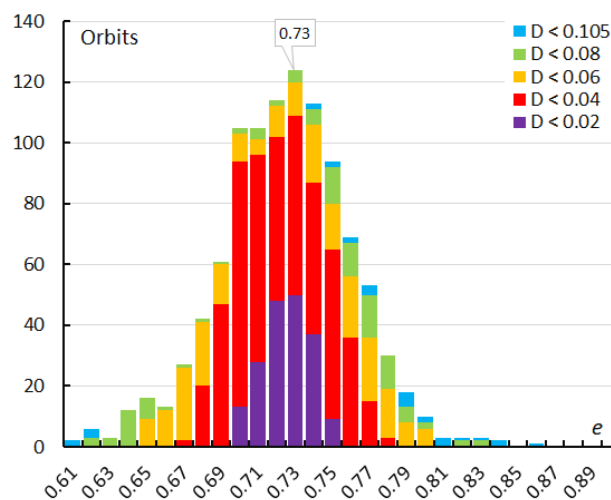


*Figure 42* – The histogram with the distribution of the eccentricity  $e$  obtained for Andromedids identified by the GMN shower identification method.

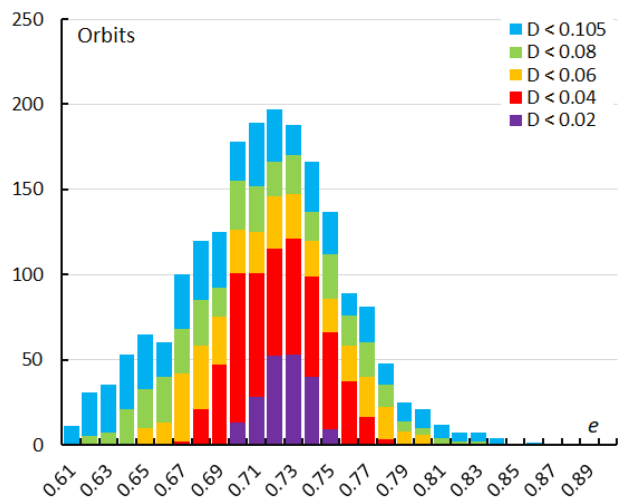


Figure 43 – The histogram with the distribution of the eccentricity  $e$  obtained for Andromedids identified by the orbit similarity shower identification method.

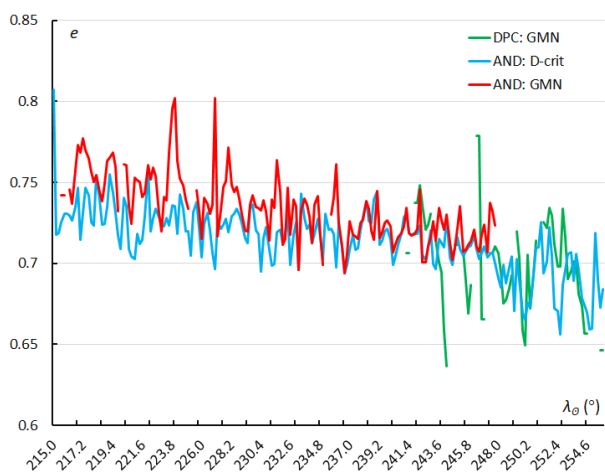


Figure 44 – The variation in eccentricity  $e$ , using the sliding mean of the eccentricity computed for a time interval of  $0.4^\circ$  in solar longitude in steps of  $0.2^\circ$ . The GMN shower identification is marked in red for the Andromedids and in green for the December psi Cassiopeids, the Andromedids according to the orbit similarity identification are marked in blue.

Figure 44 presents the evolution of the eccentricity with time (solar longitude) and shows a slight decrease within a significant scatter during the activity period. The December psi Cassiopeids fit in very well at the end of the activity period of the Andromedids.

The plot of the eccentricity against the longitude of perihelion (Figures 45 and 46) reveals a distinct concentration with the early orbits at higher eccentricity values and lower longitude of perihelion values. The second and third peak appear at slightly lower eccentricity and higher longitude of perihelion.

A clearer picture emerges when we look at the same plot with eccentricity against longitude of perihelion with the velocity color coded. In Figure 47 shows two concentrations, one formed at the first peak with higher eccentricity and lower longitude of perihelion. The second

and the third peak form another concentration with slightly lower eccentricity, higher longitude of perihelion and significant lower velocities. The same trend can be seen in Figure 48 although more diffuse due to the much more dispersed orbits. At the top of Figure 47 we see that 4 data points with high eccentricity are missing in Figure 48. This is because the orbit similarity shower identification rejects these 4 orbits which were identified as Andromedids by the GMN shower identification.

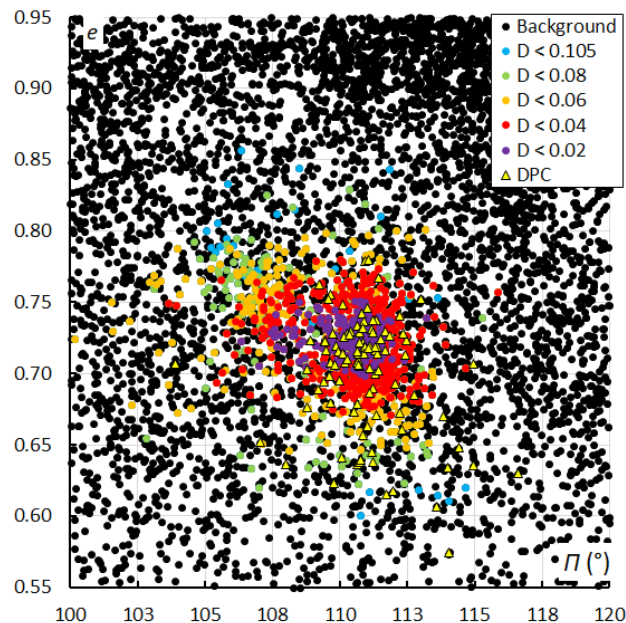


Figure 45 – The Andromedid orbits plotted as eccentricity  $e$  against longitude of perihelion  $\Pi$  based on the GMN shower identification, color coded according to the orbit similarity criteria. The triangles indicate the Andromedids which were identified as December psi Cassiopeids.

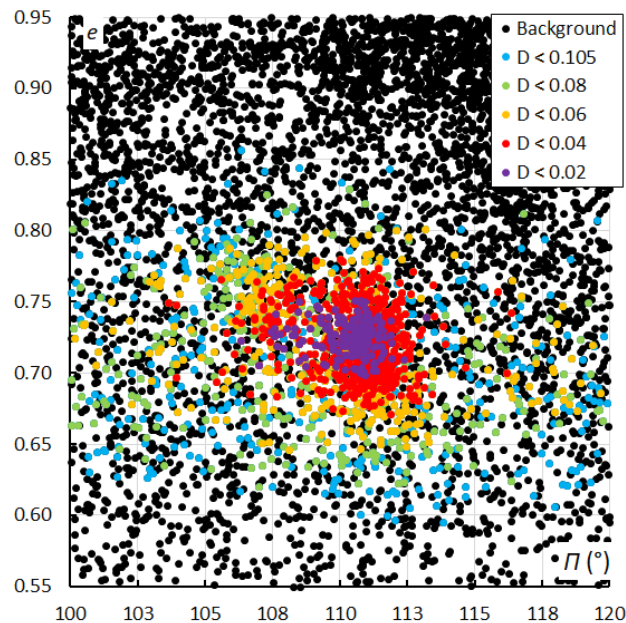


Figure 46 – The Andromedid orbits plotted as eccentricity  $e$  against longitude of perihelion  $\Pi$  based on the orbit similarity shower identification, color coded according to the orbit similarity criteria.

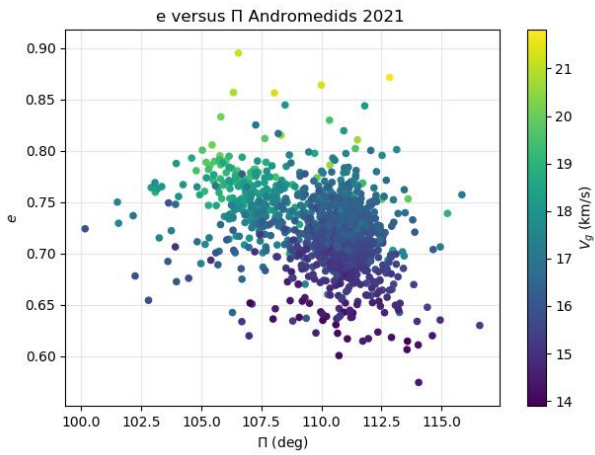


Figure 47 – The Andromedid orbits plotted as eccentricity  $e$  against the longitude of perihelion  $\Pi$  based on the GMN shower identification, color coded according to the geocentric velocity.

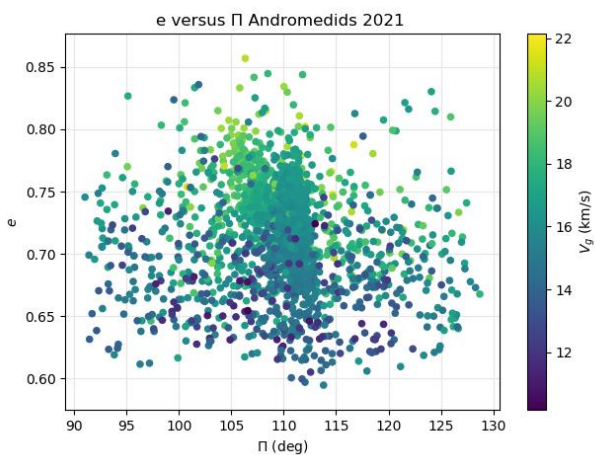


Figure 48 – The Andromedid orbits plotted as eccentricity  $e$  against the longitude of perihelion  $\Pi$  based on the orbit similarity shower identification, color coded according to geocentric velocity.

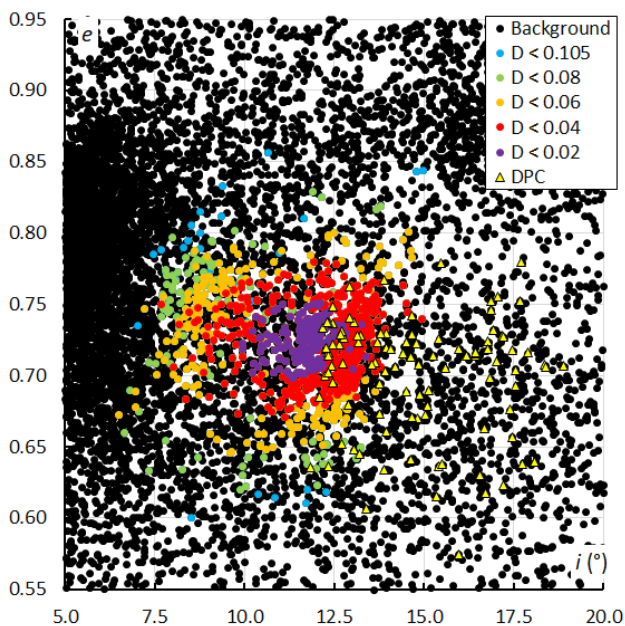


Figure 49 – The Andromedid orbits plotted as eccentricity  $e$  against the inclination  $i$  based on the GMN shower identification, color coded according to the orbit similarity criteria. The triangles indicate the Andromedids which were identified as December psi Cassiopeids.

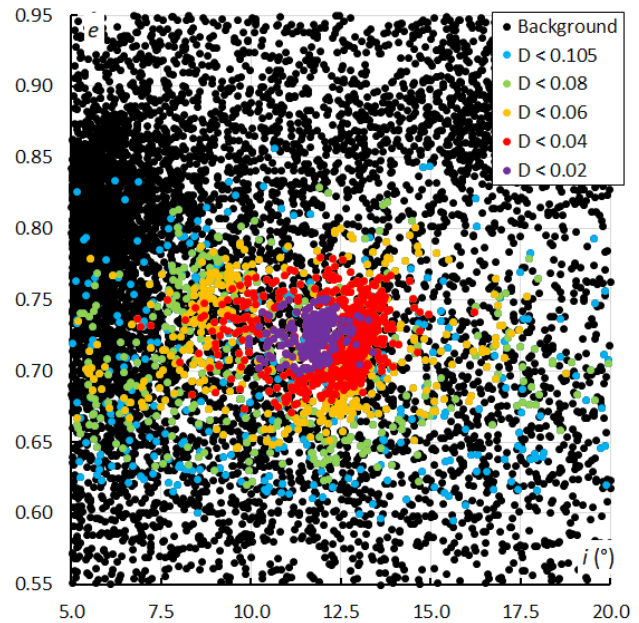


Figure 50 – The Andromedid orbits plotted as eccentricity  $e$  against the inclination  $i$  based on the orbit similarity shower identification, color coded according to the orbit similarity criteria.

The plot of the eccentricity  $e$  against the inclination  $i$  shows a concentration with the first peak Andromedid orbits at higher eccentricities with lower inclination and the second and third maximum Andromedids with slightly lower eccentricity at higher inclinations (Figure 49). The December psi Cassiopeids appear more dispersed mainly in inclination. The plot with the orbit similarity shower identification confirms the same trend, although many more dispersed orbits, including the December psi Cassiopeids were identified as Andromedids (Figure 50).

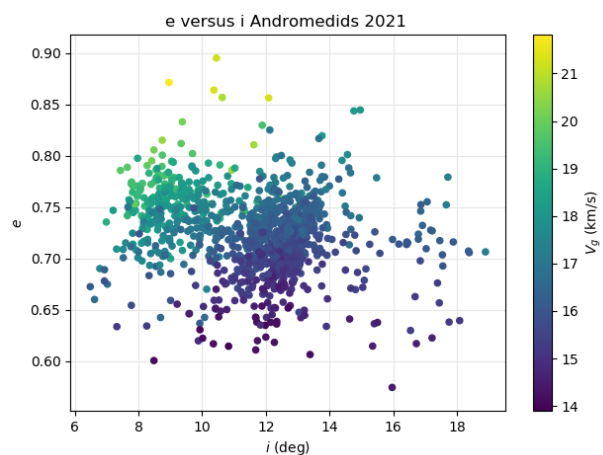
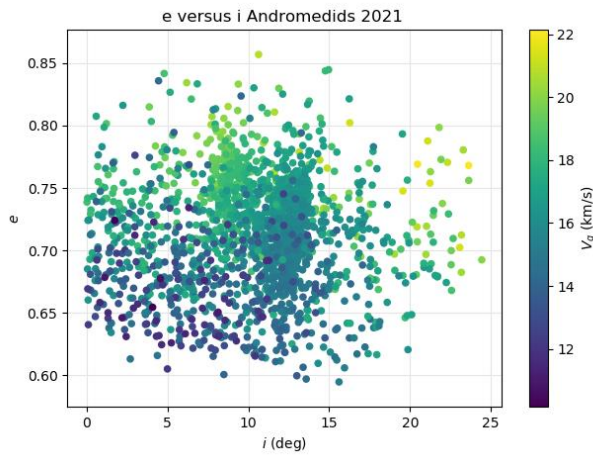


Figure 51 – The Andromedid orbits plotted as eccentricity  $e$  against the inclination  $i$  based on the GMN shower identification, color coded according to the geocentric velocity.

The same plot but with the velocity color coded (Figure 51) shows two more distinct concentrations with faster Andromedids with higher eccentricity and lower inclination during the first weeks of the activity with the first peak. The second and third peak occurred at higher inclination with slightly lower eccentricity and with lower velocity. The plot based on the orbit similarity (Figure 52) confirms this trend,

although with a larger dispersion in inclination. The lower the eccentricity and the lower the inclination, the slower the velocity. Four data points at high eccentricity in *Figure 51* have disappeared in *Figure 52* because the orbit similarity criteria rejected these orbits which were identified as Andromedids by GMN.



*Figure 52* – The Andromedid orbits plotted as eccentricity  $e$  against the inclination  $i$  based on the orbit similarity shower identification, color coded according to the geocentric velocity.

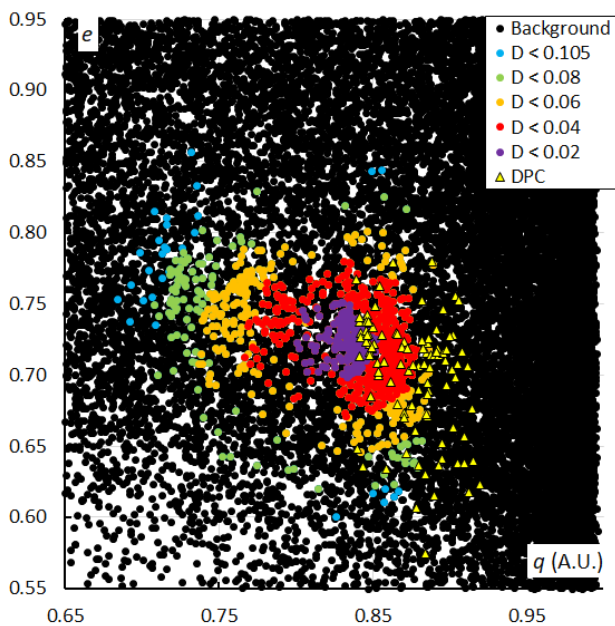


*Figure 53* – The Andromedid orbits plotted as eccentricity  $e$  against the perihelion distance  $q$  based on the GMN shower identification, color coded according to the orbit similarity criteria. The triangles indicate the Andromedids which were identified as December psi Cassiopeiids.

Plotting the eccentricity  $e$  against the perihelion distance  $q$ , a similar picture emerges as for the inclination. A first concentration can be seen at higher eccentricity and smaller perihelion distance, including the first peak. The other concentration at larger perihelion distance covers the second and the third peaks. the December psi Cassiopeiids fit in this plot with some larger dispersion after the main Andromedid activity (*Figure 53*). The plot based on the orbit similarity shower identification (*Figure 54*) confirms

this result with many more dispersed orbits identified as Andromedids.

The plot of eccentricity  $e$  against perihelion distance  $q$ , color coded for the velocity shows two distinct concentrations. The first concentration at smaller perihelion distances appears with the fastest Andromedids, the second concentration at larger perihelion distances at slightly lower eccentricity includes slower Andromedids (*Figure 55*).

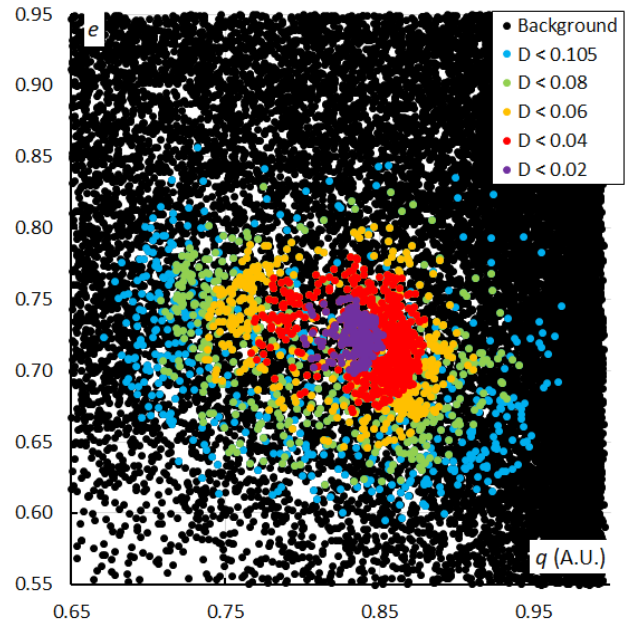


*Figure 54* – The Andromedid orbits plotted as eccentricity  $e$  against the perihelion distance  $q$  based on the orbit similarity shower identification, color coded according to the orbit similarity criteria.

The plot based on the orbit similarity shower identification displays a more diffuse picture, including more dispersed orbits. The higher the eccentricity and the smaller the perihelion distance, the faster the velocity, the larger the perihelion distance, the lower the eccentricity, the slower the velocity (*Figure 56*).

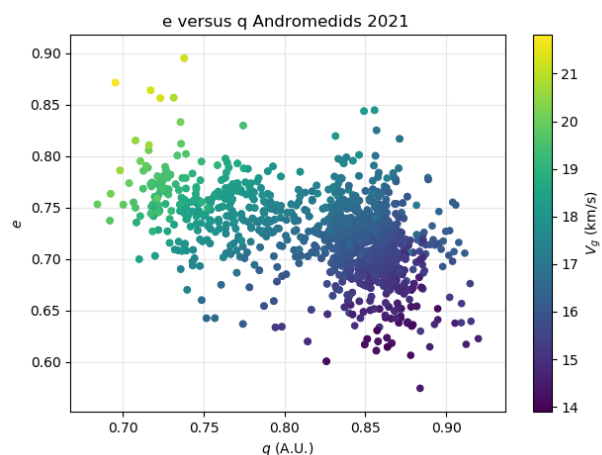


*Figure 55* – The Andromedid orbits plotted as eccentricity  $e$  against the perihelion distance  $q$  based on the GMN shower identification, color coded according to the geocentric velocity.

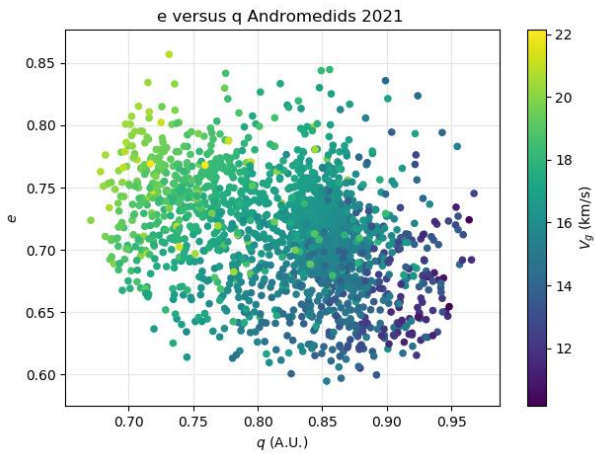


Figure 56 – The Andromedid orbits plotted as eccentricity  $e$  against the perihelion distance  $q$  based on the orbit similarity shower identification, color coded according to the geocentric velocity.

**The semi major axis  $a$**

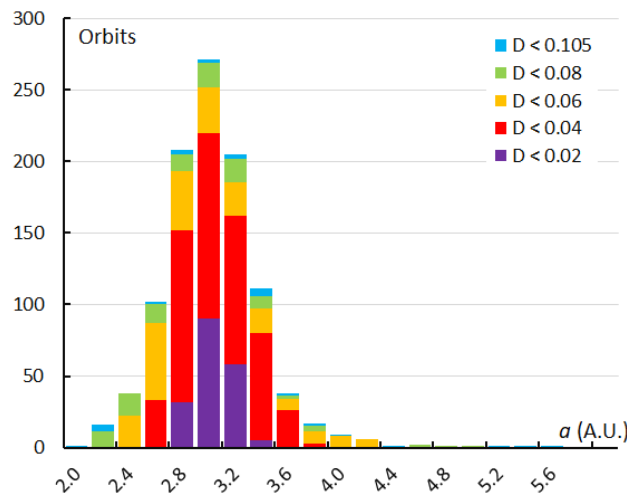


Figure 57 – The histogram with the distribution of the semi-major axis  $a$  obtained for Andromedids identified by the GMN shower identification method.

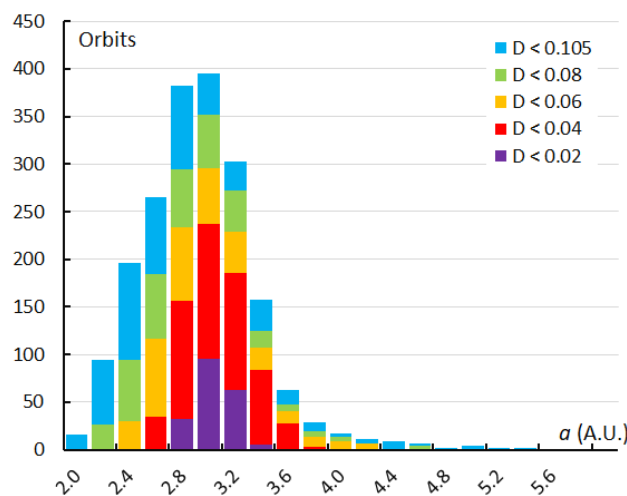


Figure 58 – The histogram with the distribution of the semi-major axis  $a$  obtained for Andromedids identified by the orbit similarity shower identification method.

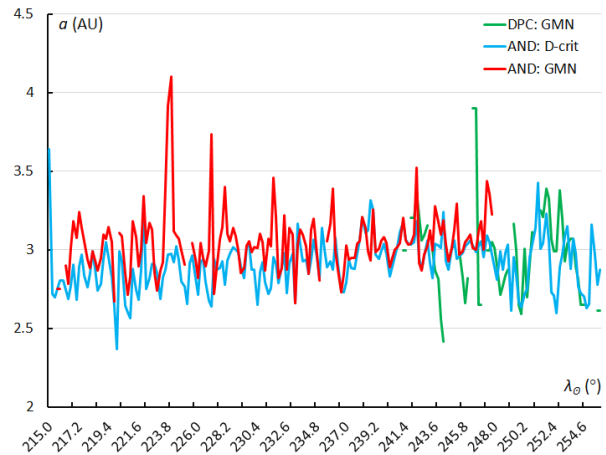


Figure 59 – The variation in semi-major axis  $a$ , using the sliding mean of the semi-major axis computed for a time interval of  $0.4^\circ$  in solar longitude in steps of  $0.2^\circ$ . The GMN shower identification is marked in red for the Andromedids and in green for the December psi Cassiopeids, the Andromedids according to the orbit similarity identification are marked in blue.

The semi major axis is the easiest element to visualize for an elliptic orbit and can be calculated using the perihelion distance  $q$  and the eccentricity  $e$  as:

$$a = \frac{q}{(1 - e)}$$

The semi-major axis is the most stable orbital element during the transit of Earth through the Andromedid stream, resulting in a symmetric profile in the histogram for both shower identification methods (Figures 57 and 58).

The values of the semi-major axis remain stable around 3.0 A.U. during the entire Andromedid activity (Figure 29) and the December psi Cassiopeids fit very well in this graph.

**6 Andromedid magnitude distribution**

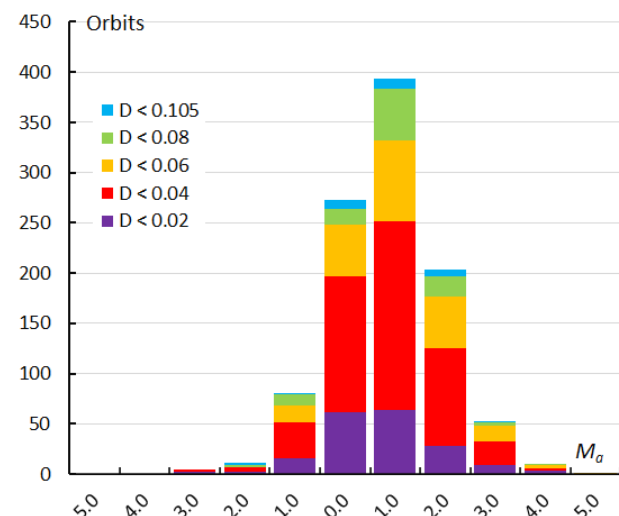


Figure 60 – The histogram with the distribution of the absolute magnitudes recorded for Andromedids identified by the GMN shower identification method.

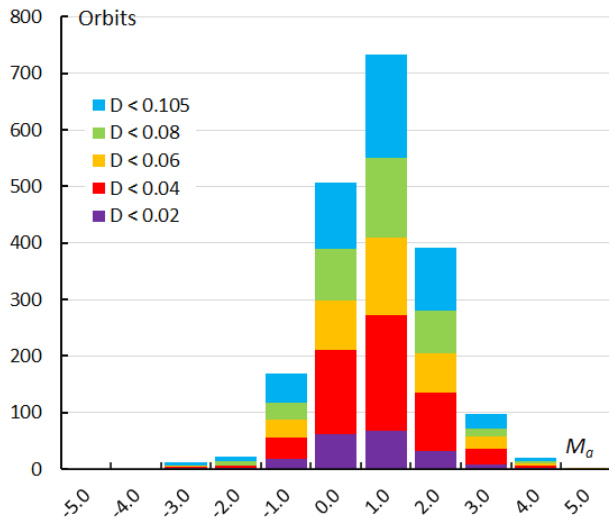


Figure 61 – The histogram with the distribution of the absolute magnitudes recorded for Andromedids identified by the orbit similarity shower identification method.

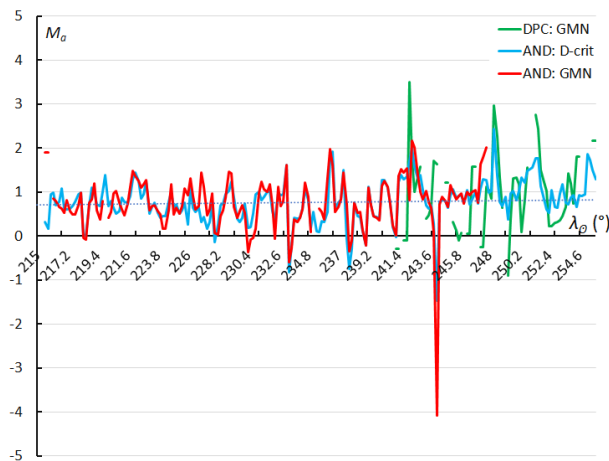


Figure 62 – The variation in absolute magnitude, using the sliding mean of the absolute magnitude computed for a time interval of 0.4° in solar longitude in steps of 0.2°. The GMN shower identification is marked in red for the Andromedids and in green for the December psi Cassiopeids, the Andromedids according to the orbit similarity identification are marked in blue.

Looking at the magnitude distribution, based on the absolute magnitudes derived from the measured intensity of the video recordings, the available data indicate that the Andromedids were mainly faint meteors. Apart from some isolated fireballs rather few bright Andromedids were recorded. The orbit similarity method seems to identify mainly more fainter shower members than the GMN method (Figures 60 and 61).

Looking at the average absolute magnitude during the activity period no trend or variation can be detected apart from scatter caused by some outliers (Figure 62).

## 7 The complex composition of the shower

The unusual radiant drift and significant change in orbital elements during the activity period make it impossible to identify these orbits correctly with a single mean orbit as reference. The radiant drift cannot be determined with a simple linear fit because of the unusual composition of the Andromedid shower. Masahiro Koseki (2021) studied the annual activity of the Andromedids based on SonotaCo orbit data for the period 2007–2018 and found the same radiant drift in Sun-centered ecliptic coordinates and the same trend in the changing orbital elements.

Instead of using a single reference orbit to try to identify Andromedid orbits, it would be more appropriate to use a matrix of orbital elements to take the significant changes in the orbital elements into account. In an attempt to visualize the effect of the selection of the reference orbit on the identification of Andromedid orbits and the subsequent activity profile; the mean orbit has been calculated based on a reference orbit obtained for different time intervals.

The mean orbits (Jopek, 1993), obtained with reference orbits valid for different time intervals have been listed in Table 1. First 7 intervals were used between solar longitude 215° and 250° in steps of 5°. Three mean orbits were obtained for the three shower maxima intervals, 222.5°–228.5°, 238.5°–242.5° and 245.6°–246.1°.

Table 1 – The mean orbits for the Andromedids identified with a reference orbit calculated for a specific range of GMN-identified orbits.

Range ref.	$\lambda_0$	$\alpha_g$	$\delta_g$	$\lambda_g - \lambda_0$	$\beta_g$	$v_g$	$a$	$q$	$e$	$i$	$\Omega$	$\omega$	$N$
$\lambda_0$ (°)	(°)	(°)	(°)	(°)	(°)	km/s	A.U.	A.U.		(°)	(°)	(°)	D < 0.04
215–220	217.65	20.6	22.2	169.9	12.5	19.0	2.96	0.722	0.7555	8.4	218.22	248.43	221
220–225	222.57	22.0	25.3	167.4	14.9	18.3	3.00	0.749	0.7502	9.0	222.70	244.62	279
225–230	227.44	23.2	28.1	164.6	17.0	17.4	2.96	0.776	0.7376	9.5	227.48	240.65	295
230–235	232.21	23.7	32.4	162.1	20.8	16.9	3.01	0.807	0.7315	10.3	232.46	235.65	507
235–240	238.71	25.2	37.6	159.0	25.2	16.2	2.99	0.832	0.7216	11.6	238.90	231.36	754
240–245	242.55	25.7	41.4	157.3	28.5	15.9	2.98	0.849	0.7155	12.2	242.49	228.39	758
245–250	246.54	25.6	44.3	154.7	31.2	15.5	3.01	0.865	0.7129	13.0	246.00	225.26	739
222.5–228.5	225.25	22.6	27.1	166.0	16.3	17.8	2.94	0.772	0.7372	9.3	227.03	241.37	297
238.5–242.5	240.45	25.6	39.7	158.5	26.9	16.2	2.99	0.839	0.7191	11.8	240.38	230.24	758
245.6–246.1	245.84	25.8	44.6	155.5	31.4	15.7	3.00	0.864	0.7124	12.9	245.80	225.54	742
DPC	243.63	25.6	42.7	156.1	30.0	15.8	2.92	0.874	0.7009	14.77	248.39	222.52	656

The mean orbit for the December psi Cassiopeiids identified by the GMN shower identification method has been used as reference orbit too (DPC).

This study has been based on a single reference orbit used to identify Andromedids independently from the GMN shower identification. The mean orbit taken for the entire activity period is a compromise and may fail to identify Andromedids at the start and at the end of the activity period. Using a series of reference orbits based on different activity intervals, we can consider the activity profile according to these different reference orbits. The relevance of these reference orbits in *Table 1* is given by the number of orbits that fulfil the high threshold similarity  $D_D < 0.04$  (*Table 1*). The resulting profiles are presented in *Figures 63 to 73*. The influence of the chosen reference orbit is obvious. The terms “peak” and “maximum” are very relative as these refer to activity levels of maximum 35% of the sporadic background activity.

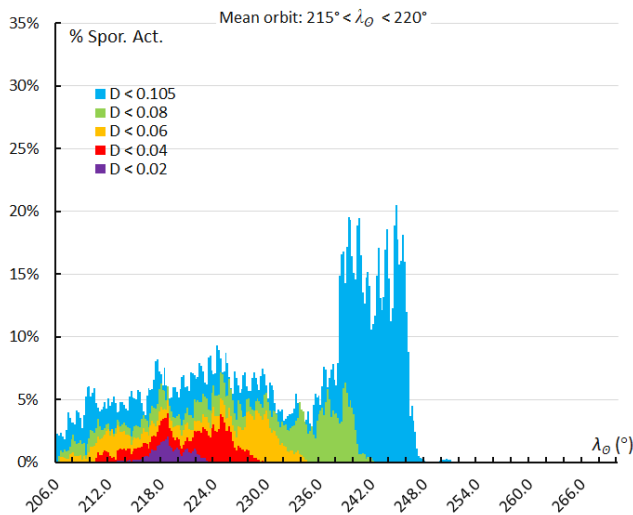


Figure 63 – The activity profile based on the orbit similarity shower identification using a reference orbit derived for the activity interval  $215^\circ < \lambda_0 < 220^\circ$ .

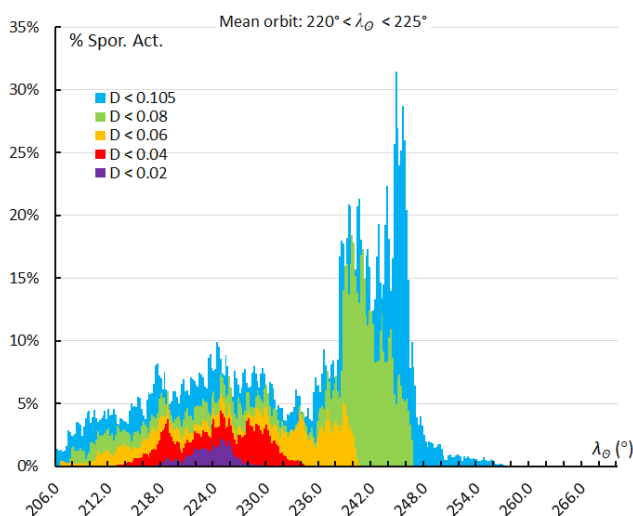


Figure 64 – The activity profile based on the orbit similarity shower identification using a reference orbit derived for the activity interval  $220^\circ < \lambda_0 < 225^\circ$ .

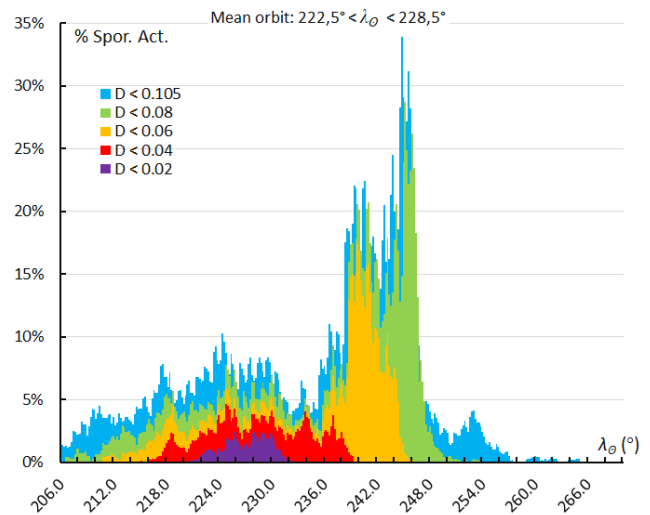


Figure 65 – The activity profile based on the orbit similarity shower identification using a reference orbit derived for the activity interval  $222.5^\circ < \lambda_0 < 228.5^\circ$ , the first maximum.

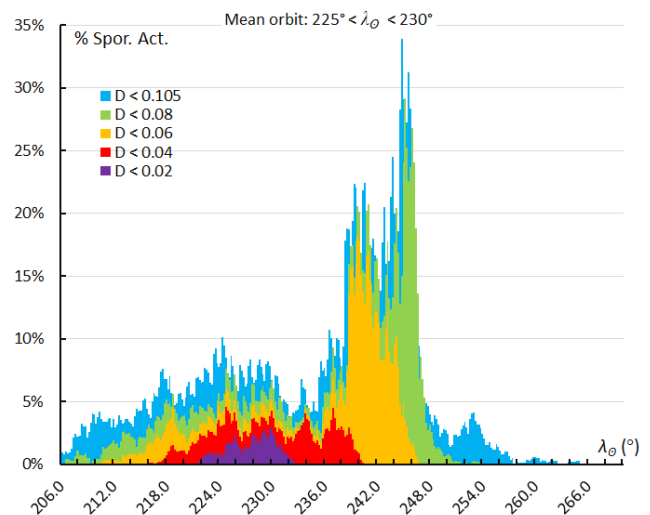


Figure 66 – The activity profile based on the orbit similarity shower identification using a reference orbit derived for the activity interval  $225^\circ < \lambda_0 < 230^\circ$ .

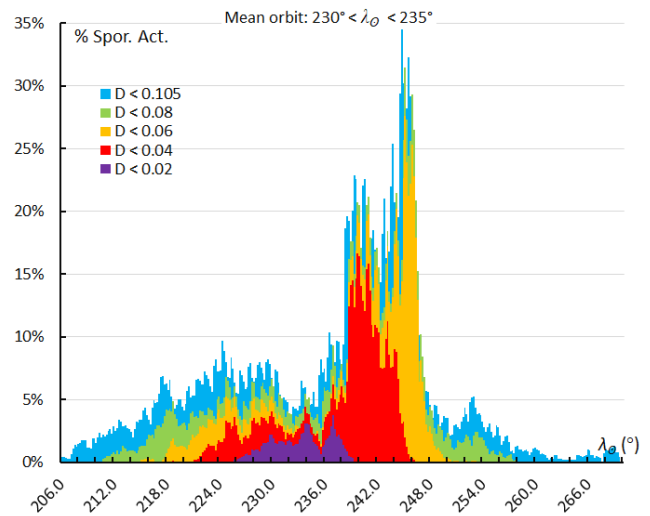


Figure 67 – The activity profile based on the orbit similarity shower identification using a reference orbit derived for the activity interval  $230^\circ < \lambda_0 < 235^\circ$ .

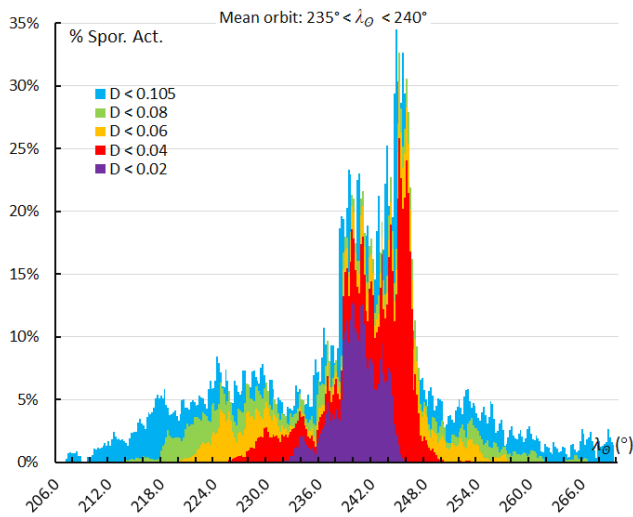


Figure 68 – The activity profile based on the orbit similarity shower identification using a reference orbit derived for the activity interval  $235^\circ < \lambda_0 < 240^\circ$ .

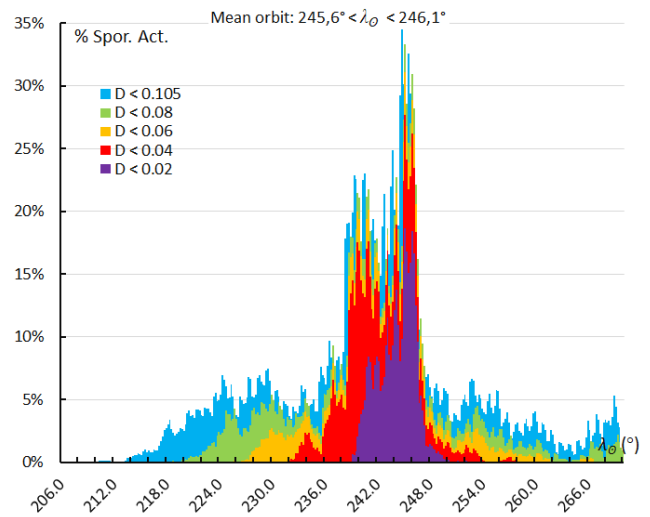


Figure 71 – The activity profile based on the orbit similarity shower identification using a reference orbit derived for the activity interval  $245.6^\circ < \lambda_0 < 246.1^\circ$ , the third and final sharp maximum.

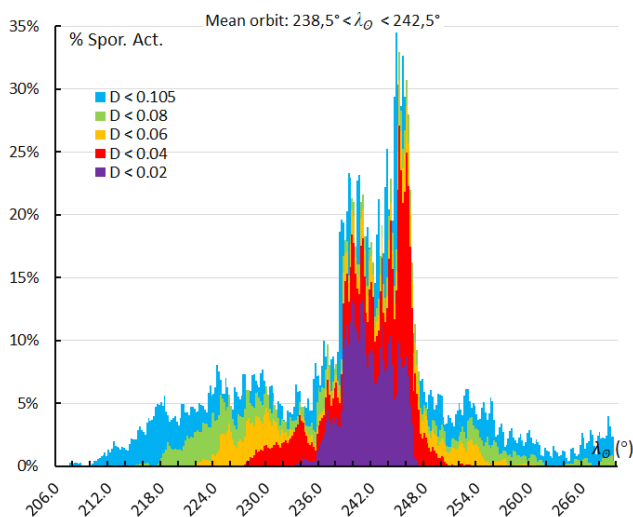


Figure 69 – The activity profile based on the orbit similarity shower identification using a reference orbit derived for the activity interval  $238.5^\circ < \lambda_0 < 242.5^\circ$ , the second maximum.

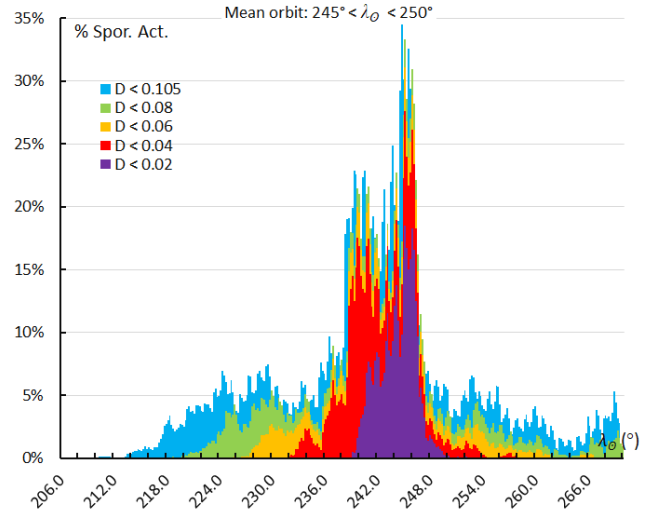


Figure 72 – The activity profile based on the orbit similarity shower identification using a reference orbit derived for the activity interval  $245^\circ < \lambda_0 < 250^\circ$ .

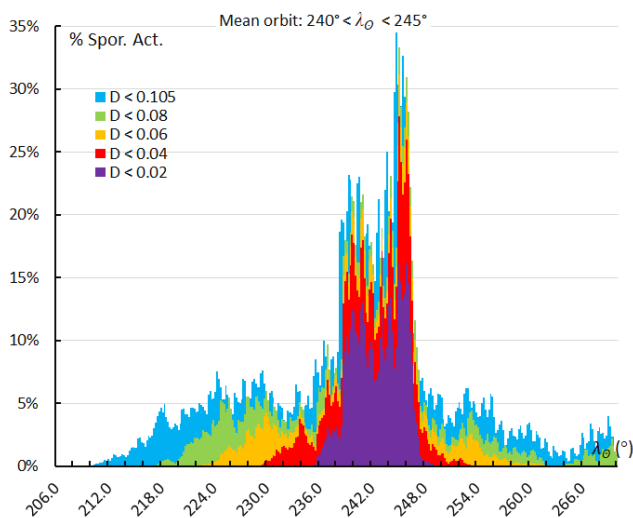


Figure 70 – The activity profile based on the orbit similarity shower identification using a reference orbit derived for the activity interval  $240^\circ < \lambda_0 < 245^\circ$ .

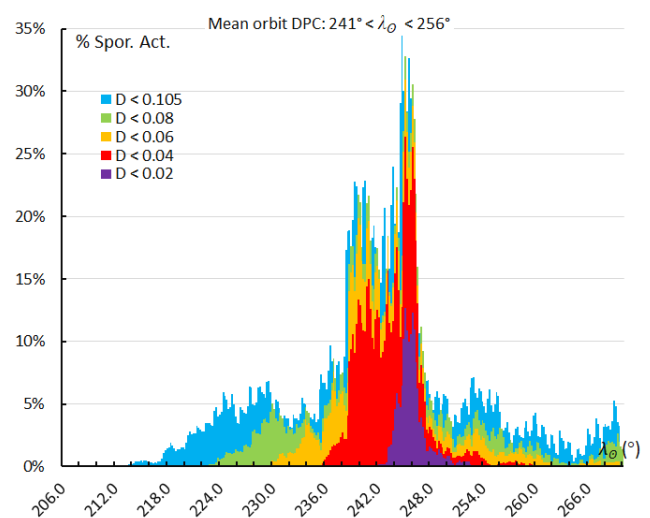


Figure 73 – The activity profile based on the orbit similarity shower identification using a reference orbit derived for the activity interval  $241^\circ < \lambda_0 < 256^\circ$  with the December psi Cassiopeiid orbits identified by GMN.

## 8 Conclusions

The analysis of the available Andromedid and December psi Cassiopeiid orbits obtained by the Global Meteor Network allowed a detailed picture to be established of the structure of this stream during the enhanced activity observed during 2021. The hourly rates remained very low at 35% of the sporadic rates at best. This is barely noticeable for an uninformed visual observer.

The activity period could be confirmed for at least the interval  $206^\circ < \lambda_\odot < 278^\circ$  or roughly October 20 till end of December. This activity period is considerably longer than previously assumed and definitely longer than what has been assumed for the automatic GMN shower identification. The shower meteors were identified according to the GMN shower association and independently with the orbit similarity method. Although the latter identifies almost twice as many Andromedid orbits than the GMN method, all essential conclusions in this study remain the same for both identification methods.

The activity profile reveals three different maxima, a first enhanced activity during several nights around  $\lambda_\odot \sim 234^\circ$ , a second more compact concentration at  $\lambda_\odot \sim 239.4^\circ$  and a final short duration concentration at  $\lambda_\odot \sim 246.0^\circ$ . Beyond these time intervals, the activity remained very low at less than 5% of the sporadic activity.

The usual radiant drift caused by the rotation of the Earth around the Sun is partly compensated by the changing orbital orientation. This explains the disagreement in radiant drift between different sources as these depend on the activity interval taken into consideration for the radiant drift. In case of the Andromedids, the radiant drift cannot be determined with an ordinary linear regression with a steady increment in R.A. and declination.

The orbital elements show an evolution in time, the longitude of perihelion  $II$ , the inclination  $i$ , and especially the perihelion distance  $q$  increase during the activity period. The eccentricity  $e$  decreases and the semi major axis  $a$  remains constant. The distribution of the orbital elements shows distinct concentrations within the Andromedid complex.

A single reference orbit and radiant position cannot identify all shower members. A range of orbits or an orbit matrix is required to cover the structure of this complex shower. The influence of the choice of the reference orbit on the identification of Andromedid orbits has been shown. Taking the drift in orbital elements into account to define a set of reference orbits to apply the D-criteria could result in an improved shower identification. It is not expected that this would lead to significant different conclusions. It is obvious that the Andromedid meteoroid stream suffered severe perturbations to an extent that it should be considered as a shower complex rather than as a single meteoroid stream.

## Acknowledgment

This report is based on the data of the Global Meteor Network which is released under the CC BY 4.0 license<sup>1</sup>. The GMN project is volunteers' work. All hardware is purchased and all operational costs are covered by the participants themselves. The authors thank the camera operators and everyone who has been somehow contributing to the Global Meteor Network for their efforts to keep the network operational: *Richard Abraham, Victor Acciari, Rob Agar, David Akerman, Daknam Al-Ahmadi, Jamie Allen, Alexandre Alves, Željko Andreić, Martyn Andrews, Miguel Angel Diaz, Enrique Arce, Georges Attard, Chris Baddiley, David Bailey, Roger Banks, Hamish Barker, Jean-Philippe Barrilliot, Richard Bassom, Ricky Bassom, Ehud Behar, Josip Belas, Alex Bell, Serge Bergeron, Denis Bergeron, Jorge Bermúdez Augusto Acosta, Steve Berry, Adrian Bigland, Chris Blake, Arie Blumenzweig, Ventsislav Bodakov, Claude Boivin, Robin Boivin, Bruno Bonicontró, Fabricio Borges, Ubiratan Borges, Dorian Božičević, David Brash, Ed Breuer, Martin Breukers, John W. Briggs, Peter G. Brown, Laurent Brunetto, Tim Burgess, Ludger Börgerding, Sylvain Cadieux, Peter Campbell-Burns, Andrew Campbell-Laing, Pablo Canedo, Seppe Canonaco, Jose Carballada, Steve Carter, David Castledine, Gilton Cavallini, Brian Chapman, Jason Charles, Matt Cheselka, Tim Claydon, Trevor Clifton, Manel Coldecarrera, Michael Cook, Bill Cooke, Christopher Coomber, Brendan Cooney, Edward Cooper, Jamie Cooper, Andrew Cooper, Marc Corretgé Gilart, Paul Cox, Llewellyn Cupido, Christopher Curtis, Ivica Ćiković, Dino Čaljkusić, Chris Dakin, Alfredo Dal'Ava Júnior, James Davenport, Richard Davis, Steve Dearden, Christophe Demeautis, Bart Dessoy, Paul Dickinson, Ivo Dijan, Pieter Dijkema, Tammo Jan Dijkema, Marcelo Domingues, Stacey Downton, Zoran Dragić, Iain Drea, Igor Duchaj, Jean-Paul Dumoulin, Garry Dymond, Jürgen Dörr, Robin Earl, Howard Edin, Ollie Eisman, Carl Elkins, Ian Graham Enting, Peter Eschman, Bob Evans, Andres Fernandez, Barry Findley, Rick Fischer, Richard Fleet, Jim Fordice, Jean Francois Larouche, Kyle Francis, Patrick Franks, Gustav Frisholm, Enrique Garcilazo Chávez, José García María, Mark Gatehouse, Ivan Gašparić, Chris George, Megan Gialluca, Kevin Gibbs-Wragge, Jason Gill, Philip Gladstone, Uwe Glässner, Hugo González, Nikola Gotovac, Neil Graham, Pete Graham, Colin Graham, Sam Green, Bob Greschke, Daniel J. Grinkevich, Larry Groom, Dominique Guiot, Tioga Gulon, Margareta Gumilar, Peter Gural, Nikolay Gusev, Kees Habraken, Alex Haislip, John Hale, Peter Hallett, Graeme Hanigan, Erwin Harkink, Ed Harman, Marián Harnádek, Ryan Harper, David Hatton, Tim Havens, Mark Haworth, Paul Haworth, Richard Hayler, Sam Hemmelgarn, Rick Hewett, Don Hladiuk, Alex Hodge, Simon Holbeche, Jeff Holmes, Nick Howarth, Matthew Howarth, Jeff Huddle, Bob Hufnagel, Roslina Hussain, Russell Jackson, Jean-Marie Jacquart, Jost Jahn, Phil James, Ron James Jr, Nick James, Rick James, Ilya Jankowsky, Alex Jeffery, Klaas*

<sup>1</sup> <https://creativecommons.org/licenses/by/4.0/>

Jobse, Richard Johnston, Dave Jones, Fernando Jordan, Vladimir Jovanović, Jocimar Justino de Souza, Javor Kac, Richard Kacerek, Milan Kalina, Jonathon Kambulow, Steve Kaufman, Paul Kavanagh, Alex Kichev, Harri Kiiskinen, Jean-Baptiste Kikwaya, Sebastian Klier, Dan Klinglesmith, John Kmetz, Zoran Knez, Korado Korlević, Stanislav Korotkiy, Danko Kočiš, Josip Krpan, Zbigniew Krzeminski, Patrik Kukić, Reinhard Kühn, Remi Lacasse, Gaétan Laflamme, Steve Lamb, Hervé Lamy, Jean Larouche Francois, Ian Lauwerys, David Leurquin, Gareth Lloyd, Rob Long De Corday, Eric Lopez, Jose Lopez Galindo, José Luis Martin, Juan Luis Muñoz, Pete Lynch, Frank Lyter, Anton Macan, Jonathan Mackey, John Maclean, Igor Macuka, Nawaz Mahomed, Simon Maidment, Mirjana Malarić, Nedeljko Mandić, Alain Marin, Bob Marshall, Colin Marshall, Andrei Marukhno, Keith Maslin, Nicola Masseroni, Bob Massey, Jacques Masson, Damir Matković, Filip Matković, Dougal Matthews, Michael Mazur, Sergio Mazzi, Stuart McAndrew, Alex McConahay, Robert McCoy, Charlie McCormack, Mark McIntyre, Peter Meadows, Edgar Merizio Mendes, Aleksandar Merlak, Filip Mezak, Pierre-Michael Micaletti, Greg Michael, Matej Mihelčić, Simon Minnican, Wullie Mitchell, Edson Morales Valencia, Nick Moskovitz, Dave Mowbray, Andrew Moyle, Gene Mroz, Muhammad Muharam Luqmanul Hakim, Brian Murphy, Carl Mustoe, Przemek Nagański, Jean-Louis Naudin, Damjan Nemarnik, Attila Nemes, Dave Newbury, Colin Nichols, Nick Norman, Philip Norton, Zoran Novak, Gareth Oakey, Washington Oliveira, Angélica Olmos López, Jamie Olver, Christine Ord, Nigel Owen, Michael O'Connell, Dylan O'Donnell, Thiago Paes, Carl Panter, Neil Papworth, Filip Parag, Gary Parker, Simon Parsons, Ian Pass, Igor Pavletić, Lovro Pavletić, Richard Payne, Pierre-Yves Pechart, William Perkin, Enrico Pettarin, Alan Pevec, Mark Phillips, Patrick Poitevin, Tim Polfriet, Derek Poulton, Janusz Powazki, Aled Powell, Alex Pratt, Miguel Preciado, Chuck Pullen, Terry Pundiak, Lev Pustil'Nik, Dan Pye, Chris Ramsay, David Rankin, Steve Rau, Dustin Rego, Chris Reichelt, Danijel Reponj, Fernando Requena, Maciej Reszelsk, Ewan Richardson, Martin Richmond-Hardy, Mark Robbins, David Robinson, Martin Robinson, Heriton Rocha, Herve Roche, Adriana Roggemans, Paul Roggemans, Alex Roig, David Rollinson, Jim Rowe, Dmitrii Rychkov, Michel Saint-Laurent, Clive Sanders, Jason Sanders, Ivan Sardelić, Rob Saunders, John Savage, Lawrence Saville, Vasili Savtchenko, William Schauf, Ansgar Schmidt, Jim Sergeant, Jay Shaffer, Steven Shanks, Mike Shaw, Angel Sierra, Ivo Silvestri, Ivica Skokić, Dave Smith, Tracey Snelus, Warley Souza, Mark Spink, Denis St-Gelais, James Stanley, Radim Stano, Laurie Stanton, Robert D. Steele, Yuri Stepanychev, Graham Stevens, Peter Stewart, William Stewart, Con Stoitsis, Andrea Storani, Andy Stott, David Strawford, Rajko Sušan, Bela Szomi Kralj, Marko Šegon, Damir Šegon, Jeremy Taylor, Yakov Tchenak, Eric Toops, Torcuill Torrance, Steve Trone, Wenceslao Trujillo, John Tuckett, Myron Valenta, Jean Vallieres, Paraksh Vankawala, Neville Vann, Marco Verstraaten, Arie Verveer, Denis Vida, Predrag Vukovic, Martin Walker, Aden Walker, Bill Wallace, John Waller,

Jacques Walliang, Didier Walliang, Jacques Walliang, Christian Wanlin, Tom Warner, Neil Waters, Steve Welch, Alexander Wiedekind-Klein, John Wildridge, Ian Williams, Guy Williamson, Urs Wirthmueller, Bill Witte, Martin Woodward, Jonathan Wyatt, Anton Yanishevskiy, Penko Yordanov, Stephane Zanoni, Dario Zubović, Pierre de Ponthière, Erwin van Ballegoij, Edison Álvarez José Felipe Pérezgómez.

## References

- Drummond J. D. (1981). "A test of comet and meteor shower associations". *Icarus*, **45**, 545–553.
- Jenniskens P. (2006). *Meteor Showers and their Parent Comets*. Cambridge, UK: Cambridge University Press, 2006.
- Jenniskens P., Vaubaillon J. (2007). "3D/Biela and the Andromedids: Fragmenting versus Sublimating Comets". *Astronomical Journal*, **134**, 1037–1045.
- Jenniskens P., Nénon Q., Albers J., Gural P. S., Haberman B., Morales R., Grigsby B. J., Samuels D., Johannink C. (2016). "The established meteor showers as observed by CAMS". *Icarus*, **266**, 331–354.
- Jenniskens P., Baggaley J., Crumpton I., Aldous P., Pokorny P., Janches D., Gural P. S., Samuels D., Albers J., Howell A., Johannink C., Breukers M., Odeh M., Moskovitz N., Collison J. and Ganjuag S. (2018). "A survey of southern hemisphere meteor showers". *Planetary Space Science*, **154**, 21–29.
- Jenniskens P. (2022a). "An outburst of Andromedids (AND#0018) in 2021". *eMetN*, **7**, 1–2.
- Jenniskens P. and Moskovitz N. (2022b). "An outburst of Andromedids on November 28, 2021". *eMetN*, **7**, 3–5.
- Jopek T. J. (1993). "Remarks on the meteor orbital similarity D-criterion". *Icarus*, **106**, 603–607.
- Jopek T. J., Rudawska R. and Pretka-Ziomek H. (2006). "Calculation of the mean orbit of a meteoroid stream". *Monthly Notices of the Royal Astronomical Society*, **371**, 1367–1372.
- Koseki M. (2021). "The activity of meteor showers recorded by SonotaCo Net video observations 2007–2018, AND (#0018)". *eMetN*, **6**, 185–186.
- Kronk G. (1988). *Meteor Showers: A Descriptive Catalog*. Hillside, New Jersey, USA: Enslow Publishers.
- Moorhead A., Clements T.D. and Vida D. (2020). "Realistic gravitational focusing of meteoroid streams". *Monthly Notices of the Royal Astronomical Society*, **494**, 2982–2994.

- Roggemans P., Johannink C. and Cambell-Burns P. (2019). “October Ursae Majorids (OCU#333)”. *eMetN*, **4**, 55–64.
- SonotaCo (2009). “A meteor shower catalog based on video observations in 2007-2008”. *WGN, Journal of the International Meteor Organization*, **37**, 55–62.
- Southworth R. R. and Hawkins G. S. (1963). “Statistics of meteor streams”. *Smithson. Contrib. Astrophys.*, **7**, 261–286.
- Vida D., Šegon D., Gural P. S., Brown P. G., McIntyre M. J. M., Dijkema T. J., Pavletić L., Kukić P., Mazur M. J., Eschman P., Roggemans P., Merlak A., Zubrović D. (2021). (2021). “The Global Meteor Network – Methodology and first results”. *Monthly Notices of the Royal Astronomical Society*, **506**, 5046–5074.
- Wiegert P. A., Brown P. G., Weryk R. J., Wong D. K. (2013). “The return of the Andromedids meteor shower”. *Astronomical Journal*, **145**, 70–81.

# A statistical analysis of BRAMON TV meteors light curve data obtained in 2014 and 2015

A. S. Betzler<sup>1</sup> and Orahcio F. de Sousa<sup>2</sup>

<sup>1</sup> Centro de Ciência e Tecnologia em Energia e Sustentabilidade, Universidade Federal do Recôncavo da Bahia, Feira de Santana, Bahia, 44.085-132, Brazil  
betzler@ufrb.edu.br

<sup>2</sup> Centro de Formação de Professores, Universidade Federal do Recôncavo da Bahia, Amargosa 45.300-000, Brazil

The Brazilian Meteor Observation Network (BRAMON) is a meteor detection network that has been implemented in Brazil since 2014. BRAMON observed about 31 thousand meteors, of which 6% were observed simultaneously by two or more stations during 2014 and 2015. We have made a statistical analysis of some meteor showers and sporadic meteors of this homogeneous set of light curves and dynamic data. The distribution of meteor light curve durations for the SDA and SPO do not vary between 2014 and 2015. This similarity could be associated with the dependence of this duration with meteor altitude variation and the zenithal component of the geocentric velocity. About 79% of the light curves with duration  $\geq 0.3$  s, are convex in our sample. The  $F$  parameter has no dependency on the parent body, meteor shower complex, or kinematic parameters. The median  $F$  equals 0.56, suggesting that these meteors' light curves are late-peaked.

## 1 Introduction

Meteors are luminous phenomena that occur in the upper atmosphere. The spatial perspective of the meteor's trajectory is completely lost if the meteor is seen from a single point on the Earth's surface. The trajectory is projected on a sky background that varies with the location of the observation. Different stellar backgrounds observed from multiple sites allow the reconstruction of the geometry of the meteor's appearance. For that, the observations must happen in a common volume of the Earth's atmosphere. This common trajectory can be deduced from observations made with the naked eye, photographic or TV cameras, or radar. The first observations with dual photographic cameras were started in 1936 at the Harvard Observatory (USA) (McCrosky and Boeschenstein, 1965) and the Ondrejov Observatory (former Czechoslovakia) in 1951 (Bland, 2004). High-sensitivity, low-cost TV cameras of the order of  $10^{-4}$  lux became common from the early 2000s. As a result, there was a significant increase in the number of amateur and professional meteor monitoring networks spread across Europe and the American continent, totaling more than a dozen projects. The common aims of most of these initiatives are the studies of dynamic (atmospheric trajectory and orbit) and physical (magnitude, mass, and chemical composition) properties of meteors. One of the largest monitoring networks in the southern hemisphere is the Brazilian Meteor Observation Network (BRAMON). BRAMON started operating with nine stations in its first year, and had 23 cameras in 2015. Most stations are located in south-central Brazil, where the largest urban centers Rio de Janeiro and São Paulo are located, and the rest in the central, northeast, and west of the country. The stations are equipped with a TV camera capable of recording astrometric and photometric data from meteors, allowing the study of the dynamic and physical properties of the

meteors. BRAMON recorded 30768 single meteors between 2014 January and 2015 September, which were separated into 392 different meteor showers from the list of the International Astronomical Union Meteor Data Center (IAU MDC) and the sporadic meteors (SPO). 2035 paired meteors were observed as double or multiple station events in the same period.

We performed a statistical analysis of the light curve photometric parameters (duration  $T$  and skewness  $F$  parameters) from meteors observed by BRAMON between 2014 and 2015.



Figure 1 – The spatial disposition of BRAMON stations in the territory of Brazil (points) in 2014 and 2015. Three major metropolitan centers had stations at that time: Brasília, João Pessoa, and São Paulo. Some stations can have two or more cameras pointed to different azimuths for pairings with adjacent observational sites.

## 2 The data

The main component of a meteor observation station is its camera whose efficiency is limited by its sensor, sky brightness, and detection software. Between 2014 and 2015, a typical BRAMON station was equipped with a Samsung SCB 2000 camera, which uses a Sony Super HAD 1/3 CCD sensor, and is capable of registering light sources up to 0.05 lux intensity. These cameras were modified with the removal of the infrared (IR) filter, and a Varifocal Ai 3-8mm Dc F1.0 Ltvr-3 lens was combined. This lens provided a field of view (FoV) of  $\sim 70 \times 60$  degrees for the shortest focal length. The 23 BRAMON operators had 27 stations, 60% of which were located in small urban centers, with a low level of light pollution. BRAMON stations are distributed below the equator, concentrating near the Tropic of Capricorn (*Figure 1*). The geographical disposition of the stations allowed the detection of meteors in a declination range between  $-90$  and  $+60$  degrees. BRAMON uses the UFOCAPTURE software to detect meteors. UFOCAPTURE works in conjunction with the UFOANALYSER and UFOORBIT programs that make it more suitable for studying meteors. UFOANALYSER classifies the detected objects (meteors, airplanes, insects, etc.) in the videos. Each class is defined using configurable parameters such as brightness, pixel dimensions, geometry, and duration. For astrometry, a celestial map is superimposed on an image extracted from the recorded video to obtain the position in the sky (right ascension and declination) and the apparent magnitude of the object as a function of time. The UFOORBIT program combines observations from different stations and calculates trajectories and orbits of meteoroids. This program has internal quality criteria that automatically reject pairs of observations with low precision or with a path geometry considered to be unrealistic. For this task, UFOORBIT has four quality factors for determining dynamic parameters of a meteor:  $Q_0$  combines data from several stations based on a given time interval ( $D_T$ ) in which the same meteor is observed at several stations;  $Q_1$  rejects fictional meteors,  $Q_2$  excludes ill-defined radiants and  $Q_3$  discards meteors with ill-determined speeds. The orbital elements generated by UFOORBIT are a mix of data with uncertainties that vary according to the number of stations that simultaneously registered the meteor, duration of the light phase, angle implied by the trajectory recorded in the camera's field of view, etc. The data considered in *Section 3* were processed using conditions  $Q_0$ , which by definition are more permissive, but which maximize the number of available orbits. However, it is perfectly possible to change the standard processing criteria to exclude ill-defined orbits. This was done in the reduction of BRAMON data. The applied criteria are shown in *Table 2* by Kornos et al. (2013).

Vereš and Toth (2010) analyzed the classification of meteors generated by UFOORBIT and by the D-criterion (Southworth and Hawkins, 1963). According to the D-criterion, a small fraction of the SPO population is contaminated by meteors associated with meteor showers,

which were poorly classified by UFOORBIT. The median contamination of the SPO population is 6.4% with a maximum value of 15.2%. We consider these percentages small so that the dynamic classifications performed by the set of UFOCAPTURE programs allow a robust population to study the BRAMON meteors within the scope of this work.

Hajduková et al. (2017) suggested that the orbital eccentricity of GEM meteors is influenced by the accuracy in determining meteor velocities. *Table 3* by Hajduková et al. (2017) suggests that the weighted average orbital elements generated by EDMOND and SonotoCo, both users of the UFO programs, and four other meteor detection networks present varied deviations from equivalent quantities generated by radar or photographic observations, in addition to having essentially similar dispersion. Based on the previous information, we conclude that the distributions of the orbital elements generated by the UFO programs, as well as other meteor detection networks, have systematic and random errors. Random errors can be associated with positional measurements of meteors in the sky extracted from trajectories recorded in a way that is not always favorable in the camera's FoVs. Systematic errors are due to the use of different methodologies to obtain velocities and orbits.

Statistical hypothesis tests applied on datasets reduced with different procedures can generate questionable results due to systematic errors. This effect is not manifested in the comparisons between BRAMON data because it comes from the same detection network, composed of similar cameras, and reduced with the same methodology.

The independent samples  $t$ -test has been used as a criterion for testing the non-similarity ("null hypothesis") between the analyzed distributions of various meteor physical parameters throughout this work. A large  $p$ -value (greater than confidence level  $\alpha = 0.05$ ) indicates strong evidence against the null hypothesis. The  $t$ -test is a parametric test that makes the comparison between means of each observed distribution, using their variance and the sample size.

We have analyzed two meteor light curve parameters: the skewness parameter  $F$  and the light curve duration. The duration of the light emission of a meteor is defined by the time interval between the beginning and the end of the detection of a meteor in a given season.

The most common measures of central tendency are the arithmetic mean, the median, and the mode. Central tendency estimators are extremely important because they provide a typical value in the sample, regardless of their dispersion. The choice of the best estimator is complex and depends a lot on the shape of the distribution (symmetrical or asymmetric). For a distribution that is of the Gaussian type, the mean is the most reasonable estimator. For an asymmetric distribution such as that observed in the duration  $T$  and  $F$  parameter, a better estimator would be the median, as it is not influenced by extreme values.

We compared the means using the  $t$ -test for its common use as a central tendency estimator in physics and astronomy.

The detected meteors were separated by meteor showers and sporadic meteors (SPO). We consider meteors associated with meteoroid streams from EDMOND’s J8 radiant catalog, which are connected with the IAU MDC working list of meteor showers (Kornoš et al., 2014). The association of meteors with meteor showers is based on the 2014 and 2015 versions of these catalogs, but updates have been added based on the current classification scheme (January 2022), based on the list of all meteor showers of the Meteor Data Center.

### 3 Analysis

#### 3.1 Duration of meteor light curves

Brosch et al. (2004) have shown that the duration of the luminous phase of a meteor is the one of most important light curve parameters to differentiate the 2002 LEO meteor light curves. We have compared distributions of visible light curve duration between different meteor showers to investigate this idea. We analyzed the distribution of visible light curve duration of meteors belonging to the SDA (Southern delta Aquariids) in 2014, CAP (alpha Capricornids), ETA (eta Aquariids), GEM (Geminids), SDA, PER (Perseids) SIA (Southern iota Aquariids), and STA (Southern Taurids) in 2015. The sporadic meteors (SPO) were observed in both observing seasons. All analyzed meteors in this section have been observed as double or multiple station events.

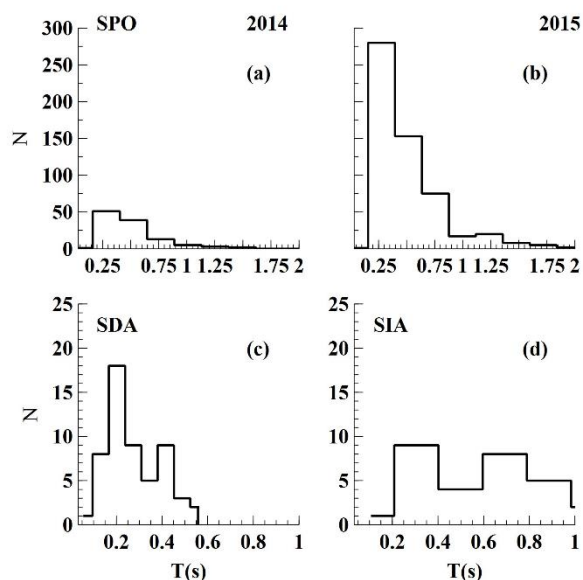


Figure 2 – Histograms of the duration  $T$ (s) of light curves of sporadic meteors and some meteor showers observed in 2014 (a) and 2015 (b, c, and d).

The observed distributions of the duration of the BRAMON meteors are positively skewed (Figure 2), with skewness and kurtosis varying between 13.725 – 17.218 (ETA) to 0.8301 – 0.529 (SIA) or 0.5393 – 0.4112 (SDA) for meteor showers observed in 2015, implied in asymmetrical to

potential symmetrical distributions. The sporadic meteors have a duration distribution with skewness and kurtosis equal to 48.169 and 326.537 respectively in the same observational season. The high kurtosis value suggests that the duration distributions of the SPO are heavily tailed or have a profusion of outliers. We have identified these outliers using the Tukey’s Fences method ( $k = 1.5$ ), corresponding to a light curve duration  $\geq 0.8$  s and  $\approx 7\%$  of the sample. The median of SPO meteors’ outliers beginning and ending heights variation  $\Delta H (= H_b - H_e)$  are twice the value of the rest of the sample (23 versus 10 km in 2014, and 20 versus 10 km in 2015) (Figure 3), associated with a reduction of the geocentric velocity (38 versus 14 km/s in 2014, and 51 versus 21 km/s in 2015). These meteors have a long atmospheric path and low velocity, justifying a longer light curve duration. We were not able to define the same statement for the meteor shower’s outliers between the analyzed meteor showers due to the small number of meteors in the same duration range.

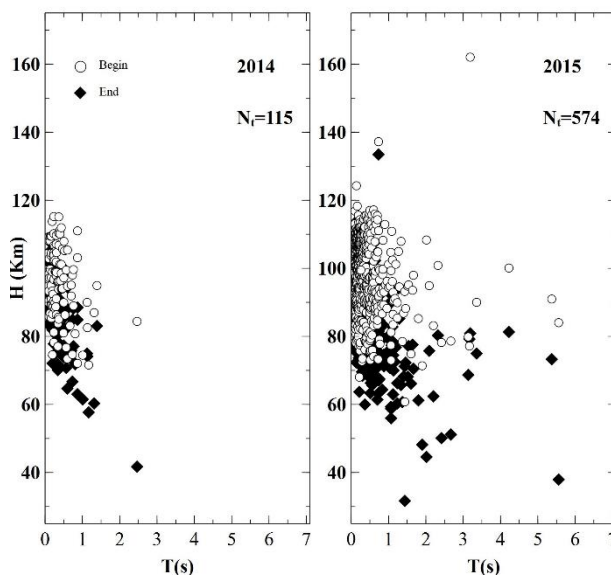


Figure 3 – Relationship between the SPO’s meteors visible light curve duration  $T$ (s) and beginning and ending heights  $H$  (km) observed by BRAMON in 2014 and 2015 respectively.

Table 1 – Number of meteors  $N$  and median geocentric velocities  $v_g$  (km/s), beginning and ending height  $H_b$  and  $H_e$  (km), radiant zenith distance  $Z$  (degrees) and duration  $T$ (s) for the SDA meteor shower observed by BRAMON in 2014.

$N$	$v_g$	$H_b$	$H_e$	$Z$	$T$
24	36.0	92.8	85.7	23.6	0.20

We sort the meteor shower geocentric velocities on ascending order in Table 2 to define the pairs compared with the  $t$ -test. The  $t$ -test suggests a similarity between the distributions of the duration of the light curves for the SDA meteor shower observed in 2014 and 2015, with a  $p$ -values = 0.078. This condition is valid for SPO meteors observed in the same period ( $p$ -value = 0.35). The comparison between the distributions of the pairs GEM – SDA, SDA – SIA and PER – ETA in 2015 have shown a dissimilarity between them (Table 3). The pair CAP – GEM is similar with  $p$ -value = 0.12.

Table 2 – Number of meteors  $N$  and median geocentric velocities  $v_g$  (km/s), beginning and ending height  $H_b$  and  $H_e$  (km), radiant zenith distance  $Z$  (degrees) and duration  $T$ (s) for the meteor showers observed by BRAMON in 2015.

Name	$N$	$v_g$	$H_b$	$H_e$	$Z$	$T$
CAP	29	22.3	89.3	78.5	27.8	0.50
GEM	19	33.8	94.7	81.4	45.8	0.63
SDA	55	38.6	91.8	84.7	26.5	0.22
SIA	30	39.8	90.6	90.6	27.4	0.16
PER	15	59.6	113.0	98.9	80.5	1.18
ETA	20	64.5	108.8	96.9	47.0	0.26

Table 3 – Meteor shower pairs and corresponding  $p$ -values obtained from  $t$ -test using 2015 data.

Pair	$p$ -value
CAP – GEM	$1.2 \times 10^{-1}$
GEM – SDA	$4.0 \times 10^{-4}$
SDA – SIA	$< 7.0 \times 10^{-2}$
PER – ETA	$< 1.0 \times 10^{-4}$

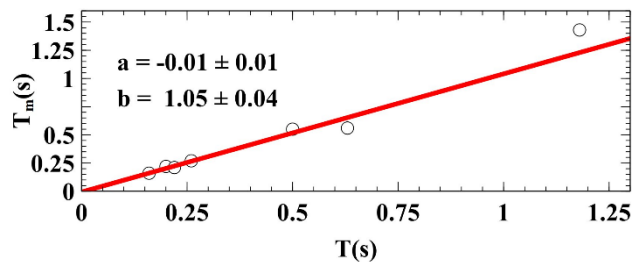


Figure 4 – Relationship between the median visible light curve duration  $T$ (s) and the ratio  $T_m (= \Delta H/v_g \cos(Z))$  (s) of the meteor showers listed in the Tables 1 and 2. The best linear fit with linear  $a$  and angular  $b$  coefficients is represented by the solid red line.

The meteor shower SDA has approximately the same median geocentric velocity  $v_g$ , zenith distance  $Z$ , and height variation  $\Delta H$  in 2014 and 2015 (Tables 1 and 2), which could explain its similarity. There are significant differences between some of these parameters for pairs of meteor showers with  $p$ -value  $\leq 0.05$ , and even between statistically similar showers as the pair CAP – GEM.

There is no distinction between the meteoroids analyzed in this study from a mineralogical point of view. Sekiguchi (2020) classified 1596 meteor spectra using the scheme by Borovička et al. (2005). The analyzed meteors are in the absolute magnitude range from  $-8$  to  $+2.6$ , similar to our sample. The showers ETA, GEM, PER, and SDA showed predominantly meteoroids with N3 type spectra (enhanced Na and Fe poor). The dissimilarity between the pairs PER – ETA, SDA–SIA and GEM – SDA in Table 3 could not be explained by mineralogical difference between the meteors from various meteor showers.

We calculated the ratio  $T_m$  between the height variation  $\Delta H$  and the zenith component of the meteor's geocentric velocity  $v_g \cos(Z)$ . The classic model of the ablation of meteors suggests that the duration depends on the initial

mass, the density, height, speed of the meteor and the zenith distance (its  $\cos(Z)$ ) (Hawkes and Jones, 1975). We found that the ratio  $T_m$  is approximately equal to the duration  $T$  (Figure 4).

The largest difference  $D$  between  $T_m$  and  $T$  is associated with the PER meteor shower ( $D = -0.25$  s), as opposed to what was observed in the CAP, GEM, SDA, SIA and ETA meteoroid streams ( $-0.05 \leq D \leq 0.07$  s). The difference  $D$  between  $T$  and  $T_m$  could be explained by the deceleration suffered by the meteoroid on its entry into the Earth's atmosphere. The previous measurements are approximately within the uncertainty of the measurement of time in our observations (0.07 s). Then, given the uncertainty of duration, it is not possible to detect the effect of the deceleration in the light curve duration amongst the analyzed meteor showers.

The zenith component of the geocentric velocity in the definition of duration  $T$  may be responsible for the similarity or dissimilarity between the pairs defined in Table 3.

The zenith distance of a meteor's radiant depends on the geographic location of the observer, so it is not recommended to compare the distribution of the duration of meteor light curves obtained from different observational sites.

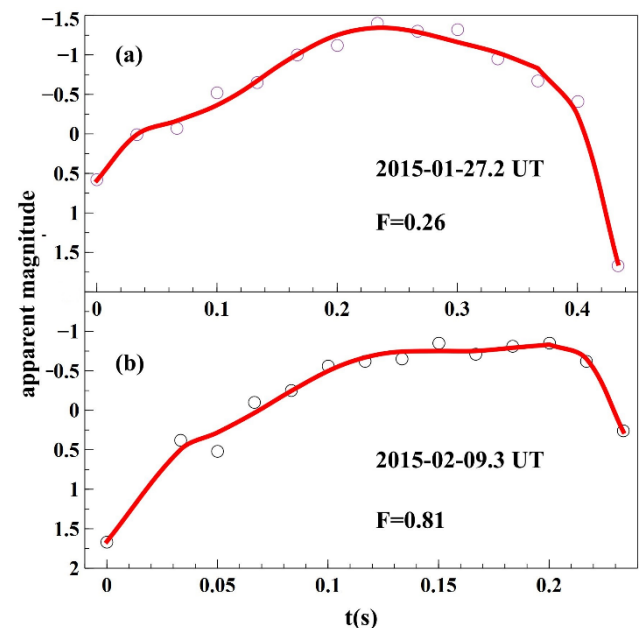


Figure 5 – Light curves from sporadic early (a) and late-type (b) meteors were observed in João Pessoa (northeast of Brazil) in the first quarter of 2015. The solid red curve corresponds to a sixth-degree polynomial.

### 3.2 Symmetry of meteor light curves

The classical model for the ablation of a dust ball meteor suggests an asymmetrical magnitude distribution around the brightness peak. However, the light curve can be late or early peaked due to variation in the atmospheric density and meteoroid composition, size, bulk density, or compressive strength (Figure 5). The light curve symmetry or skewness parameter  $F$ , defined as the ratio between the time intervals

for a meteor magnitude rise and drop of 1 magnitude relative to the light curve peak (Brosch et al., 2004):

$$F = \frac{t_{B1} - t_M}{t_{B1} - t_{E1}} \quad (1)$$

with  $t_{B1}$  and  $t_{E1}$  the time when the meteor brightness is 1 magnitude fainter than the peak ( $t_{B1} < t_{E1}$ ), and  $t_M$  is the time of the peak brightness.

Table 4°– Number of meteors  $N$ , parent body or meteor shower complex, and median  $F$  parameters for SPO meteors observed in 2014 and 2015, and seven meteor showers observed in 2015.

Name	$N$	Parent Body/Complex	$F$
NIA	32	x/298/IAQ	0.52
SDA	85	P/2008 Y12 (SOHO)/297/DAQ	0.52
PER	81	109P/Swift-Tuttle/x	0.54
SPO 2014	751	x/x	0.55
SPO 2015	787	x/x	0.57
ETA	39	1P/Halley/x	0.58
SIA	43	x/298/IAQ	0.61
CAP	59	169P/NEAT/x	0.62
ERI	42	C/1852 K1 (Chacornac)?/x	0.69

Table 5°– Meteor shower pairs and corresponding  $p$ -values obtained with t-test using 2015 data.

Pair	$p$ -value
SIA – SDA	$2.0 \times 10^{-4}$
SIA – NIA	$3.2 \times 10^{-3}$
PER – ERI	$4.2 \times 10^{-2}$
SDA – PER	$2.0 \times 10^{-1}$
ERI – ETA	$4.3 \times 10^{-1}$
CAP – SIA	$7.9 \times 10^{-2}$
ETA – PER	$2.1 \times 10^{-1}$
NIA – SDA	$7.3 \times 10^{-1}$

The times  $t_{B1}$ ,  $t_{E1}$ , and  $t_M$  of Equation (1) were estimated with the sixth-degree polynomial adjustment of the meteor light curves. This degree of the polynomial was arbitrated for providing a high quadratic correlation factor ( $R^2 \geq 0.95$ ) for curves with an approximately convex shape (Beech, 2007). The morphological classification applied in this study is based on the  $F$  value:  $F = 0.5$  corresponds to a symmetrical light curve as predicted by the classic model,  $F < 0.5$  is an early one, and  $F > 0.5$  a late skewed curve.

We analyzed the distribution of 4725 measures of parameter  $F$  corresponding to light curves and duration equal to or higher than 0.3 s. The choice of this minimum duration implied light curves with at least 10 data points considering an interval of  $\approx 0.033$  s between each frame. The meteors were observed at a single station, justifying the difference

between the number of meteors in the same meteor shower or sporadic meteors analyzed in Section (3.1). There were no meteors with sufficiently high angular velocity in our data set to generate trails that would make it impossible to determine the points that made up the light curves. The analyzed dataset has SPO meteors observed in 2014 and 2015 and the CAP, ERI, ETA, NIA (Northern Iota Aquariids), PER, SDA, and SIA meteors observed in 2015. About 5% of this sample is made up of meteor light curves with  $F < 0.2$  and 16% with  $F > 0.8$ .

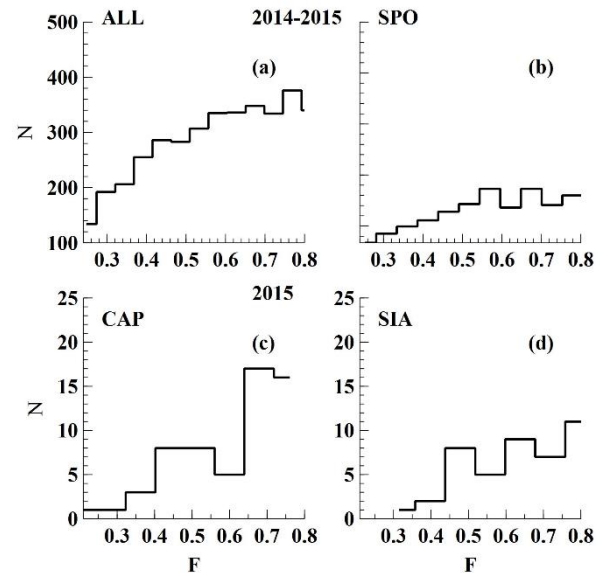


Figure 6°– Histograms of the  $F$  parameter distributions of the light curves of all meteors and SPO meteors observed in 2014 and 2015 (a and b), and for CAP and SIA meteor showers in 2015 (c and d).

Koten et al. (2004) did not identify light curves with  $F < 0.2$  and about 2% of a total of 170 PER meteors had light curves with  $F > 0.8$ . Our data do not allow us to refute these ideas. The BRAMON's light curves with  $F > 0.8$ , appear to be double-peaked (Kozak, 2018) or probably present flickering phenomena (Opik, 1936; Beech and Brown, 2000). This implied quadratic correlation coefficients  $R^2 \leq 0.90$  with the used polynomial. We do not consider these  $F$  parameter estimates to be reliable. Light curves with  $0.2 \leq F \leq 0.8$  have an approximately convex shape (Figure 5). As a result, we analyzed light curves with  $0.2 \leq F \leq 0.8$ , which reduced our sample to 3732 measurements. This amount implied that 79% of BRAMON meteors had approximately convex light curves, which is a reasonable value when compared to the 67% percentage of single-peak light curves found by Subasinghe et al. (2016). The residual distribution is asymmetrical, with left/negative skew, long left tale (skewness =  $-0.23$ ), and platykurtic (kurtosis =  $-1.0$ ), and presents short thin tails (Figure 6). The median  $F$  parameter of the meteor showers and SPO meteors vary between 0.5 and 0.7 (Table 4).

The  $F$  parameters of the CAP, ETA, SDA, SIA, and PER meteors do not appear to have any correlation with the geocentric velocity or its zenith component, altitude variation, or light curve duration comparing the data from

Table 4 to 1 and 2. The  $t$ -test indicates that the meteor shower  $F$  parameter distributions also are independent of the dynamic association (Tables 4 and 5).

The distributions of the  $F$  parameter of the SPO meteors vary between 0.5 and 0.7 (Table 4). The distributions of the  $F$  parameter of the SPO meteors shows temporal variation ( $p$ -value =  $1.8 \times 10^{-2}$ ) between 2014 and 2015. The  $F$  parameter distributions of meteor showers SDA, SIA, and NIA are not similar to SPO meteors in the 2015 observational season (Table 6).

Table 6 – Meteor shower pairs and corresponding  $p$ -values obtained with  $t$ -test using 2015 data.

Pair	$p$ -value
SPO – SDA	$5.5 \times 10^{-3}$
SPO – ERI	$6.2 \times 10^{-2}$
SPO – NIA	$3.8 \times 10^{-2}$
SPO – SIA	$4.2 \times 10^{-2}$
SPO – PER	$2.9 \times 10^{-1}$
SPO – ETA	$4.4 \times 10^{-1}$
SPO – CAP	$6.4 \times 10^{-1}$

Koten et al. (2004) postulates that the average  $F$  parameter is inversely proportional to the strength of the material that makes up the meteoroids. The strength of the meteoroid material can be inferred indirectly through the PE criterion (Ceplecha and McCrosky, 1976). Fireballs can be separated into four classes (I, II, IIIA, and IIIB), according to the PE value. Brown et al. (2013) defined mean PE values for the Taurids ( $-5.39 \pm 0.34$ ), PER ( $-5.52 \pm 0.24$ ) and GEM ( $-4.5 \pm 0.3$ ) observed by the MORP network. The PER and Taurids fireballs are more often of type IIIa (short period cometary), whereas the GEM meteoroids are of type I (ordinary chondrite-like). GEM meteoroids would be less fragile than PER. Thus, we could conclude that the pairs defined in Tables 5 and 6 with  $p$ -value  $\geq 0.05$  would have similar strength levels. However, the PER meteors may present late-peaked light curves for meteoroids of greater mass ( $> 10^{-5}$  kg) (Campbell-Brown, 2019).

The median  $F$  parameter of all meteor light curves observed by BRAMON in 2014 and 2015 is 0.56, which suggests that light curves are, in general, late peaked for meteors with a duration greater than or equal to 0.3 s.

## 4 Conclusions

We analyzed a homogeneous set of photometric and dynamic meteor data obtained by BRAMON between 2014 and 2015. Our main results are:

Light curves of SPO meteors with  $T \geq 0.80$  s are classified as outliers, corresponding to 8% of the total number of meteors observed in 2014 and 2015. These outlier meteors have  $\Delta H$  height variations and the geocentric speeds are twice and half of the rest of the sample respectively justifying their longer duration.

The distributions of the duration  $T$  of the luminous phase of the meteors of the SDA showers and the SPO meteors do not present variation between 2014 and 2015. There is a similarity between the distributions of duration between the meteor shower pairs CAP – GEM and SDA – SIA in the 2015 observational season.

The ratio between height variation  $\Delta H$  and the zenith component of geocentric meteor velocity  $v_g \cos(Z_i)$  is approximately equal to the duration  $T$  of a meteor light curve.

The zenith distance of a meteor’s radiant depends on the geographic location of the observer, so it is not recommended to compare the distribution of the duration of meteor light curves obtained from different observing sites.

The distributions of the symmetry parameter  $F$  of the meteors’ light curves of SPO meteors are dissimilar in 2014 and 2015. The opposite condition was observed in 2015 between the meteor shower pairs SDA – PER, ERI – ETA, CAP – SIA, ETA – PER, and NIA – SDA. The similarity between these meteor showers suggests independence of the  $F$  parameters with the light curve duration, cinematic parameters, or parent body/meteor shower complex.

The median value of the symmetry parameter  $F$  of the light curves registered in 2015, with a duration greater than or equal to 0.3 s and  $0.2 \leq F \leq 0.8$ , is 0.56, indicating that the meteor light curves are late-peaked

## Acknowledgment

The author thanks C. A. di Pietro and M. Zurita for kindly providing the BRAMON data.

## References

- Beech M. (2007). “The classification of meteor light curves: an application of hat theory”. *Monthly Notices of the Royal Astronomical Society*, **380**, 1649–1655.
- Beech M. and Brown P. (2000). “Fireball flickering: the case for indirect measurement of meteoroid rotation rates”. *Planetary and Space Science*, **48**, 925–932.
- Bland P. A. (2004). “Fireball cameras: The Desert Fireball Network”. *Astronomy and Geophysics*, **45**, 5.20–5.23.
- Borovička J., Koten P., Spurný P., Boček J., and Štork R. (2005). “A survey of meteor spectra and orbits: evidence for three populations of Na-free meteoroids”. *Icarus*, **174**, 15–30.
- Brosch N., Helled R., Polishook D., Almozino E., and David N. (2004). “Meteor light curves: the relevant parameters”. *Monthly Notices of the Royal Astronomical Society*, **355**, 111–119.
- Brown P., Marchenko V., Moser D. E., Weryk R., and Cooke W. (2013). “Meteorites from meteor

- showers: A case study of the Taurids”. *Meteoritics and Planetary Science*, **48**, 270–288.
- Campbell-Brown, M. D. (2019). “Meteoroid structure and fragmentation”. *Planetary and Space Science*, **169**, 1–7.
- Cepplecha Z. and McCrosky R. E. (1976). “Fireball end heights: A diagnostic for the structure of meteoric material”. *Journal of Geophysical Research*, **81**, 6257–6275.
- Hajduková M. J., Koten P., Kornoš L., and Tóth J. (2017). “Meteoroid orbits from video meteors. The case of the Geminid stream”. *Planetary and Space Science*, **143**, 89–98.
- Hawkes R. L. and Jones J. (1975). “A quantitative model for the ablation of dustball meteors”. *Monthly Notices of the Royal Astronomical Society*, **173**, 339–356.
- Kornos L., Koukal J., Piffel R., and Toth J. (2013). “Database of meteoroid orbits from several European video networks”. In, Gyssens M. and Roggemans P., editors, *Proceedings of the International Meteor Conference*, La Palma, Canary Islands, Spain, 2012. IMO, pages 21–25.
- Kornoš L., Matlovič P., Rudawska R., Tóth J., Hajduková M. J., Koukal J., and Piffel R. (2014). “Confirmation and characterization of IAU temporary meteor showers in EDMOND database”. In, Jopek T. J., Rietmeijer F. J. M., Watanabe J., and Williams I. P., editors, *Meteoroids 2013*, pages 225–233.
- Koten P., Borovička J., Spurný P., Betlem H., and Evans S. (2004). “Atmospheric trajectories and light curves of shower meteors”. *Astronomy & Astrophysics*, **428**, 683–690.
- Kozak P. (2018). “Meteors with multi-modal light curves: observations and qualitative models”. *Bulletin of Taras Shevchenko National University of Kyiv Astronomy*, **58**, 48–55.
- McCrosky R. E. and Boeschenstein H. J. (1965). “The Prairie Meteorite Network”. *SAO Special Report*, **173**.
- Opik E. (1936). “Researches on the physical theory of meteor phenomena. i. theory of the formation of meteor craters”. *Publications of the Tartu Astrofizica Observatory*, **28**, 1–12.
- Sekiguchi T. (2020). “Results of spectral observations of meteor showers and sporadic meteors from October 2018 until May 2020”. *eMetN*, **5**, 300–313.
- Southworth R. B. and Hawkins G. S. (1963). “Statistics of meteor streams”. *Smithsonian Contributions to Astrophysics*, **7**, 261–285.
- Subasinghe D., Campbell-Brown M. D., and Stokan E. (2016). “Physical characteristics of faint meteors by light curve and high-resolution observations, and the implications for parent bodies”. *Monthly Notices of the Royal Astronomical Society*, **457**, 1289–1298.
- Vereš P. and Toth J. (2010). “Analysis of the SonotaCo video meteoroid orbits”. *WGN, Journal of the International Meteor Organization*, **38**, 54–57.

# Discovery of a shower associated with comet 197P/LINEAR in UKMON Meteor Orbit Data

John Greaves

midmet@mail.com

Examination of archived meteor orbits from the UKMON multi-station meteor survey in comparison to known cometary orbits via  $D_J$  criterion selection revealed meteor streaming associated with the Jupiter Family Comet 197P/LINEAR. Extension to other multi-station meteor surveys led to a significant increase of candidate meteors helping to confirm matters. The recent evolution of the cometary orbit suggests that this shower is not only new but may increase in activity in the years to come, with the possibility of the May iota Draconids being an early expression outlier of this stream also being discussed.

## 1 Methodology

Archival data from the UKMON meteor survey (e.g., Campbell-Burns and Kacerek, 2014) were obtained from the UKMON online public data archive<sup>2</sup> with the orbital part of the data being analyzed utilizing the Jopek (1993)  $D$  criterion modification, henceforth referred to as  $D_J$ . One analysis took the form of assessing the UKMON orbits against those of comets using a  $D_J$  upper threshold limit of 0.10.

After a reasonable match of ten meteor orbits were found against the Jupiter Family Comet 197P/LINEAR<sup>3</sup> a wider  $D_J$  test was made using data from multi-station meteor survey publicly available data archives of SonotaCo Network (e.g., SonotaCo, 2009), CAMS (e.g., Jenniskens et al., 2018), EDMOND (e.g., Kornoš et al., 2014) and Global Meteor Network (Vida et al., 2019a; 2019b). As various regional meteor surveys can not only provide their own dataset but contribute it to other surveys the combined datasets used in this search had the potential for some duplicates, accordingly the results were sorted on Right Ascension and any objects in the resultant output having a commonality of Right Ascension, Declination and Solar Longitude had one of the duplicates removed (this led to the removal of three orbits). The various surveys have differing end dates for their public data releases, in the case presented here only GMN, SonotaCo and UKMON has so far provided data covering up until the end of 2021.

This resulted in a total of 161 meteor orbits meeting the  $D_J < 0.100$  threshold for the 197P/LINEAR orbit used, of which 72 have  $D_J < 0.008$  and 20 have  $D_J < 0.006$ .

As all the surveys have at least some regional aspects in global terms, with only some being truly global, leading to concomitant caveats with respect to nightly coverage due to local weather, as well as the dramatic increase in the number of cameras and sites used in most if not all surveys in very recent times, no year-by-year count of meteors is presented.

As survey temporal and spatial coverage increases and becomes more complete such comparisons may well be informative due to the evolution of this comet's orbit, as outlined in the Discussion section.

## 2 Results

The ten UKMON discovery orbits are listed in *Table 1* below. Due to some surveys using similar software either currently and/or in the past there is a tendency for them to have similar if not identical styles for their identifiers. Where relevant in *Table 1* and also in the following *Table 2* SonotaCo identifiers appear as is, the very similar EDMOND identifiers are preceded by the two-letter prefix 'ED' and the equally similar UKMON identifiers are preceded by the two-letter prefix 'UK' in order to clarify the provenance of the orbits. At the time the data were procured GMN did not use a unique identifier and as such those orbits had a built-in running number identifier appended to them on import into a master orbits database created for analyses such as this. This running number is in no way official.

## 3 Discussion

### 197P/LINEAR and its orbit

The original analysis used cometary orbits as a seed to check for potential comet–shower associations within UKMON orbit data, with 197P/LINEAR alone arising as a previously unknown candidate. Whilst examining the data at the Minor Planet Center for this small and faint object it was noted that there were several different orbits provided since 2003 effectively representing the comet's perihelion return nearly every five years. Although somewhat inclined in its orbit the comet does nevertheless approach the orbit of Jupiter to within one Astronomical Unit (1 AU) at aphelion, having a Jupiter Family Comet Tisserand like value ( $T_J$ ) of around 2.9.

<sup>2</sup> <https://archive.ukmeteornetwork.co.uk/>

<sup>3</sup> [https://minorplanetcenter.net/db\\_search/show\\_object?object\\_id=197P](https://minorplanetcenter.net/db_search/show_object?object_id=197P)

Table 1 – The identifier,  $D_J$  criterion value relative to 197P for the UKMON orbits, radiant position as Right Ascension and declination in degrees, solar longitude  $\lambda_\odot$  in degrees, geocentric velocity  $v_g$  in km/s, perihelion distance  $q$  in Astronomical Units, eccentricity  $e$ , inclination  $i$  in degrees, argument of perihelion  $\omega$  in degrees and ascending node  $\Omega$  in degrees are given for each associated meteor orbit followed by their mean and median value along with the standard deviation and finally the orbital details for 197P used in the test.

$ID$	$D_J$	R.A.	Dec.	$\lambda_\odot$	$v_g$	$q$	$e$	$i$	$\omega$	$\Omega$
UK20200526_003101	0.088	235.4	53.7	64.962	16.3	0.9984	0.5873	24.15	196.1	64.97
UK20210530_235903	0.092	238.0	57.8	69.487	16.2	1.0082	0.5575	24.91	190.09	69.5
UK20200531_000246	0.054	240.0	60.2	69.741	17.8	1.0107	0.6135	27.39	187.42	69.75
UK20210531_235736	0.072	232.3	56.3	70.444	16.5	1.008	0.6376	24.13	189.97	70.46
UK20190601_235642	0.082	225.9	62.5	70.940	15.2	1.0141	0.6094	22.3	180.97	70.94
UK20210601_234528	0.077	223.1	60.5	71.394	15.4	1.0138	0.6446	22.13	182.38	71.41
UK20180604_001155	0.081	240.0	59.0	73.105	17.4	1.0108	0.6284	26.37	187.81	73.11
UK20210605_002040	0.092	240.2	59.3	74.291	17.7	1.0116	0.628	26.91	187.15	74.3
UK20210606_225702	0.098	241.6	64.6	76.150	18.3	1.0149	0.6088	28.51	180.47	76.16
Mean orbit		235.1	59.1	66.872	16.9	1.007	0.619	25.2	188.6	66.9
Median orbit		236.7	59.3	67.007	16.9	1.008	0.618	25.3	189.1	67
Stand. Dev.		6.3	4.2	5.333	1.1	0.007	0.034	2.1	5.9	5.3
197P/LINEAR						1.0599	0.6301	25.557	188.68	66.39

Table 2 – The identifier,  $D_J$  criterion value relative to 197P for all orbits, radiant position as Right Ascension and declination in degrees, solar longitude  $\lambda_\odot$  in degrees, geocentric velocity  $v_g$  in km/s, perihelion distance  $q$  in Astronomical Units, eccentricity  $e$ , inclination  $i$  in degrees, argument of perihelion  $\omega$  in degrees and ascending node  $\Omega$  in degrees are given for each associated meteor orbit followed by their mean and median value along with the standard deviation, as well as the minimum and maximum value for all orbits and finally the orbital details for 197P used in the test. The GMN running number is not official, SonotaCo orbits have no prefix, an ‘ED’ or ‘UK’ prefix denotes an EDMOND or UKMON orbit respectively.

$ID$	$D_J$	R.A.	Dec.	$\lambda_\odot$	$v_g$	$q$	$e$	$i$	$\omega$	$\Omega$
ED20080523_224334	0.079	229.6	60.2	63.038	15.9	1.0101	0.5992	23.61	186.65	63.04
20090527_022105	0.092	234.9	52.4	65.459	15.9	0.9989	0.6431	22.38	195.43	65.46
ED20100524_220014	0.064	239.9	59.5	63.479	18.2	1.0075	0.6060	28.09	189.48	63.48
20100602_235220	0.058	234.0	62.4	71.825	16.9	1.0141	0.6482	25.16	181.14	71.83
ED060506MLA0027	0.083	241.7	65.3	75.116	16.5	1.0147	0.5848	25.39	179.77	75.12
ED20110522_222928	0.081	240.4	60.2	61.330	18.0	1.0076	0.6028	27.87	189.02	61.33
ED052425ZGR0004	0.095	243.0	60.7	63.173	19.1	1.0084	0.6021	30.00	188.58	63.17
CAMS8363	0.088	239.7	55.7	65.627	18.8	0.9996	0.6579	28.19	194.91	65.63
ED20110529_231653	0.094	228.1	55.0	68.085	16.4	1.0074	0.6998	22.93	189.94	68.09
ED20110603_003805	0.089	245.2	66.9	71.975	17.7	1.0142	0.5891	27.73	179.00	71.98
CAMS8414	0.082	224.6	59.9	72.315	15.2	1.0132	0.6008	22.22	184.40	72.32
ED20110604_015304	0.095	235.5	64.0	72.983	17.6	1.0143	0.7063	25.56	181.49	72.98
CAMS60415	0.094	231.8	52.6	58.610	16.4	0.9910	0.5817	24.07	199.26	58.61
CAMS60635	0.059	235.4	57.6	60.371	17.8	1.0014	0.6246	26.72	193.51	60.37
CAMS60798	0.051	234.4	57.4	61.539	17.2	1.0023	0.6083	25.84	193.22	61.54
CAMS60858	0.064	225.8	54.9	62.327	15.9	1.0021	0.6305	22.76	193.29	62.33
CAMS60876	0.077	239.2	55.3	62.371	17.8	0.9968	0.5957	27.10	196.63	62.37
CAMS61249	0.084	219.9	63.0	67.254	15.7	1.0132	0.6442	22.78	182.25	67.26
CAMS61346	0.077	225.8	63.2	68.165	15.5	1.0132	0.5885	23.27	182.91	68.17
ED20120529_215237	0.079	232.7	64.7	68.740	16.6	1.0137	0.5921	25.47	180.64	68.74

<i>ID</i>	<i>D<sub>J</sub></i>	<i>R.A.</i>	<i>Dec.</i>	$\lambda_{\odot}$	$v_g$	<i>q</i>	<i>e</i>	<i>i</i>	$\omega$	$\Omega$
CAMS61674	0.058	235.6	62.2	70.119	16.8	1.0124	0.5856	25.75	185.29	70.12
CAMS62019	0.096	242.8	59.6	72.071	17.9	1.0094	0.5896	27.79	189.23	72.07
CAMS62848	0.097	230.3	64.1	78.650	16.8	1.0152	0.6267	25.28	179.59	78.65
CAMS116414	0.096	231.1	54.2	56.353	18.2	0.9916	0.6749	26.26	197.91	56.35
CAMS116669	0.092	234.3	52.2	57.486	17.4	0.9866	0.6036	25.73	200.85	57.48
CAMS116917	0.088	233.2	52.1	59.254	17.0	0.9890	0.6001	24.89	200.00	59.25
ED20130520_212457	0.082	232.1	59.7	59.826	17.1	1.0070	0.6181	25.80	189.24	59.83
20130521_205020	0.082	228.4	59.3	60.404	17.3	1.0080	0.6323	26.03	188.38	60.40
CAMS117442	0.053	230.8	57.4	63.078	16.3	1.0046	0.5995	24.26	191.85	63.07
CAMS117654	0.061	238.7	56.8	64.161	17.7	1.0016	0.6025	27.01	193.99	64.16
CAMS117745	0.064	223.2	59.5	65.970	16.2	1.0104	0.6652	23.28	186.74	65.96
CAMS117828	0.044	226.9	60.1	67.869	16.6	1.0111	0.6548	24.18	186.37	67.86
CAMS118015	0.086	227.8	54.6	69.021	15.6	1.0059	0.6166	22.43	191.54	69.02
CAMS118106	0.089	234.1	56.8	69.795	16.0	1.0070	0.5774	24.10	191.06	69.79
CAMS118212	0.085	223.9	56.4	69.947	16.1	1.0096	0.6804	22.71	188.28	69.94
20130531_214206	0.079	236.9	56.1	70.037	16.9	1.0078	0.5852	25.76	190.40	70.04
20130603_211321	0.072	231.4	57.0	72.893	16.7	1.0116	0.6386	24.76	186.84	72.89
CAMS118604	0.078	221.4	64.5	73.783	16.1	1.0145	0.6462	23.50	178.82	73.78
CAMS118684	0.098	227.4	63.2	74.670	15.3	1.0146	0.5688	23.10	181.02	74.67
CAMS187483	0.094	233.0	51.2	57.086	17.5	0.9840	0.6192	25.48	201.71	57.08
20140520_004224	0.089	237.3	57.7	58.388	16.9	1.0037	0.5901	25.51	191.85	58.39
CAMS366248	0.075	235.9	54.9	58.673	18.1	0.9940	0.6304	27.07	197.34	58.67
20140522_000305	0.066	235.8	55.1	60.286	16.7	1.0010	0.5928	24.94	193.95	60.29
CAMS188569	0.074	238.7	59.3	63.984	17.1	1.0062	0.5649	26.43	190.99	63.98
CAMS188636	0.056	230.0	60.6	64.719	16.2	1.0097	0.5972	24.26	187.56	64.72
CAMS188673	0.073	222.1	57.8	64.784	15.3	1.0088	0.6246	21.85	188.48	64.78
ED20140526_221937	0.082	225.3	62.7	65.384	15.6	1.0121	0.5963	23.24	184.21	65.38
ED20140526_231411	0.090	239.9	63.1	65.420	17.1	1.0112	0.5543	26.79	185.97	65.42
CAMS188822	0.090	227.5	55.3	65.623	15.1	1.0049	0.5782	22.03	192.14	65.62
ED20140528_003629	0.087	220.8	55.1	66.436	14.9	1.0076	0.6328	20.87	189.83	66.44
CAMS189072	0.099	235.0	55.3	66.633	16.0	1.0024	0.5602	24.11	194.09	66.63
CAMS189244	0.076	230.0	55.5	66.869	15.7	1.0048	0.5933	23.07	192.24	66.87
ED20140529_020818	0.073	243.2	59.2	67.457	18.6	1.0067	0.6115	28.79	190.80	67.46
CAMS189291	0.088	234.3	55.0	67.616	17.8	1.0021	0.6765	26.01	193.58	67.61
CAMS189423	0.054	227.0	57.1	67.820	16.0	1.0083	0.6373	23.19	189.34	67.82
CAMS189467	0.100	239.4	55.6	68.526	18.5	1.0016	0.6585	27.66	194.09	68.52
CAMS189531	0.074	224.7	61.0	68.680	15.2	1.0125	0.5921	22.49	184.72	68.68
CAMS189540	0.047	226.5	60.1	68.693	16.4	1.0115	0.6533	23.97	186.00	68.69
CAMS366360	0.079	243.1	60.5	69.302	17.9	1.0095	0.5806	28.03	188.77	69.30
ED20140531_035320	0.066	229.6	58.2	69.446	15.8	1.0097	0.5985	23.38	188.51	69.45
CAMS189805	0.089	221.5	65.8	70.432	15.7	1.0139	0.6135	23.23	178.72	70.43
CAMS190039	0.086	230.9	68.0	71.557	17.3	1.0138	0.6245	26.27	177.47	71.56
CAMS190065	0.058	230.3	60.5	71.596	17.1	1.0123	0.6621	25.20	185.54	71.60
CAMS190316	0.061	232.1	62.1	73.536	16.7	1.0137	0.6185	25.20	183.70	73.54
CAMS190680	0.097	238.8	61.1	75.484	17.7	1.0128	0.6243	27.12	185.65	75.49
CAMS190803	0.093	236.6	63.4	76.424	17.0	1.0146	0.5938	26.26	182.32	76.43
ED20140608_021817	0.100	239.5	64.8	77.045	17.6	1.0149	0.5960	27.45	181.00	77.05
CAMS190901	0.098	232.6	64.1	77.255	17.8	1.0150	0.6670	26.71	180.56	77.26

<i>ID</i>	<i>D<sub>J</sub></i>	<i>R.A.</i>	<i>Dec.</i>	$\lambda_{\odot}$	$v_g$	<i>q</i>	<i>e</i>	<i>i</i>	$\omega$	$\Omega$
CAMS378824	0.081	234.6	56.8	57.453	18.1	0.9978	0.6377	26.99	195.18	57.45
ED20150520_204748	0.095	234.6	60.6	59.311	17.5	1.0068	0.5953	26.88	189.46	59.31
20150523_022656	0.093	235.7	60.3	61.101	15.6	1.0085	0.5883	23.20	188.23	61.10
ED20150524_220102	0.064	237.3	60.8	63.207	18.2	1.0088	0.6332	27.69	188.07	63.21
CAMS261709	0.098	222.7	57.6	74.083	15.6	1.0128	0.6613	22.16	185.33	74.08
CAMS261763	0.091	239.6	60.8	74.232	17.5	1.0122	0.6017	26.95	186.41	74.23
ED20150605_211215	0.094	241.9	61.6	74.679	17.9	1.0137	0.5923	28.03	184.06	74.68
CAMS262192	0.097	232.2	65.0	78.121	16.7	1.0151	0.5979	25.46	179.08	78.12
CAMS444956	0.100	236.5	57.5	56.541	17.5	0.9984	0.5833	26.82	195.15	56.54
20160519_002758	0.079	233.3	54.3	57.888	16.5	0.9987	0.5999	24.49	194.99	57.89
ED20160523_232311	0.060	233.7	60.0	63.013	16.7	1.0087	0.5996	25.22	188.27	63.01
ED20160524_233547	0.093	233.8	54.2	63.982	15.4	1.0009	0.5720	22.66	194.67	63.98
CAMS445444	0.081	226.5	59.3	65.312	15.2	1.0096	0.5775	22.56	187.94	65.31
CAMS445465	0.064	232.6	56.2	65.407	16.3	1.0038	0.5902	24.22	192.76	65.41
CAMS322105	0.043	235.1	59.9	65.412	18.0	1.0081	0.6540	26.97	189.12	65.41
CAMS322112	0.057	226.0	55.9	65.445	16.0	1.0057	0.6394	22.92	191.13	65.45
20160603_005430	0.072	233.2	59.1	72.307	15.5	1.0131	0.6146	22.67	184.54	72.31
CAMS322828	0.098	241.1	67.9	72.897	18.7	1.0143	0.6306	29.12	178.28	72.89
CAMS322854	0.096	228.6	62.6	72.976	15.3	1.0141	0.5618	23.16	182.45	72.98
20160604_024948	0.093	247.7	59.9	73.342	18.3	1.0110	0.6460	27.87	187.65	73.34
CAMS322981	0.073	231.8	60.3	74.029	16.7	1.0130	0.6317	24.93	185.27	74.03
ED20160606_210930	0.090	232.3	65.8	76.347	16.6	1.0143	0.5962	25.46	176.79	76.35
20170520_224425	0.096	233.1	50.3	59.494	16.5	0.9893	0.5859	24.27	200.08	59.49
20170530_013215	0.097	251.3	61.3	68.255	18.0	1.0115	0.5564	28.72	186.28	68.26
20180522_021821	0.080	233.5	59.1	60.357	16.3	1.0067	0.6387	23.68	189.51	60.36
20180527_021646	0.046	237.4	60.7	65.160	16.9	1.0102	0.6466	25.04	186.86	65.16
20180530_215143	0.089	227.6	59.9	68.821	15.3	1.0130	0.5655	23.08	183.44	68.82
20180603_032144	0.098	243.6	57.5	71.915	16.3	1.0075	0.5968	24.30	190.79	71.91
20180603_035405	0.079	249.0	66.6	71.936	17.2	1.0142	0.5810	26.72	180.57	71.94
UK20180604_001155	0.081	240.0	59.0	73.105	17.4	1.0108	0.6284	26.37	187.81	73.11
GMN4598	0.078	226.0	52.9	62.527	16.5	0.9984	0.6683	23.11	195.20	62.54
GMN4620	0.086	221.7	59.8	62.626	15.4	1.0095	0.6200	22.29	187.28	62.64
GMN4697	0.071	231.4	53.5	64.358	16.5	0.9986	0.6196	24.01	195.63	64.36
UK20190601_235642	0.082	225.9	62.5	70.940	15.2	1.0141	0.6094	22.30	180.97	70.94
GMN5079	0.100	237.3	58.5	71.206	18.6	1.0087	0.6884	27.62	189.30	71.21
GMN5215	0.082	237.9	67.1	73.274	17.8	1.0144	0.6078	27.62	178.91	73.28
GMN79106	0.090	236.4	52.3	60.136	18.1	0.9882	0.6317	26.73	200.14	60.15
GMN79107	0.097	236.9	52.7	60.136	18.7	0.9887	0.6598	27.58	199.64	60.15
GMN79373	0.094	221.2	52.3	60.981	15.6	0.9990	0.6637	21.42	194.74	60.99
GMN79472	0.068	225.8	57.1	61.169	16.7	1.0043	0.6641	23.91	191.49	61.18
GMN79497	0.069	234.7	55.7	61.240	18.3	0.9983	0.6661	26.96	195.17	61.25
GMN79505	0.075	223.8	58.0	61.252	16.3	1.0062	0.6564	23.30	190.05	61.26
GMN79507	0.090	225.3	53.4	61.253	15.2	0.9993	0.5965	21.75	195.12	61.26
GMN79675	0.081	237.7	58.5	61.945	17.0	1.0040	0.5626	26.16	192.43	61.95
GMN79677	0.088	223.9	56.4	61.958	15.0	1.0050	0.5924	21.73	191.47	61.97
GMN79689	0.080	235.2	52.8	62.071	17.6	0.9924	0.6311	25.92	198.48	62.08
GMN79764	0.068	225.5	59.7	62.391	16.4	1.0084	0.6496	23.91	188.33	62.40
GMN79902	0.082	222.3	60.8	63.219	15.9	1.0105	0.6438	23.03	186.21	63.23

<i>ID</i>	<i>D<sub>J</sub></i>	<i>R.A.</i>	<i>Dec.</i>	$\lambda_{\odot}$	$v_g$	<i>q</i>	<i>e</i>	<i>i</i>	$\omega$	$\Omega$
GMN80106	0.076	229.3	53.5	64.300	17.0	0.9993	0.6707	24.21	194.92	64.31
UK20200526_003101	0.088	235.4	53.7	64.962	16.3	0.9984	0.5873	24.15	196.10	64.97
GMN80192	0.056	226.4	55.9	65.046	16.2	1.0052	0.6514	23.26	191.42	65.05
GMN80229	0.056	237.2	59.2	65.149	18.4	1.0065	0.6597	27.73	190.41	65.16
GMN80352	0.053	237.4	59.0	65.856	18.3	1.0066	0.6551	27.61	190.45	65.86
GMN80752	0.070	226.9	59.2	67.144	17.2	1.0099	0.6933	24.72	187.53	67.15
GMN80822	0.085	235.0	54.8	67.792	17.6	1.0015	0.6558	25.86	194.11	67.80
GMN80849	0.069	232.0	55.6	67.863	17.1	1.0044	0.6580	24.96	192.28	67.87
GMN80861	0.037	236.9	61.2	67.893	17.5	1.0105	0.6155	26.79	187.27	67.90
GMN80990	0.056	239.7	63.3	68.789	18.2	1.0123	0.6206	28.04	184.95	68.80
20200531_015313	0.074	239.6	60.3	69.455	15.7	1.0118	0.5721	23.71	186.10	69.45
UK20200531_000246	0.054	240.0	60.2	69.741	17.8	1.0107	0.6135	27.39	187.42	69.75
GMN81655	0.081	234.2	56.7	70.941	17.1	1.0071	0.6401	25.32	190.76	70.95
GMN 218148	0.079	225.0	57.2	59.711	15.9	1.0038	0.6183	22.99	191.82	59.72
GMN 218196	0.079	235.1	60.2	59.789	17.3	1.0056	0.5999	26.42	190.62	59.80
GMN 218476	0.065	235.6	54.8	61.085	17.8	0.9958	0.6306	26.53	196.69	61.09
GMN 218636	0.099	231.7	50.2	61.274	17.3	0.9870	0.6489	24.62	200.55	61.29
20210522_171348	0.081	235.6	52.8	61.539	17.7	0.9920	0.6232	26.08	198.84	61.54
GMN 218701	0.069	230.2	56.6	61.885	16.0	1.0028	0.5856	23.77	193.04	61.90
UK20210523_015210	0.075	233.9	57.0	61.885	15.9	1.0038	0.5791	23.62	192.43	61.90
GMN 218703	0.097	233.4	59.0	61.900	18.7	1.0050	0.7062	27.57	190.81	61.91
GMN 219470	0.070	231.3	64.9	66.765	17.2	1.0130	0.6319	26.03	182.41	66.77
GMN 219502	0.073	241.6	59.9	66.863	17.7	1.0079	0.5739	27.53	189.90	66.87
GMN 219858	0.082	236.9	62.7	68.462	16.5	1.0122	0.5550	25.68	185.25	68.47
GMN 220001	0.096	222.5	65.3	68.619	16.9	1.0137	0.6792	24.64	179.96	68.63
GMN 220284	0.069	234.1	58.1	69.487	16.3	1.0084	0.5885	24.66	189.73	69.50
UK20210530_235903	0.092	238.0	57.8	69.487	16.2	1.0082	0.5575	24.91	190.09	69.50
GMN 220318	0.094	216.9	60.9	69.516	14.7	1.0135	0.6172	20.96	182.47	69.53
GMN 220524	0.089	234.7	56.0	70.379	17.5	1.0057	0.6596	25.77	191.66	70.39
GMN 220543	0.077	242.4	64.7	70.400	18.2	1.0135	0.5960	28.51	182.91	70.41
GMN 220588	0.078	229.9	56.2	70.444	16.6	1.0077	0.6558	24.08	190.13	70.46
UK20210531_235736	0.072	232.3	56.3	70.444	16.5	1.0080	0.6376	24.13	189.97	70.46
GMN 220835	0.088	218.9	60.0	71.246	14.8	1.0136	0.6183	21.19	183.11	71.26
GMN 220861	0.100	239.4	68.4	71.326	18.4	1.0139	0.6261	28.62	177.79	71.33
GMN 220899	0.096	240.0	68.1	71.358	18.1	1.0140	0.6056	28.33	178.15	71.37
UK20210601_234528	0.077	223.1	60.5	71.394	15.4	1.0138	0.6446	22.13	182.38	71.41
GMN 220992	0.091	224.8	67.4	71.425	16.2	1.0137	0.6087	24.36	177.19	71.44
GMN 221122	0.084	239.0	58.8	71.627	17.2	1.0092	0.5932	26.39	189.33	71.64
GMN 221419	0.099	241.3	66.7	72.396	19.1	1.0143	0.6551	29.56	179.88	72.41
GMN 221517	0.074	239.5	62.5	73.192	18.1	1.0132	0.6292	27.81	184.66	73.20
GMN 221529	0.072	232.0	66.5	73.214	17.4	1.0144	0.6299	26.40	178.78	73.22
GMN 221564	0.090	223.9	58.1	73.261	15.2	1.0127	0.6208	21.92	185.50	73.27
UK20210605_002040	0.092	240.2	59.3	74.291	17.7	1.0116	0.6280	26.91	187.15	74.30
GMN 222340	0.096	241.0	65.3	76.150	18.3	1.0149	0.6174	28.43	180.76	76.16
UK20210606_225702	0.098	241.6	64.6	76.150	18.3	1.0149	0.6088	28.51	180.47	76.16

<i>ID</i>	<i>D<sub>J</sub></i>	R.A.	Dec.	$\lambda_{\odot}$	$v_g$	$q$	$e$	$i$	$\omega$	$\Omega$
<b>mean</b>		233.1	59.1	67.112	16.9	1.007	0.619	25.2	188.5	67.1
<b>median</b>		233.8	59.3	67.616	16.9	1.008	0.618	25.2	188.8	67.6
<b>stdev</b>		6.6	4.1	5.323	1.1	0.007	0.034	2.1	5.9	5.3
<b>min</b>		216.9	50.2	56.353	14.7	0.984	0.554	20.9	176.8	56.3
<b>max</b>		251.3	68.4	78.650	19.1	1.015	0.706	30.0	201.7	78.6
<b>197P</b>						1.060	0.6301	25.6	188.68	66.39
<b>MID</b>	0.078	230.8	252.5	60.200	16.7	0.989	0.604	24.3	198.1	60.2

Accordingly, the orbit used in this analysis was progressed backwards to earlier epochs and also to a lesser extent to future epochs via numerical integration. This revealed that prior to a less than 1 AU encounter with Jupiter itself in 1941 the comets perihelion distance,  $q$ , dropped below the roughly 1.2 AU previous average value and remained between roughly 1.12 and 1.17 until a nearly 0.5 AU encounter with Jupiter in 2001 which reduced  $q$  further to around 1.06 AU. In the formal elements provided by the Minor Planet Center (see footnote 2 in the Section Methodology) so called “non-gravitational” elements are also included (although not used in the less rigorous analysis of this study), such elements being due to other effects on a comet’s motion, usually outgassing.

Thus, from just after the turn of the Millennium until now this comet, which is likely outgassing dust and ices, has had a perihelion distance getting ever close to the mean orbit of the Earth. Indeed, this led to the recovery of the comet in 2003 where it was identified as a new asteroidal object 2003 KV2. It was recovered during its next apparition in 2008 as 2008 E2 and soon afterwards both its association with the earlier object and its cometary nature were realized. Following that there were returns in 2013 and 2018 with next perihelion being due in early December 2022. Throughout these apparitions the perihelion distance remained very near to 1.06 AU, although never getting much nearer to Earth than 0.3 AU throughout. In 2024, around the aphelion following on from the upcoming 2022 perihelion, the comet will again come within 1 AU of Jupiter after which the perihelion distance will increase to averaging around 1.1 AU and over. This small to and from drift in  $q$  following occasional aphelion interactions with Jupiter will carry on for the rest of the Century with even a limited potential of  $q$  dipping barely just below 1 AU in the next Century, however such forward extrapolations become less secure especially given the non-gravitational effects which can be quite variable in their vector during each perihelion.

Nevertheless, it can be seen that 197P became available in recent most times in order to produce a stream. It may have done so in the past, having danced with close approaches to Jupiter for long ages, but as it is a small and faint comet (rarely achieving much above magnitude 20 even when within 1 AU of Earth) and meteoroids from past to long past epochs may well have diffused out of the stream. Unfortunately, its new era of closer perihelion distances coincides with the evolution and growth of multi-station

video meteor surveys and accordingly it is likely impossible to disentangle the recent increase (especially in the 2020–2021 seasons) of this latest May to earliest June shower from the great increase of coverage and consequent data that have arrived in the past two or three years, even amongst the long established and previously relatively prolific monitoring groups.

However, as many of these surveys are now reaching optimal coverage to the point of near saturation such that differences due to year by year, and/or aphelion by aphelion orbit changes, along with the combination of the orbit drift and the non-gravitational forces as an indicator of material ejection, may well lead to enhanced periods of cometary activity in the last week in May and first week in June, centered around June 1<sup>st</sup>. The various surveys, which are more effective for brighter meteors, reveal a goodly proportion of fireballs for this shower, and although some detections were as faint as magnitude 4 the mean magnitude is around 0 with the brightest meteor being magnitude –5.

#### 4 Nomenclature of the shower

Finally, during the analysis the mean values of *Table 2* for Right Ascension and Declination and Solar Longitude were compared with those of extant showers. The shower May iota Draconids, henceforth MID (Šegon at al., 2015), was something of a distant possibility when only the UKMON data were used, its position and timing being markedly removed from said mean. However, when the analysis was extended to include more surveys, it then became an extreme outlier to the stream identified in the current analysis, albeit the MID discovery paper not mentioning any association with the comet, despite the shower discovery date post-dating 197P’s discovery. Indeed, another associated candidate (an asteroid) was noted in that paper, despite many of the particulars of its orbit being markedly different.

Given the evolutionary trends of the comet’s orbit there remained the possibility that the MID shower represented a stream from a discrete orbit from an earlier epoch. Accordingly, the values given for the orbit in the MID discovery paper were tested against the orbit for 197P/LINEAR used in this analysis and gave a result for  $D_J$  of 0.078, a respectable enough value. Therefore, given this similarity the MID shower is likely the same as the 197P shower and accordingly the former only requires its details updating following the current more complete number of orbits available, remembering that the “shower” is likely to

be a collection of slightly discrete streams due to the orbital evolution of the comet with little time having passed for dynamic relaxation, and that 197P should now be noted as the parent body to the May iota Draconids.

## 5 Conclusion

Examination of UKMON meteor orbits via  $D_J$  criterion testing revealed a likely association of 10 of the orbits with the comet 197P/LINEAR. An extended analysis using meteor orbits from other publicly available surveys extended the number of orbits by 151. Examination of the comet revealed a succession of close approaches to Jupiter, both in the past and in the future, not only leading to the comet orbit's perihelion distance coming within range sufficient for any meteoroids to be likely noted on Earth but oscillating at a value for the foreseeable future likely to make this the ongoing case, with even a possibility of crossing just within Earth's orbit in the more distant future. However, due to the evolution of the orbit coinciding with the evolution of multi-station video meteor monitoring to ever greater spatial and temporal coverage it cannot be shown as to whether an apparent recent increase, or even discovery, of such a shower is primarily due to this increased monitoring or to the orbital evolution. The presence of varying non-gravitational effects in the orbital particulars of the comet also suggest episodic outgassing thus complicating further any particular year's increase and/or decrease in meteors.

Taking this drift into account and its likely effect on radiant position and Solar Longitude over time, examination of extant meteor showers revealed that the May iota Draconids, though dissimilar and already given a candidate parent body in the literature, may in fact be connected to 197P/LINEAR which would make it the true parent body. Similarly, the larger picture provided by the increase in survey data available since the discovery of the May iota Draconids shows that the mean orbital and radiant and duration particulars need to be updated.

The periodic Jupiter Family Comet 197P/LINEAR due to aphelion interactions with Jupiter has recently evolved into an orbit with perihelion distance closer to Earth's orbit than hitherto known. The May iota Draconids may well be an early indication of the continued drift and evolution of the meteoroid stream. If so, the modern radiant of the shower is now centered nearer Right Ascension 233.1 degrees, Declination +59.1 degrees and Solar Longitude 67.1 degrees, in other words a week before and a week after a date centered around June 1<sup>st</sup>. It presents a number of slow-moving bright meteors and fireballs given its roughly 17 kms<sup>-1</sup> geocentric velocity. Modern surveys' coverage availability could lead to revealing results relatable to the comet's orbital variations whilst its parent body's variable perihelion distance remains close enough to Earth's orbit for at least the next Century.

## Acknowledgment

The meteor survey groups and especially their volunteers and operatives are expressly thanked not only for their work but for making their data public and thus available for analytical examination by all instead of just wallowing in a private archive. The individual groups are mentioned in the body text of the article and fully referenced below. Strangely, for the case of public domain scientific data, the Global Meteor Network (GMN) and UKMON data are released under the following licence<sup>4</sup>.

## References

- Campbell-Burns P., Kacerek R. (2014). "The UK Meteor Observation Network". *WGN, Journal of the International Meteor Organization*, **42**, 139–144.
- Jenniskens P., Baggaley J., Crumpton I., Aldous P., Pokorny P., Janches D., Gural P. S., Samuels D., Albers J., Howell A., Johannink C., Breukers M., Odeh M., Moskovitz N., Collison J., Ganju S. (2018). "A survey of southern hemisphere meteor showers". *Planetary Space Science*, **154**, 21–29.
- Jopek T. J. (1993). "Remarks on the meteor orbital similarity D-criterion". *Icarus*, **106**, 603–607.
- Kornoš L., Koukal J., Piffel R., and Tóth J. (2014). "EDMOND Meteor Database". In, Gyssens M., Roggemans P., Zoladek, P., editors, *Proceedings of the International Meteor Conference*, Poznań, Poland, Aug. 22-25, 2013. International Meteor Organization, pages 23–25.
- Šegon Damir, Gural Peter, Andrei Željko, Vida Denis, Skokić Ivica and Novoselnik Filip (2015). "Four possible new high-declination showers". *WGN, Journal of the International Meteor Organization*, **43**, 147–150.
- SonotaCo (2009). "A meteor shower catalog based on video observations in 2007-2008". *WGN, Journal of the International Meteor Organization*, **37**, 55–62.
- Vida D., Gural P., Brown P., Campbell-Brown M., Wiegert P. (2019). "Estimating trajectories of meteors: an observational Monte Carlo approach - I. Theory". *Monthly Notices of the Royal Astronomical Society*, **491**, 2688–2705.
- Vida D., Gural P., Brown P., Campbell-Brown M., Wiegert P. (2019). "Estimating trajectories of meteors: an observational Monte Carlo approach - II. Results". *Monthly Notices of the Royal Astronomical Society*, **491**, 3996–4011.

<sup>4</sup> <https://creativecommons.org/licenses/by/4.0/>

# A potential new summer shower in Lacerta

John Greaves

midmet@mail.com

Examination of archived sporadic meteor orbits from the UKMON multi-station meteor survey suggests a summer shower centered in Lacerta.

## 1 Methodology

Archival data from the UKMON meteor survey (e.g. Campbell-Burns and Kacerek, 2014) were obtained from the UKMON online public data archive and all the orbits flagged as being sporadic retained whilst all other orbits were removed, leading to 16252 remaining orbits. The orbital part of the data was then analyzed against a copy of itself for all 16252 orbits utilizing the Jopek (1993)  $D_J$  criterion modification, henceforth referred to as  $D_J$ , to obtain matching orbit pairs using a  $D_J$  upper threshold limit of 0.10. This particular processing time took over four days on a 3GHz intel quadcore computer.

The resultant output was examined for radiant clustering via passive visual inspection of the radiants' positions plotted against the sky with solar longitude and geocentric velocity being scaled into the graphical representation. Following on from this some indication of a reasonably tight but thinly populated grouping was noted in Lacerta and accordingly a wider  $D_J$  test was made upon the mean orbital particulars of those meteors using data from multi-station meteor survey publicly available data archives of SonotaCo Network (e.g. SonotaCo, 2009), CAMS (e.g. Jenniskens et al., 2018) and EDMOND (e.g. Kornoš et al., 2014) and Global Meteor Network (Vida et al., 2019a; 2019b). As various regional meteor surveys can not only provide their own dataset but contribute it to other surveys the combined datasets used in this search had the potential for some duplicates, accordingly the results were sorted on Right Ascension and any objects in the resultant output having a commonality of Right Ascension, declination and solar longitude had their duplicates removed. This led to the removal of one orbit, with one other orbit being removed as its orbit had a hyperbolic solution. A new mean orbit was then derived from the results and that orbit further tested against the above-mentioned datasets using the  $D_J$  criterion.

## 2 Results

The analysis resulted in a total of 21 meteor orbits meeting the  $D_J < 0.100$  threshold, of which 13 have  $D_J < 0.008$  and 4 have  $D_J < 0.006$ . The meteoroids spanned the years 2009 to 2021, with 2012 the only missing year, ranging from only one some years to four each in 2015 and 2016. However, due to the nature of the surveys used all bar one of the

meteors were brighter than magnitude +1 and of these 12 were brighter than magnitude 0, essentially fireballs, with the brightest magnitude  $-3.4$ . Thus, there is a selection effect for only the brightest of potential meteors from this shower having been detected. The distribution of meteors as a function of solar longitude is displayed in *Figure 1*, and the particulars of the meteors are given in *Table 1*.

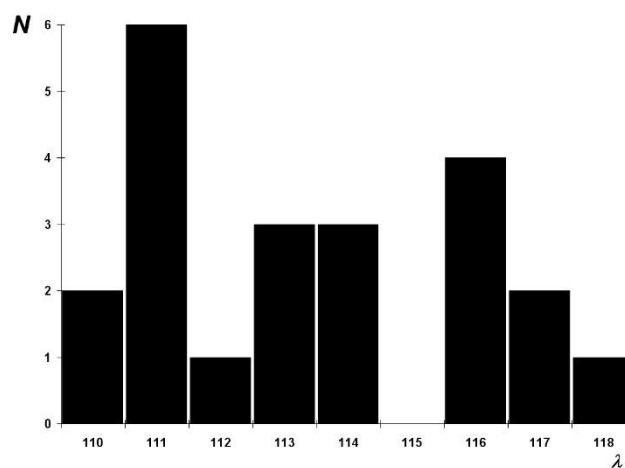


*Figure 1* – The number of meteors as a function of  $\lambda_0$  (solar longitude) in degrees.

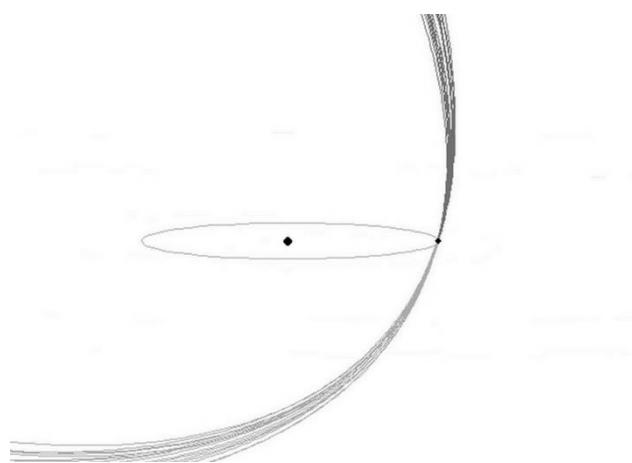


*Figure 2* – The orbits of the 21 meteors depicted for a representative date of July 16<sup>th</sup> where the Earth and Sun are represented by black dots, with the Earth's orbit shown as an ellipse and the meteor orbits shown with the above ecliptic sections in dark grey and the below ecliptic section in lighter grey.

*Table 1* – Mean and Median plus standard deviation on the Mean along with Minimum and Maximum values of the meteor orbits are given for :- Right Ascension (in degrees); declination (in degrees); solar longitude,  $\lambda_{\odot}$ , (in degrees); geocentric velocity,  $v_g$ , (km/s); perihelion distance,  $q$ , (AU); eccentricity,  $e$ ; inclination,  $i$ , (in degrees); argument of perihelion,  $\omega$ , (in degrees); ascending node,  $\Omega$ , (in degrees); ecliptic longitude,  $\lambda$ , (in degrees); ecliptic latitude,  $\beta$ , (in degrees); ecliptic latitude minus solar longitude,  $\lambda - \lambda_{\odot}$ , (in degrees) and longitude of perihelion,  $\Pi$ , (in degrees).

	<i>R.A.</i>	<i>Dec</i>	$\lambda_{\odot}$	$v_g$	$q$	$e$	$i$	$\omega$	$\Omega$	$\lambda$	$\beta$	$\lambda - \lambda_{\odot}$	$\Pi$
Mean	342.3	44.1	114.0	53.5	0.935	0.922	98.5	213.4	114.0	6.3	46.5	252.3	327.5
Median	342.4	44.0	113.7	53.3	0.937	0.924	97.8	213.6	113.7	6.0	46.5	252.1	326.6
Stand. Dev.	2.4	1.0	2.6	0.8	0.013	0.033	1.6	2.9	2.6	2.5	1.0	1.5	4.5
Min	338.8	42.7	110.6	52.1	0.909	0.849	95.7	209.2	110.6	2.6	44.5	249.3	320.8
Max	346.8	46.7	118.8	54.9	0.955	0.990	101.4	218.4	118.8	10.6	48.6	255.0	335.1

The similarity of the orbits is revealed in *Figure 2* where the ecliptic crossing path at a date of July 16<sup>th</sup> is depicted with the Earth and Sun shown. *Figure 3* lists the disposition of the meteors in terms of geocentric ecliptic latitude  $\beta_g$  in Sun-centered geocentric longitude with respect to the UKMON sporadic meteor background, whilst *Figure 4* does the same for the case of the meteor orbital inclinations  $i$  against the longitudes of perihelion  $\Pi$ . Finally *Figure 5* denotes the position of the 21 meteors in Right Ascension and declination with respect to the full entirety of the 16252 sporadic UKMON meteors used in the analysis via Aitoff projection.

### 3 Conclusion

Examination of 16525 sporadic UKMON meteor orbits suggested a clustering of same geocentric velocity meteors

in Lacerta and subsequently an iteratively derived mean orbit for an area in Lacerta was tested against an extended dataset of orbital data. This resulted in 21 potential meteor orbits from which mean and median and standard deviation particulars of radiant, Solar Longitude, and orbit were derived.

This led to a potential shower of some small radiant dispersion but relatively tight date of presentation of around 1 to 4 bright to fireball level medium to fast meteors per annum, near a representative radiant of Right Ascension 342 degrees, declination 44 degrees centered around a solar longitude of 114 degrees (around July 16<sup>th</sup>) and a geocentric velocity of 53.5 km/s.

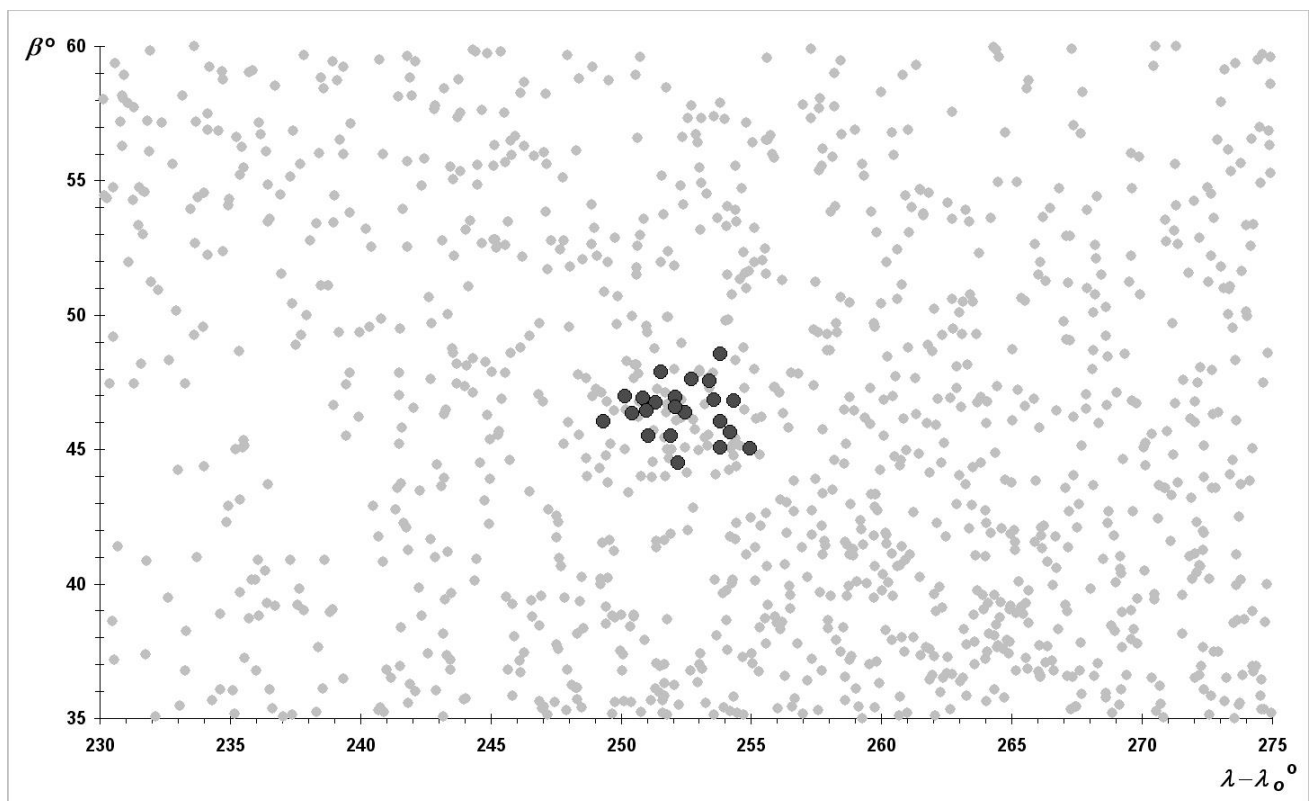


*Figure 3* – A depiction of the ecliptic latitude,  $\beta$ , with respect to the difference between the Sun-centered ecliptic longitude,  $\lambda - \lambda_{\odot}$ , for the shower meteors depicted as black filled circles and the UKMON sporadic meteor background in light grey circles.

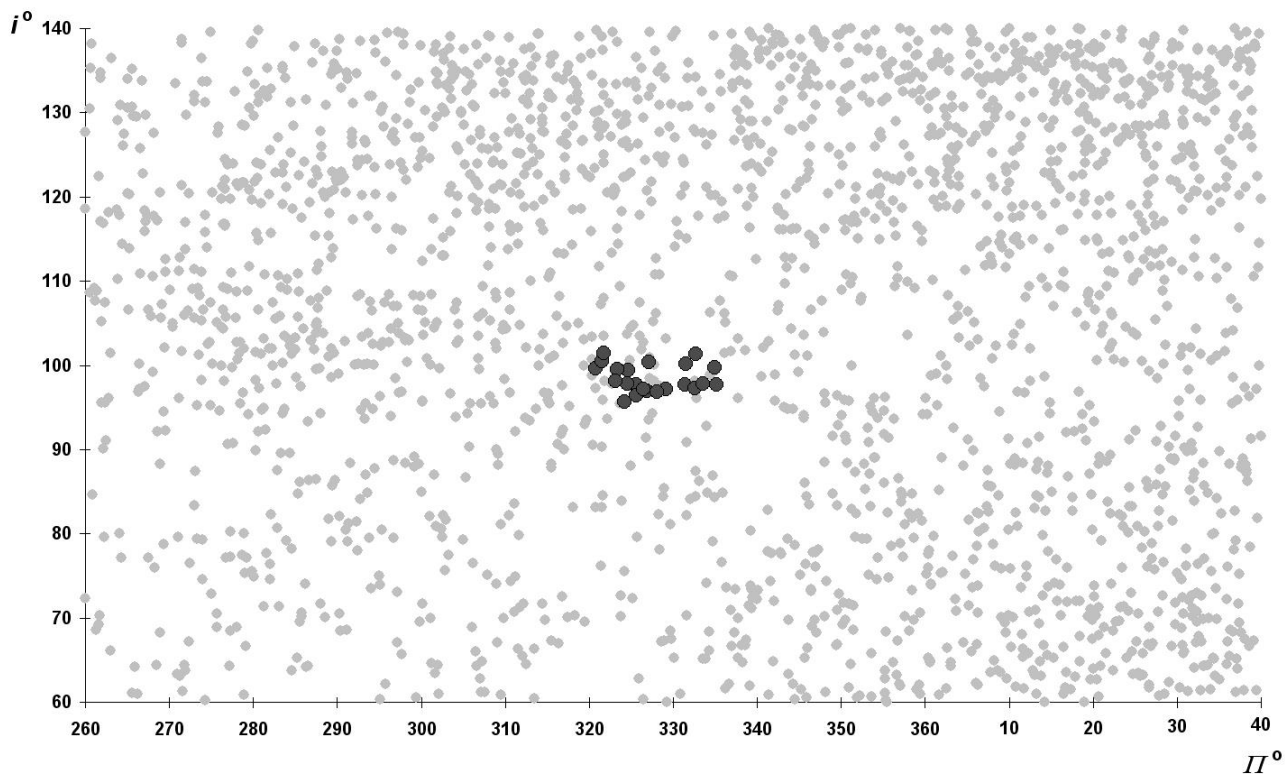


Figure 4 – A depiction of the orbital inclination,  $i$ , with respect to the longitude of perihelion,  $\Pi$ , for the shower meteors depicted as black filled circles and the UKMON sporadic meteor background in light grey circles.

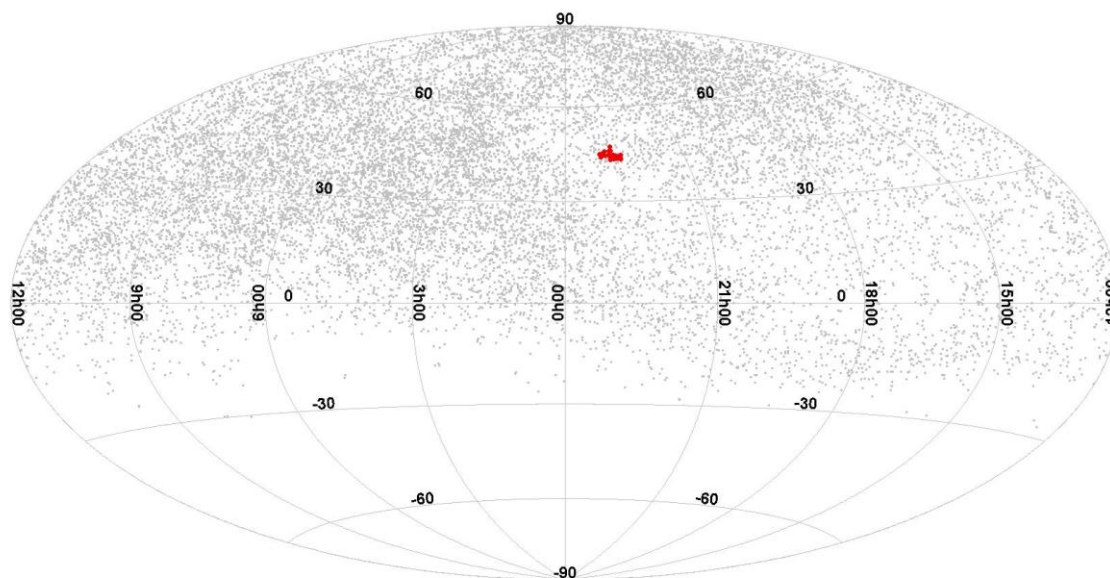


Figure 5 – The Right Ascension and declination of the shower meteors are shown in Aitoff Projection denoted as red filled circles with the entirety of the 16525 sporadic UKMON meteors denoted as light grey dots. Grid lines are shown for every 3 hours of Right Ascension and every 30 degrees of declination.

## Acknowledgment

The meteor survey groups and especially their volunteers and operatives are expressly thanked not only for their work but for making their data public and thus available for analytical examination by all instead of just wallowing in a

private archive. The individual groups are mentioned in the body text of the article and fully referenced below. Strangely, for the case of public domain scientific data, the Global Meteor Network (GMN) and UKMON data are released under the following licence<sup>5</sup>. The Aitoff Projection was generated using TopCat<sup>6</sup>.

<sup>5</sup> <https://creativecommons.org/licenses/by/4.0/>

<sup>6</sup> <http://www.star.bris.ac.uk/~mbt/topcat/>

## References

- Campbell-Burns P., Kacerek R. (2014). “The UK Meteor Observation Network”. *WGN, Journal of the International Meteor Organization*, **42**, 139–144.
- Jenniskens P., Baggaley J., Crumpton I., Aldous P., Pokorny P., Janches D., Gural P. S., Samuels D., Albers J., Howell A., Johannink C., Breukers M., Odeh M., Moskovitz N., Collison J., Ganju S. (2018). “A survey of southern hemisphere meteor showers”. *Planetary Space Science*, **154**, 21–29.
- Jopek T. J. (1993). “Remarks on the meteor orbital similarity D-criterion”. *Icarus*, **106**, 603–607.
- Kornoš L., Koukal J., Piffel R., and Tóth J. (2014). “EDMOND Meteor Database”. In, Gyssens M., Roggemans P., Zoladek, P., editors, *Proceedings of the International Meteor Conference*, Poznań, Poland, Aug. 22-25, 2013. International Meteor Organization, pages 23–25.
- SonotaCo (2009). “A meteor shower catalog based on video observations in 2007-2008”. *WGN, Journal of the International Meteor Organization*, **37**, 55–62.
- Vida D., Gural P., Brown P., Campbell-Brown M., Wiegert P. (2019). “Estimating trajectories of meteors: an observational Monte Carlo approach - I. Theory”. *Monthly Notices of the Royal Astronomical Society*, **491**, 2688–2705.
- Vida D., Gural P., Brown P., Campbell-Brown M., Wiegert P. (2019). “Estimating trajectories of meteors: an observational Monte Carlo approach - II. Results”. *Monthly Notices of the Royal Astronomical Society*, **491**, 3996–4011.

# The Southwestern Europe Meteor Network: development of new artificial intelligence tools and remarkable fireballs observed from January to February 2022

J. M. Madiedo<sup>1</sup>, J. L. Ortiz<sup>1</sup>, J. Izquierdo<sup>2</sup>, P. Santos-Sanz<sup>1</sup>, J. Aceituno<sup>3</sup>,  
E. de Guindos<sup>3</sup>, P. Yanguas<sup>4</sup>, J. Palacián<sup>4</sup>, A. San Segundo<sup>5</sup>, D. Ávila<sup>6</sup>, B. Tosar<sup>7</sup>,  
A. Gómez-Hernández<sup>8</sup>, J. Gómez-Martínez<sup>8</sup> and A. I. Aimee<sup>9</sup>

<sup>1</sup> Departamento de Sistema Solar, Instituto de Astrofísica de Andalucía (IAA-CSIC), 18080 Granada, Spain  
madiedo@cica.es, ortiz@iaa.es, psantos@iaa.es

<sup>2</sup> Departamento de Física de la Tierra y Astrofísica, Universidad Complutense de Madrid, 28040 Madrid, Spain  
jizquierdo9@gmail.com

<sup>3</sup> Observatorio Astronómico de Calar Alto (CAHA), E-04004, Almería, Spain  
aceitun@caha.es, guindos@caha.es

<sup>4</sup> Departamento de Estadística, Informática y Matemáticas e Institute for Advanced Materials and Mathematics,  
Universidad Pública de Navarra, 31006 Pamplona, Navarra, Spain  
yanguas@unavarra.es, palacian@unavarra.es

<sup>5</sup> Observatorio El Guijo (MPC J27), Galapagar, Madrid, Spain  
mpcj27@outlook.es

<sup>6</sup> Estación de Meteoros de Ayora, Ayora, Valencia, Spain  
David\_ayora007@hotmail.com

<sup>7</sup> Casa das Ciencias. Museos Científicos Coruñeses. A Coruña, Spain  
borjatosar@gmail.com

<sup>8</sup> Estación de Registro La Lloma, Olocau, Valencia, Spain  
curso88@gmail.com

<sup>9</sup> Southwestern Europe Meteor Network, 41012 Sevilla, Spain  
swemn.server@gmail.com

In this work we focus on the development of an artificial intelligence in the framework of the Southwestern Europe Meteor Network (SWEMN) and the SMART project. This is named AIMIE and is capable of writing scientific contributions from fireball data included in the SWEMN database. As an example of the capabilities of AIMIE we also present in this work a report containing the analysis of some of the remarkable fireballs spotted from our meteor-observing stations from January to February 2022. These have been observed over the Iberian Peninsula, and their absolute magnitude ranges from  $-10$  to  $-13$ . One of these bolides was a potential meteorite-dropper. The emission spectrum of one of the events is also discussed.

## 1 Introduction

The Southwestern Europe Meteor Network (SWEMN) is a research project coordinated in Spain from the Institute of Astrophysics of Andalusia (IAA-CSIC) with the aim to analyze the Earth's meteoric environment. This network is also integrated by researchers from the Complutense University of Madrid (UCM), the Public University of Navarre (UPNA), and the Calar Alto Observatory (CAHA). In 2021 we decided to open the project to the amateur community. This Pro-Am collaboration resulted in the deployment of new meteor stations in our country that provide their results to our network.

In order to identify and analyze meteors in the Earth's atmosphere, SWEMN develops the Spectroscopy of Meteoroids by means of Robotic Technologies (SMART) survey (Madiedo, 2014; Madiedo, 2017). And to improve our knowledge about the Earth-Moon meteoric environment, SMART works in close connection with another project conducted by IAA-CSIC: the MIDAS survey (Moon Impacts Detection and Analysis System). MIDAS uses the Moon as a laboratory that provides information about meteoroids hitting the lunar ground (Ortiz et al., 2015; Madiedo et al. 2015a, b). A strong synergy has been proved to exist between this survey and the SMART project (Madiedo et al. 2015a, b).

Recently, we announced the development of the first digital and interactive meteor database containing meteor events recorded over Spain and surrounding regions (Madiedo et al., 2021). And later on, we discussed the development of artificial intelligence (AI) tools designed to handle the contents of this database, and also capable of disseminating in social networks and media information about relevant fireballs recorded by our systems (Madiedo et al., 2022). Now we have gone one step further by developing an AI which is capable of writing a scientific work by employing the information contained in the above-mentioned database. We describe here the main features of this innovative tool, which has been named AIMIE (acronym for Artificial Intelligence with Meteoroid Environment Expertise). We also focus on the description of some of the most remarkable fireballs recorded by our systems from January to February 2022. The report describing these events has been fully written by AIMIE. So, this work is an example of the capabilities of the current version of this new software.

## 2 New applications of the SWEMN digital database: AIMEE

Software development has been a priority since the SMART project was started in 2006. Thus, this software was necessary in order to calculate meteor trajectories and meteoroid orbits. But also, to analyze meteor spectra and to automate the operation of remote meteor-stations (Madiedo, 2014). In addition, the lack of enough manpower made also necessary to create software tools that could accelerate different parts of the data processing and results dissemination pipeline. The first AI methods employed by the SWEMN network were implemented in the SAMIA software developed by the first author to handle the contents of the SWEMN meteor database and also to automatically derive valuable information from the events contained in it (Madiedo et al., 2021). Next, additional AI methods were implemented to disseminate our scientific results among the general public through social networks (mainly Twitter and Facebook), information media, our website, and also YouTube (Madiedo et al., 2022). Before these tools were available, the time consumed by this dissemination process was very significant, since all of the information necessary for this purpose was gathered manually, and the corresponding reports were also prepared by hand.

The AI in the SAMIA software was recently expanded to write autonomously scientific communications from the information stored in the SWEMN database. This includes abstracts for congresses, but also papers like this one. This AI was named AIMEE, which is the acronym for Artificial Intelligence with Meteoroid Environments Expertise. The user only needs to specify the author's list and, of course, which event(s) must be included in the work. The information stored for each event in the SWEMN database is so comprehensive (Madiedo et al., 2021), that in most cases AIMEE can find there all of the information necessary to prepare the communication. If some information is missing, the IA asks the user to provide it. But AIMEE can

also try to find additional information on its own by using external databases. Thus, for instance, it can obtain data about meteoroid streams from the IAU meteor database<sup>7</sup>. And it can find bibliographic references by employing the SAO/NASA Astrophysics Data System (ADS)<sup>8</sup>. In addition, by employing geolocation services, AIMEE can also know the specific and precise geographic areas (country, region, province, city, seas, etc.) that a particular event overflowed along its atmospheric trajectory.

The software contains a database with predefined templates for congresses and journals. In this way, AIMEE can compose the text by following the style and maximum length requested in each case. At this moment AIMEE is capable of writing communications for several congresses: EPSC, LPSC, and Meteoroids. But also, for the MeteorNews e-zine. In a near future, templates for peer-review journals will be implemented. The text created by AIMEE is written in MS-Word DOC format and covers the whole work: communication title, authors and their affiliations, abstract, materials and methods, figures, tables, etc. Even the conclusions and references. The user can perform modifications to this text manually or ask the IA to write again a given section of the communication in a different way.

Finally, AIMEE can provide feedback to the SWEMN meteor database if new information was obtained for a specific event during the preparation of the scientific communication.

As an example of the current capabilities of AIMEE, we present below a report prepared by this AI in relation to a series of remarkable bolides recorded by the SWEMN network along January and February 2022. The remaining text appearing in this work below this paragraph was written entirely by AIMEE.

## 3 Instrumentation and methods

To record the events analyzed in this work we have employed Watec 902H2 and Watec 902 Ultimate cameras. Their field of view ranges from  $62 \times 50$  degrees to  $14 \times 11$  degrees. To record meteor spectra we have attached holographic diffraction gratings (1000 lines/mm) to the lens of some of these devices. We have also employed digital CMOS color cameras (models Sony A7S and A7SII) operating in HD video mode ( $1920 \times 1080$  pixels). These cover a field of view of around  $70 \times 40$  degrees. A detailed description of this hardware and the way it operates was given in previous works (Madiedo, 2017).

The atmospheric path and radiant of meteors, and also the orbit of their parent meteoroids, were obtained with the SAMIA software, developed by J. M. Madiedo. This program employs the planes-intersection method (Ceplecha, 1987). The emission spectrum presented in this work was analyzed with the CHIMET software (Madiedo, 2017).

<sup>7</sup> <http://www.astro.amu.edu.pl/~jopek/MDC2007/>

<sup>8</sup> <https://ui.adsabs.harvard.edu/>



Figure 1 – Stacked image of the SWEMN20220102\_060558 “Santa Margarida” bolide as recorded from Sevilla.

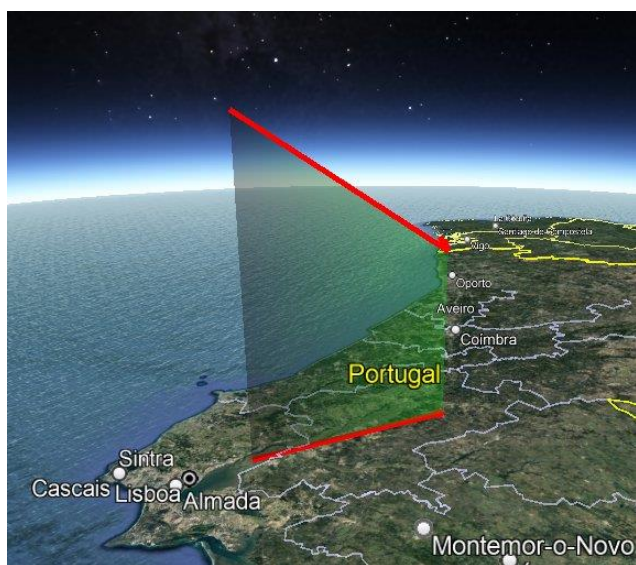


Figure 2 – Atmospheric path and projection on the ground of the trajectory of the SWEMN20220102\_060558 meteor.

#### 4 Description of the 2022 January 2 event

We spotted this bright fireball (Figure 1) from the meteor-observing stations located at Calar Alto, Sierra Nevada, Sevilla, La Sagra (Granada), Huelva, El Aljarafe, and La Hita (Toledo). The bright meteor was recorded on 2022 January 2, at  $6^{\text{h}}05^{\text{m}}58 \pm 0.1^{\text{s}}$  UT. The event had a peak absolute magnitude of  $-12.0 \pm 0.5$ , and was included in our meteor database with the code SWEMN20220102\_060558. A video showing images of the bolide and its trajectory was uploaded to YouTube<sup>9</sup>.

##### Atmospheric trajectory, radiant and orbit

The event overflowed Portugal. It began at an altitude  $H_b = 119.9 \pm 0.5$  km near from the zenith of the locality of Alhandra, and the terminal point of the luminous path was located at a height  $H_e = 62.2 \pm 0.5$  km, over the locality of Santa Margarida. The apparent radiant was located at the equatorial coordinates  $\alpha = 146.67^\circ$ ,  $\delta = -4.54^\circ$ . Besides, we found that the meteoroid stroke the atmosphere with a

velocity  $v_\infty = 58.1 \pm 0.4$  km/s. The trajectory in the Earth’s atmosphere of the bright meteor is shown in Figure 2.

Table 1 – Orbital data (J2000) of the progenitor meteoroid of the SWEMN20220102\_060558 fireball before its encounter with our planet.

$a$ (AU)	$13.3 \pm 5.8$	$\omega$ ( $^\circ$ )	$123.8 \pm 01.0$
$e$	$0.983 \pm 0.006$	$\Omega$ ( $^\circ$ )	$101.517026 \pm 10^{-5}$
$q$ (AU)	$0.224 \pm 0.004$	$i$ ( $^\circ$ )	$121.0 \pm 0.5$

This event was named “Santa Margarida”, since the bright meteor was located over this locality during its final phase. The parameters of the heliocentric orbit of the parent meteoroid before its encounter with our planet are included in Table 1. The geocentric velocity of the meteoroid was  $v_g = 57.3 \pm 0.4$  km/s. These parameters and the derived radiant confirm that the bright meteor was generated by the sigma Hydrids (IAU code HYD#0016) (Jenniskens et al., 2016). According to the value estimated for the Tisserand parameter with respect to Jupiter ( $T_J = 0.09$ ), the meteoroid followed a cometary orbit before impacting the Earth’s atmosphere. Figure 3 shows the orbit in the Solar System of the meteoroid.

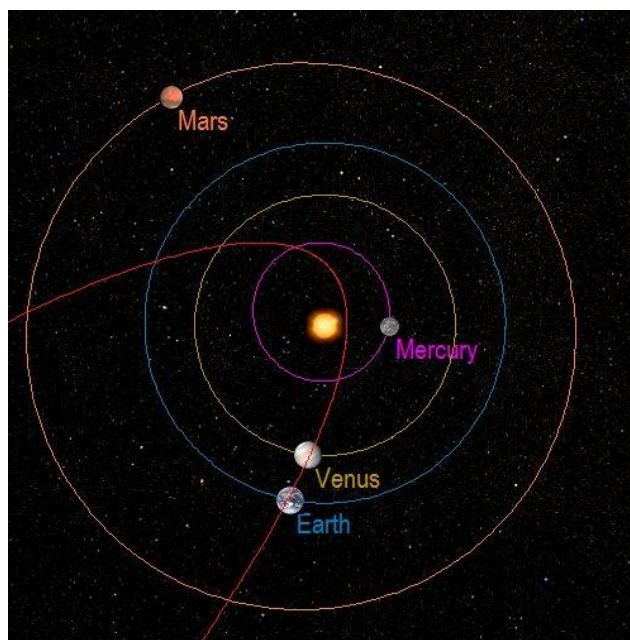


Figure 3 – Projection on the ecliptic plane of the orbit of the SWEMN20220102\_060558 event.

#### 5 The 2022 January 9 bolide

This stunning fireball (Figure 4) was recorded by our systems on 2022 January 9, at  $0^{\text{h}}18^{\text{m}}08 \pm 0.1^{\text{s}}$  UT. The event had a peak absolute magnitude of  $-13.0 \pm 0.5$ . The bolide was included in our meteor database with the code SWEMN20220109\_001808.

##### Atmospheric path, radiant and orbit

By calculating the luminous path of the bolide we deduced that the event overflowed the south of Spain. The ablation process of the meteoroid began at a height  $H_b = 103.5 \pm 0.5$

<sup>9</sup> <https://youtu.be/xkLRm1WQnk4>

km almost over the locality of Montecorto (province of Cádiz), and the bolide penetrated the atmosphere till a final height  $H_e = 31.0 \pm 0.5$  km near from the zenith of the locality of Paradas (province of Sevilla). The apparent radiant was located at the equatorial coordinates  $\alpha = 127.24^\circ$ ,  $\delta = -4.67^\circ$ . The meteoroid hit the atmosphere with an initial velocity  $v_\infty = 41.7 \pm 0.4$  km/s. *Figure 5* shows the atmospheric path of the bright meteor. We named this bright meteor “Montecorto”, because the bolide passed near from the zenith of this locality during its initial phase.

The orbital parameters of the parent meteoroid before its encounter with our planet have been included in *Table 2*. The geocentric velocity obtained for the particle yields  $v_g = 40.2 \pm 0.4$  km/s. These values and the calculated radiant confirm that the fireball was generated by the alpha Hydrids (IAU code AHY#0331) (Jenniskens et al., 2016).



*Figure 4* – Stacked image of the SWEMN20220109\_001808 “Montecorto” bolide as recorded from Calar Alto (CAHA).

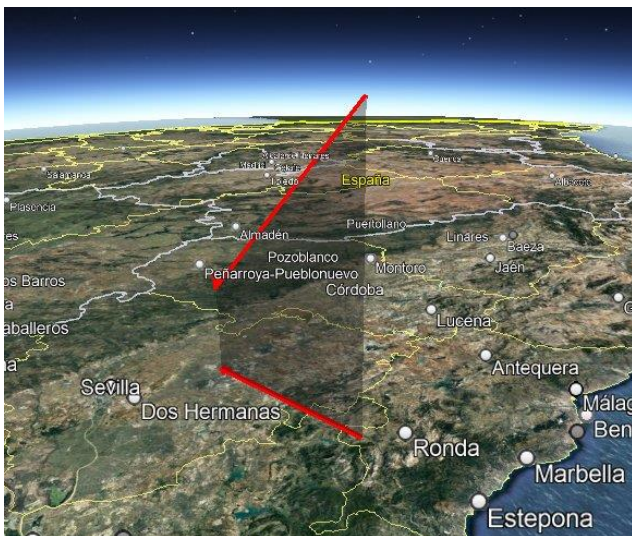


*Figure 5* – Atmospheric path and projection on the ground of the trajectory of the SWEMN20220109\_001808 fireball.

According to the value calculated for the Tisserand parameter referred to Jupiter ( $T_J = 1.13$ ), before striking our

atmosphere the particle was moving on a cometary orbit. *Figure 6* shows the orbit in the Solar System of the meteoroid.

*Table 2* – Orbital data (J2000) of the progenitor meteoroid before its encounter with our planet.

$a$ (AU)	$8.0 \pm 1.8$	$\omega$ ( $^\circ$ )	$114.7 \pm 00.4$
$e$	$0.962 \pm 0.008$	$\Omega$ ( $^\circ$ )	$108.400679 \pm 10^{-5}$
$q$ (AU)	$0.299 \pm 0.002$	$i$ ( $^\circ$ )	$44.3 \pm 0.5$

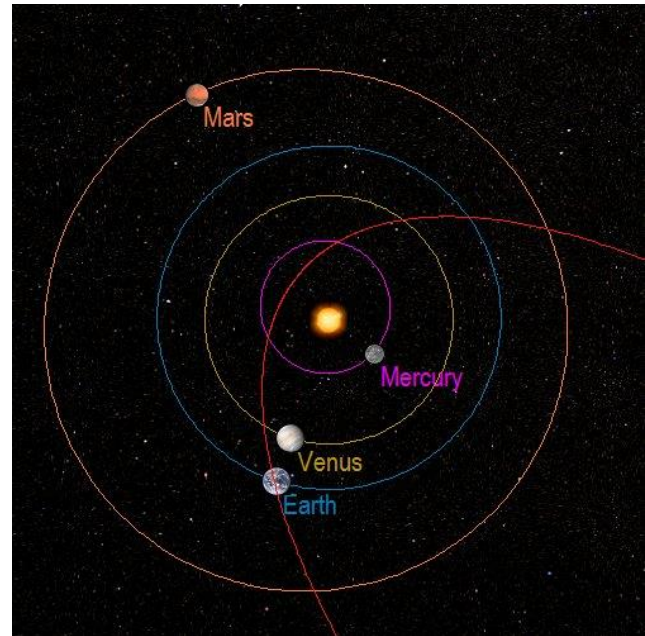


*Figure 6* – Projection on the ecliptic plane of the orbit of the SWEMN20220109\_001808 “Montecorto” meteor.

## 6 The 2022 January 14 fireball

We captured this stunning bolide from the meteor-observing stations located at Calar Alto, Sierra Nevada, Sevilla, La Sagra (Granada), Huelva, El Aljarafe, Madrid (Universidad Complutense), and La Hita (Toledo) (*Figure 7*). The fireball was spotted on 2022 January 14, at  $21^{\text{h}}27^{\text{m}}07 \pm 0.1^{\text{s}}$  UT and had a peak absolute magnitude of  $-12.0 \pm 0.5$ . It was included in our meteor database with the code SWEMN20220114\_212707. This bright meteor can be viewed on this YouTube video<sup>10</sup>.

### Atmospheric path, radiant and orbit

According to our calculations, the fireball overflowed the south of Spain. Its initial altitude was  $H_b = 85.3 \pm 0.5$  km near from the vertical of the locality of Ventillas (province of Ciudad Real). The bolide penetrated the atmosphere till a final height  $H_e = 23.6 \pm 0.5$  km near from the vertical of the locality of Solana del Pino (province of Ciudad Real). The position found for the apparent radiant correspond to the equatorial coordinates  $\alpha = 63.68^\circ$ ,  $\delta = +39.26^\circ$ . The entry velocity in the atmosphere concluded for the parent meteoroid was  $v_\infty = 13.6 \pm 0.3$  km/s. The atmospheric path of the luminous event is shown in *Figure 8*.

<sup>10</sup> [https://youtu.be/b7w2qdBY\\_R4](https://youtu.be/b7w2qdBY_R4)

We named this bright meteor “Ventillas”, because the bolide was located near the zenith of this locality during its initial phase. The orbital parameters of the parent meteoroid before its encounter with our planet are included in *Table 3*, and the geocentric velocity derived in this case was  $v_g = 7.9 \pm 0.5$  km/s. By taking into account these orbital data and the radiant position, it was concluded that the fireball was generated by a sporadic meteoroid. From the value derived for the Tisserand parameter with respect to Jupiter ( $T_J = 3.77$ ), we found that the meteoroid was moving on an asteroidal orbit before entering our atmosphere. This orbit is shown in *Figure 9*.

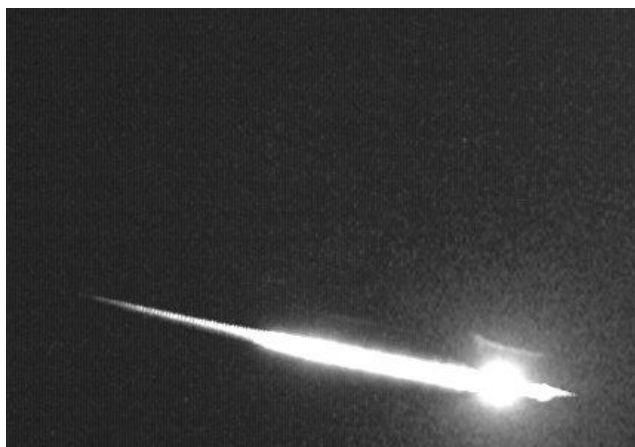


Figure 7 – Stacked image of the SWEMN20220114\_212707 “Ventillas” meteor as recorded from La Hita.

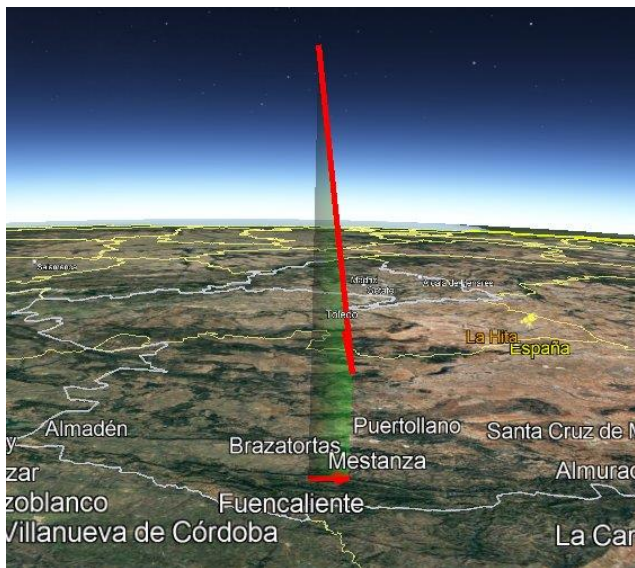


Figure 8 – Projection on the ground of the trajectory of the SWEMN20220114\_212707 fireball.

Table 3 – Orbital data (J2000) of the progenitor meteoroid before its encounter with our planet.

$a$ (AU)	$1.9 \pm 0.1$	$\omega$ (°)	$201.8 \pm 00.5$
$e$	$0.49 \pm 0.03$	$\Omega$ (°)	$294.433674 \pm 10^{-5}$
$q$ (AU)	$0.960 \pm 0.001$	$i$ (°)	$3.9 \pm 0.2$

Our analysis reveals that the meteoroid was not completely ablated in the atmosphere. Thus, we obtained a non-zero but small (below 50 grams) terminal mass. The dark flight was also analyzed and the landing area of the surviving mass

was determined. An expedition was organized to that area by experts in meteorites in collaboration with the SWEMN network. However, the meteorite was not found.

**Emission spectrum**

The emission spectrum of the bolide was also recorded from the meteor-observing station located at La Hita. This signal was calibrated in wavelength by employing typical lines appearing in meteor spectra, and then corrected by taking into account the sensitivity of the recording device. The resulting calibrated emission spectrum is shown in *Figure 10*. This plot shows the most remarkable lines identified in the spectrum. These contributions correspond to Na I-1 (588.9 nm), Mg I-2 (516.7 nm), Fe I-4 (385.6 nm), Fe I-41 (441.5 nm), Fe I-42, Fe I-43 (414.3 nm), Fe I-15 (526.9 nm), and Fe I-318.

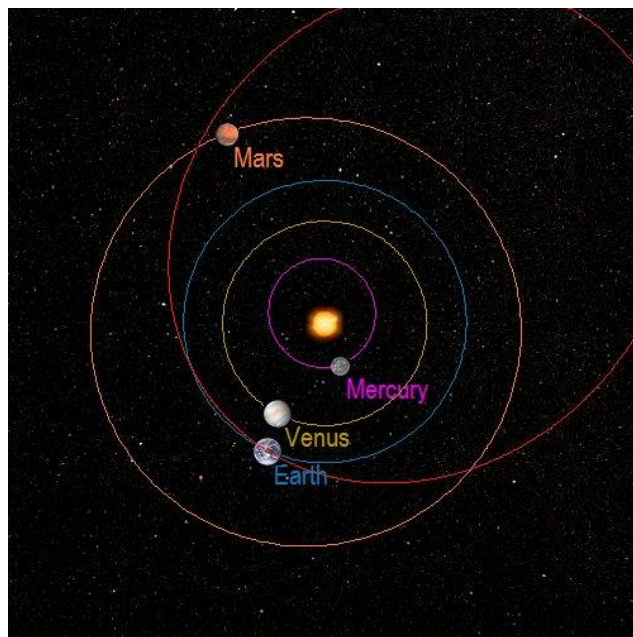


Figure 9 – Projection on the ecliptic plane of the orbit of the SWEMN20220114\_212707 event.

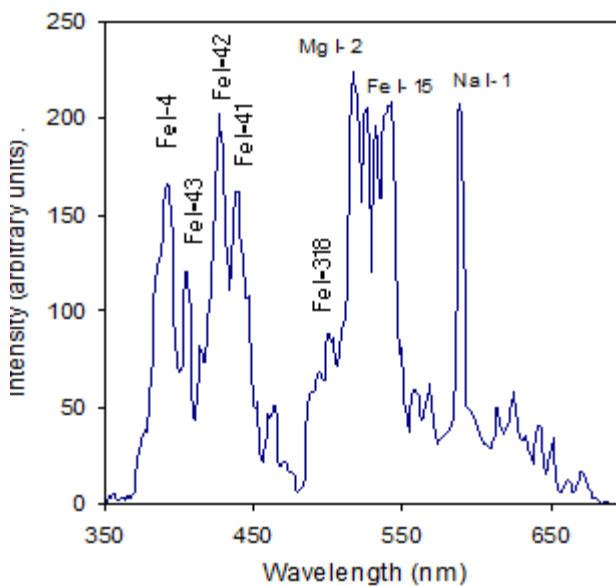


Figure 10 – Calibrated spectrum of the SWEMN20220114\_212707 bolide.

## 7 Description of the 2022 January 18 event

We captured this bright bolide from the meteor-observing stations located at Calar Alto, Sierra Nevada, Sevilla, Huelva y La Sagra (Granada). The event was spotted on 2022 January 18, at  $18^{\text{h}}20^{\text{m}}54 \pm 0.1^{\text{s}}$  UT (*Figure 11*). It had a peak absolute magnitude of  $-11.0 \pm 0.5$ . The fireball was included in our meteor database with the code SWEMN20220118\_182054. A video about this bolide can be viewed on YouTube<sup>11</sup>. A wide number of casual observers saw how the bright meteor crossed the sky and reported the event on social networks.

### Atmospheric path, radiant and orbit

It was obtained by calculating the trajectory in the atmosphere of the event that the bright meteor overflowed the Mediterranean Sea. Its initial altitude was  $H_b = 77.1 \pm 0.5$  km over the sea. The bolide penetrated the atmosphere till a final height  $H_e = 29.6 \pm 0.5$  km over the sea. From the analysis of the atmospheric path, we also found that the apparent radiant was located at the position  $\alpha = 321.69^\circ$ ,  $\delta = +78.04^\circ$ . The pre-atmospheric velocity inferred for the meteoroid yields  $v_\infty = 14.0 \pm 0.3$  km/s. The path in the atmosphere of the event is shown in *Figure 12*.



*Figure 11* – Stacked image of the SWEMN20220118\_182054 meteor.

*Table 4* – Orbital data (J2000) of the progenitor meteoroid before its encounter with our planet.

$a$ (AU)	$1.13 \pm 0.02$	$\omega$ ( $^\circ$ )	$186.8 \pm 00.4$
$e$	$0.13 \pm 0.02$	$\Omega$ ( $^\circ$ )	$298.346236 \pm 10^{-5}$
$q$ (AU)	$0.9830 \pm 0.0001$	$i$ ( $^\circ$ )	$15.6 \pm 0.7$

The parameters of the heliocentric orbit of the progenitor meteoroid before its encounter with our planet are contained in *Table 4*. The calculated value of the geocentric velocity of this particle is  $v_g = 8.6 \pm 0.4$  km/s. With these data and the radiant position, we inferred that the parent meteoroid belonged to the sporadic background. The Tisserand

parameter with respect to Jupiter yields  $T_J = 5.4$ , which shows that this meteoroid was moving on an asteroidal orbit before entering the atmosphere. This orbit is shown in *Figure 13*.

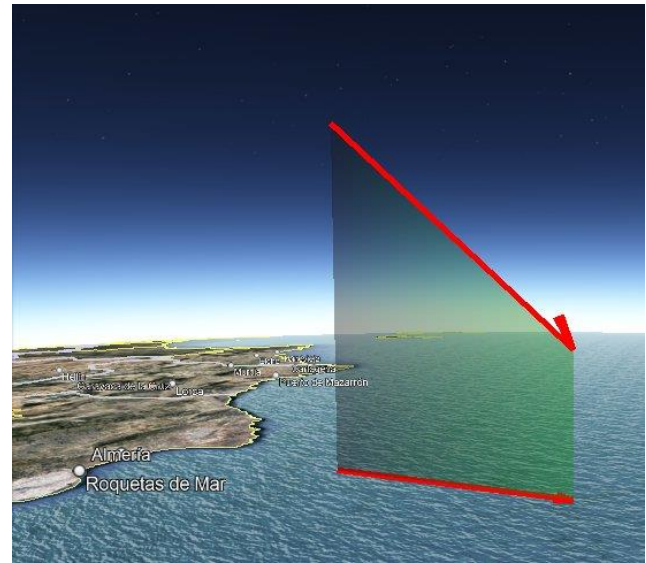


*Figure 12* – Atmospheric path and projection on the ground of the trajectory of the SWEMN20220118\_182054 bolide.

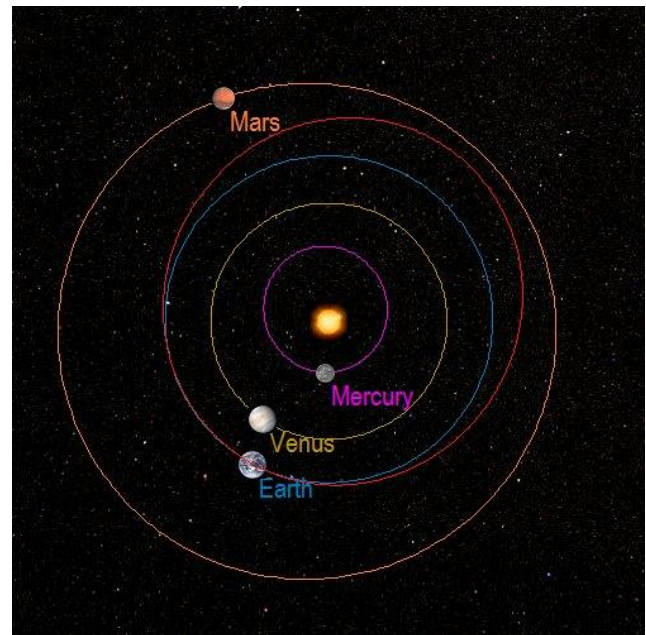


*Figure 13* – Projection on the ecliptic plane of the orbit of the SWEMN20220118\_182054 event.

## 8 The 2022 January 19 meteor

This gorgeous event was spotted on 2022 January 19, at  $4^{\text{h}}11^{\text{m}}03 \pm 0.1^{\text{s}}$  UT. The bolide (*Figure 14*) had a peak absolute magnitude of  $-11.0 \pm 1.0$ . We listed it in our meteor database with the code SWEMN20220119\_041103. A video showing images of this bolide and its atmospheric trajectory was uploaded to YouTube<sup>12</sup>.

### Atmospheric path, radiant and orbit

According to the analysis of the trajectory in the atmosphere of the bright meteor we inferred that the bolide overflowed Spain. Its initial altitude was  $H_b = 126.6 \pm 0.5$  km near the

<sup>11</sup> <https://youtu.be/XHIPdXjbNvY>

<sup>12</sup> [https://youtu.be/ce\\_7i6AMMnl](https://youtu.be/ce_7i6AMMnl)

zenith of the location of Orea (province of Guadalajara). The fireball penetrated the atmosphere till a final height  $H_e = 69.0 \pm 0.5$  km near from the zenith of the location of Peñalen (province of Guadalajara). The apparent radiant was located at the equatorial coordinates  $\alpha = 219.61^\circ$ ,  $\delta = +16.65^\circ$ . Besides, we obtained that the meteoroid entered the atmosphere with a velocity  $v_\infty = 64.9 \pm 0.5$  km/s. *Figure 15* shows the projection on the ground and the path in the atmosphere of the event.



*Figure 14* – Stacked image of the SWEMN20220119\_041103 “Orea” event as recorded from Calar Alto.

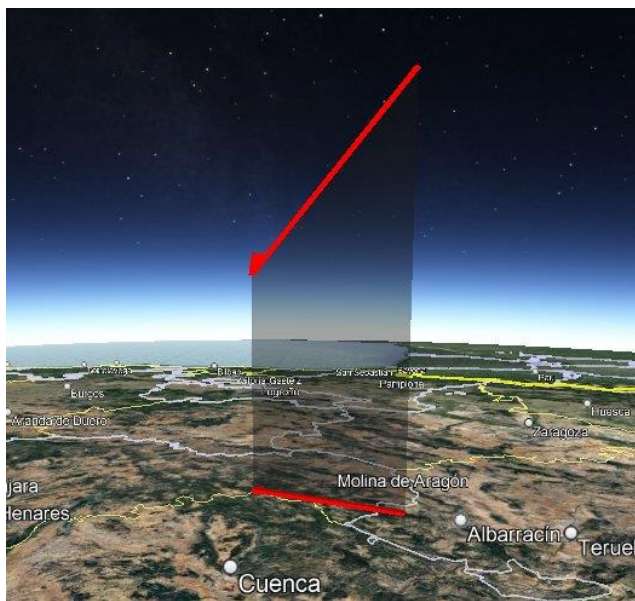


*Figure 15* – Atmospheric path and projection on the ground of the trajectory of the SWEMN20220119\_041103 meteor.

We named this bright meteor “Orea”, because the fireball passed near the zenith of this locality during its initial phase. The parameters of the orbit of the progenitor meteoroid before its encounter with our planet are included in *Table 5*, and the geocentric velocity yields  $v_g = 63.2 \pm 0.5$  km/s. By taking into account this orbit and the radiant position, we concluded that the fireball was generated by the 12 Bootids (IAU meteor shower code TBO#0607). The value calculated for the Tisserand parameter with respect to Jupiter ( $T_J = 0.21$ ) indicates that the meteoroid was moving on a cometary orbit before striking the atmosphere. This

orbit in the Solar System is drawn in *Figure 16* (Segon et al., 2014).

*Table 5* – Orbital data (J2000) of the progenitor meteoroid before its encounter with our planet.

$a$ (AU)	$5.6 \pm 1.3$	$\omega$ ( $^\circ$ )	$173.2 \pm 00.4$
$e$	$0.82 \pm 0.04$	$\Omega$ ( $^\circ$ )	$298.752428 \pm 10^{-5}$
$q$ (AU)	$0.9808 \pm 0.0003$	$i$ ( $^\circ$ )	$127.6 \pm 0.2$

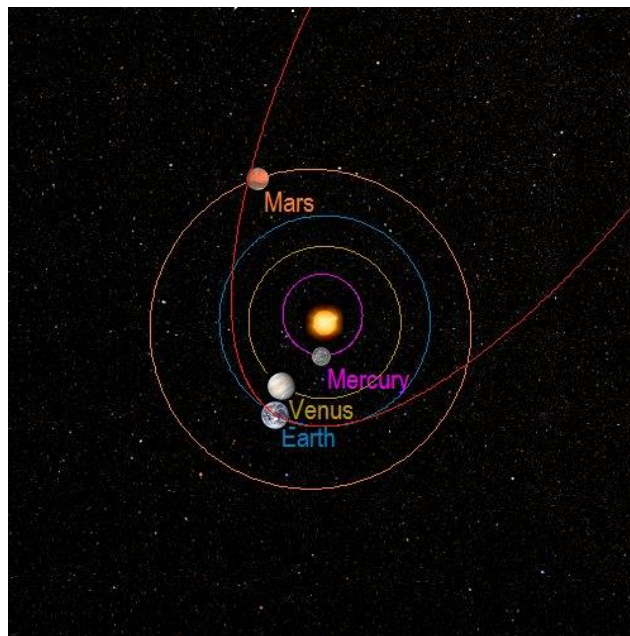


*Figure 16* – Projection on the ecliptic plane of the orbit of the SWEMN20220119\_041103 “Orea” fireball.

## 9 The 2022 February 11 fireball



*Figure 17* – Stacked image of the SWEMN20220211\_022400 “Daimiel” event as recorded from Madrid (Universidad Complutense).

On 2022 February 11, at  $2^{\text{h}}24^{\text{m}}00 \pm 0.1^{\text{s}}$  UT, our cameras recorded this bright event (*Figure 17*). The peak luminosity of the bright meteor was equivalent to an absolute magnitude of  $-10.0 \pm 1.0$ . The event was listed in the SWEMN meteor database with the code

SWEMN20220211\_022400. A video containing images of the bolide and its atmospheric trajectory was uploaded to YouTube<sup>13</sup>.

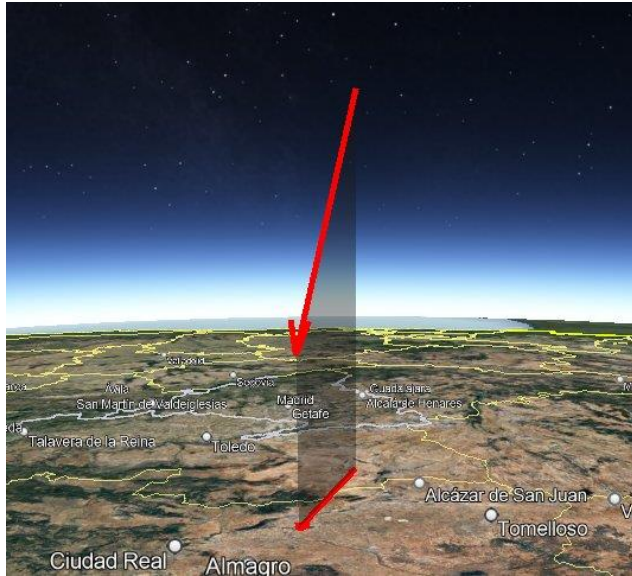


Figure 18 – Atmospheric path and projection on the ground of the trajectory of the SWEMN20220211\_022400 bolide.

#### Atmospheric path, radiant and orbit

The bolide overflowed the center of Spain. Its initial altitude was  $H_b = 114.5 \pm 0.5$  km, near the vertical of the locality of Villacañas (province of Toledo). The fireball penetrated the atmosphere till a final height  $H_e = 45.8 \pm 0.5$  km, near the zenith of the locality of Daimiel (province of Ciudad Real). The equatorial coordinates inferred for the apparent radiant are  $\alpha = 210.67^\circ$ ,  $\delta = +72.60^\circ$ . The entry velocity in the atmosphere found for the parent meteoroid was  $v_\infty = 24.2 \pm 0.3$  km/s. Figure 18 shows the luminous path of the event.

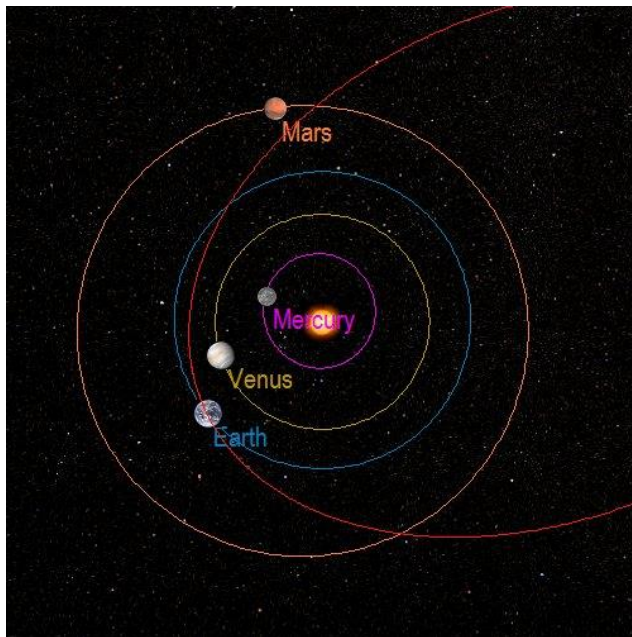


Figure 19 – Projection on the ecliptic plane of the orbit of the SWEMN20220211\_022400 “Daimiel” meteor.

Table 6 – Orbital data (J2000) of the progenitor meteoroid before its encounter with our planet.

$a$ (AU)	$2.5 \pm 0.1$	$\omega$ ( $^\circ$ )	$206.52 \pm 00.04$
$e$	$0.63 \pm 0.01$	$\Omega$ ( $^\circ$ )	$322.034733 \pm 10^{-5}$
$q$ (AU)	$0.9466 \pm 0.0004$	$i$ ( $^\circ$ )	$32.5 \pm 0.3$

The fireball was named “Daimiel”, because the bright meteor was located near the zenith of this locality during its final phase. The orbital parameters of the progenitor meteoroid before its encounter with our planet have been can be found in Table 6, and the geocentric velocity yields  $v_g = 21.4 \pm 0.3$  km/s. These values and the derived radiant confirm that the bright meteor was produced by the sporadic background. The Tisserand parameter ( $T_J = 2.93$ ) led to the conclusion that before hitting our planet’s atmosphere the progenitor particle was moving on a cometary (Jupiter family comet, JFC) orbit. This orbit in the Solar System is shown in Figure 19.

## 10 The 2022 February 18 fireball

On 2022 February 18, at  $1^{\text{h}}02^{\text{m}}47 \pm 0.1^{\text{s}}$  UT, the systems operated by the SWEMN network spotted this remarkable bright meteor (Figure 20). The fireball had a peak absolute magnitude of  $-13.0 \pm 1.0$ . It was included in our meteor database with the code SWEMN20220218\_010247. A video about this fireball was uploaded to YouTube<sup>14</sup>.



Figure 20 – Stacked image of the SWEMN20220218\_010247 “Torremocha” bolide as recorded from Calar Alto.

#### Atmospheric path, radiant and orbit

The calculation of the atmospheric trajectory of the bright meteor allowed to deduce that the fireball overflowed Spain. The initial altitude of the meteor yields  $H_b = 91.6 \pm 0.5$  km over the locality of Torremocha (province of Cáceres). It ended at a height  $H_e = 24.4 \pm 0.5$  km near the zenith of the locality of Aldea de Trujillo (province of Cáceres). From the analysis of the atmospheric path we also found that the apparent radiant was located at the position  $\alpha = 144.02^\circ$ ,  $\delta = +15.93^\circ$ . The entry velocity in the atmosphere obtained

<sup>13</sup> <https://youtu.be/vMqcf9N8WvE>

<sup>14</sup> <https://youtu.be/SafR6jgGfXI>

for the parent meteoroid was  $v_{\infty} = 20.7 \pm 0.3$  km/s. *Figure 21* shows the trajectory of the bolide in our atmosphere.

*Table 7* – Orbital data (J2000) of the progenitor meteoroid before its encounter with our planet.

$a$ (AU)	$2.22 \pm 0.08$	$\omega$ (°)	$69.7 \pm 00.1$
$e$	$0.67 \pm 0.01$	$\Omega$ (°)	$148.939624 \pm 10^{-5}$
$q$ (AU)	$0.729 \pm 0.004$	$i$ (°)	$0.79 \pm 0.03$

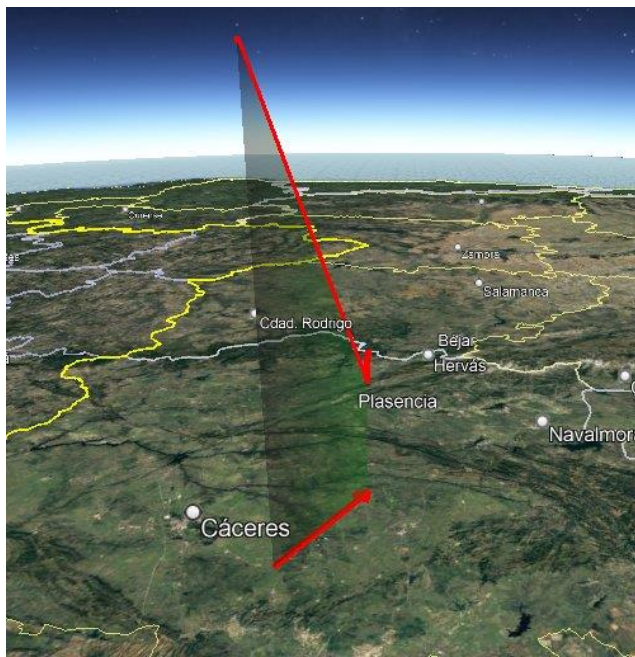


*Figure 21* – Atmospheric path and projection on the ground of the trajectory of the SWEMN20220218\_010247 “Torremocha” event.

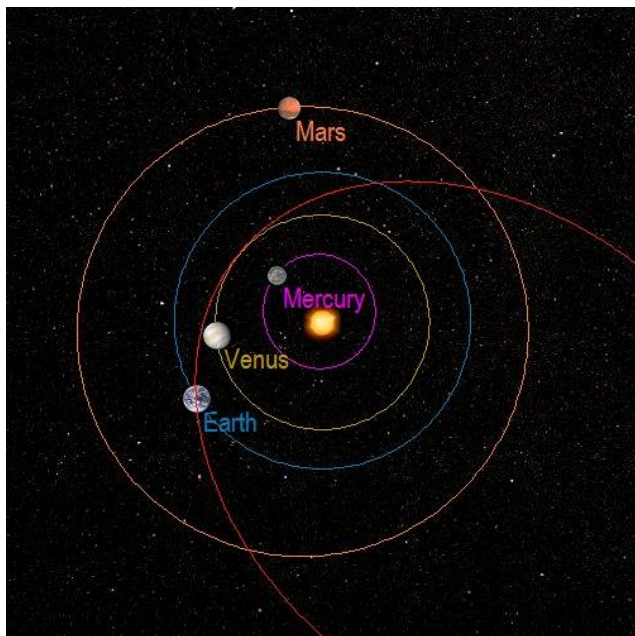


*Figure 22* – Projection on the ecliptic plane of the orbit of the SWEMN20220218\_010247 “Torremocha” fireball.

We named this bolide “Torremocha”, because the fireball overflowed this locality during its initial phase. The orbital parameters of the parent meteoroid before its encounter with our planet are listed in *Table 7*. The value calculated for the geocentric velocity was  $v_g = 17.6 \pm 0.3$  km/s. By

taking into account this orbit and the radiant position, we inferred that the bright meteor was generated by a meteoroid associated with the sporadic component. The Tisserand parameter with respect to Jupiter yields  $T_J = 3.31$ , which means that before striking the atmosphere the meteoroid was moving on an asteroidal orbit. This orbit is drawn in *Figure 22*.

## 11 Conclusions

We have focused in this work on the description of an innovative tool that employs artificial intelligence (AI) techniques to generate scientific contributions from the information stored in the SWEMN digital database. This AI was named AIMEE (Artificial Intelligence with Meteoroid Environment Expertise). AIMEE has been employed in this work to automatically generate a report about a series of events recorded in the framework of the SWEMN network and the SMART project. In this way, we have also presented here some of the brightest fireballs recorded by our meteor-observing stations from January to February 2022. Their peak absolute brightness ranges from mag.  $-10$  to mag.  $-13$ . The text below, which summarizes the main conclusions derived from the analysis of these bolides, was written by AIMEE.

The “Santa Margarida” fireball was recorded on January 2. This sigma Hydrid (HYD#0016) meteor event had a peak absolute magnitude of  $-12.0$  and overflowed Portugal. The meteoroid followed a cometary orbit before hitting the Earth’s atmosphere.

The second bright meteor discussed here was the “Montecorto” fireball. This was recorded on January 9. The peak magnitude of this alpha Hydrid (AHY#0331), which overflowed the south of Spain, was  $-13.0$ . Before striking our planet’s atmosphere the meteoroid was moving on a cometary orbit. The final height of this deep-penetrating meteor was of about 31 km.

The third fireball was the “Ventillas” bolide. This was recorded on January 14. It was associated with the sporadic background, its peak magnitude was  $-12.0$ , and overflowed the south of Spain. The meteoroid was moving on an asteroidal orbit before striking our planet’s atmosphere. At the final stage of its luminous phase this deep-penetrating bolide was located at a height of about 23 km. Since the analysis of the final stage revealed a non-zero mass, this meteor was considered as a potential meteorite-dropper. The emission spectrum of the bolide was also registered and analyzed. This exhibits the lines from Na I-1 (588.9 nm), Mg I-2 (516.7 nm), Fe I-4 (385.6 nm), Fe I-41 (441.5 nm), Fe I-42, Fe I-43 (414.3 nm), Fe I-15 (526.9 nm), and Fe I-318.

The next fireball analyzed here was a bolide recorded on January 18. Its peak magnitude was  $-11.0$ . The meteor was produced by a sporadic meteoroid and overflowed the Mediterranean Sea. Before impacting our atmosphere, this meteoroid was moving on an asteroidal orbit. The ending height of this deep-penetrating fireball was of about 29 km.

The fifth bright meteor presented in this report was a fireball recorded on January 19 that was named “Orea”. Its peak magnitude was  $-11.0$ . The fireball was produced by a 12 Bootid (TBO#0607) meteoroid and overflowed Spain. This meteoroid was moving on a cometary orbit before striking our atmosphere.

The next event was the “Daimiel” bright meteor. This was recorded on February 11 and its peak absolute magnitude was  $-10.0$ . The meteor event was produced by a sporadic meteoroid and overflowed Spain. This meteoroid was moving on a cometary (JFC) orbit before entering the atmosphere. This deep-penetrating meteor reached a final altitude of about 45 km.

And the last event presented in this paper was the “Torremocha” bolide, that was recorded on February 18. It was also associated with the sporadic background. Its peak magnitude was  $-13.0$  and overflowed Spain. Before colliding with the atmosphere, the meteoroid was moving on an asteroidal orbit. This deep-penetrating meteor reached a terminal height of about 24 km.

## Acknowledgment

We acknowledge support from the Spanish Ministry of Science and Innovation (project PID2019-105797GB-I00). We also acknowledge financial support from the State Agency for Research of the Spanish MCIU through the “Center of Excellence Severo Ochoa” award to the Instituto de Astrofísica de Andalucía (SEV-2017-0709). P.S.-S. acknowledges financial support by the Spanish grant AYA - RTI2018 - 098657 - J - I00 “LEO - SBNAF” (MCIU / AEI / FEDER, UE). The first author is very grateful to Casa das Ciencias (Museos Científicos Coruñeses) for their helpful support in the setup and operation of the automated meteor-observing station located at their facilities in A Coruña.

## References

- Cepplecha Z. (1987). “Geometric, dynamic, orbital and photometric data on meteoroids from photographic fireball networks”. *Bull. Astron. Inst. Cz.*, **38**, 222–234.
- Jenniskens P., Nénon Q., Albers J., Gural P. S., Haberman B., Holman D., Morales R., Grigsby B. J., Samuels D. and Johannink C. (2016). “The established meteor showers as observed by CAMS”. *Icarus*, **266**, 331–354.
- Madiedo J. M. (2014). “Robotic systems for the determination of the composition of solar system materials by means of fireball spectroscopy”. *Earth, Planets & Space*, **66**, 70.
- Madiedo J. M., Ortiz J. L., Organero F., Ana-Hernández L., Fonseca F., Morales N. and Cabrera-Caño J. (2015a). “Analysis of Moon impact flashes detected during the 2012 and 2013 Perseids”. *A&A*, **577**, A118.
- Madiedo J. M., Ortiz J. L., Morales N. and Cabrera-Caño J. (2015b). “MIDAS: Software for the detection and analysis of lunar impact flashes”. *Planetary and Space Science*, **111**, 105–115.
- Madiedo J. M. (2017). “Automated systems for the analysis of meteor spectra: The SMART Project”. *Planetary and Space Science*, **143**, 238–244.
- Madiedo J. M., Ortiz J. L., Izquierdo J., Santos-Sanz P., Aceituno J., de Guindos E., Yanguas P., Palacian J., San Segundo A., and Avila D. (2021). “The Southwestern Europe Meteor Network: recent advances and analysis of bright fireballs recorded along April 2021”. *eMetN*, **6**, 397–406.
- Madiedo J. M., Ortiz J. L., Izquierdo J., Santos-Sanz P., Aceituno J., de Guindos E., Yanguas P., Palacian J., San Segundo A., and Avila D. (2022). “The Southwestern Europe Meteor Network: new advances and analysis of bright fireballs recorded from September to December 2021”. *eMetN*, **7**, 113–122.
- Ortiz J. L., Madiedo J. M., Morales N., Santos-Sanz P. and Aceituno F. J. (2015). “Lunar impact flashes from Geminids: analysis of luminous efficiencies and the flux of large meteoroids on Earth”. *Monthly Notices of the Royal Astronomical Society*, **454**, 344–352.
- Segon D., Andreic Z., Gural P., Skokic I., Korlevic K., Vida D., Novoselnik F. and Gostinski D. (2014). “Results of CMN 2013 search for new showers across CMN and SonotaCo databases III”. *WGN, Journal of the International Meteor Organization*, **42**, 227–233.

# February 2022 report CAMS BeNeLux

Carl Johannink

Am Ollenkamp 4, 48599 Gronau, Germany

c.johannink@t-online.de

A summary of the activity of the CAMS BeNeLux network during the month of February 2022 is presented. This month was good for a total of 5770 multi-station meteors resulting in 1939 orbits. Most of them were collected during the last ten days of this month.

## 1 Introduction

Meteor activity in February is nearly at the lowest level for northern latitudes. After a poor month of January, we hoped for some improvement this month.

## 2 February 2022 statistics

In February the gloomy weather continued until February 20 for most of our stations. Mean temperatures were again fairly high, due to lack of clear skies during the night. Once more the northern stations were hampered by long periods of overcast skies, where the more southern stations could at least get some results like on February 7–9, and February 16, 18 and 19.

So, the effect that the active more northern stations got less results than the stations in the southern parts of the BeNeLux was maintained during the first twenty nights of this month. During five February nights, all during the first two third of this month, we couldn't collect any data at all.

The last week however weather improved significantly, culminating in complete clear and transparent nights towards the end of the month.

CAMS-BeNeLux collected 5770 multi-station meteors this month, resulting in a total of 1939 orbits, 1154 of them in the last 8 nights, or nearly 60% of the total amount of orbits this month.

The number of orbits derived from more than two stations remained at the low level of approximately 60% during the first three weeks. As a result of the clear and transparent last period of February, this percentage increased to nearly 70% then.

On average 63.7 cameras were active during the nights this month. This number is lower than last year, because for different reasons some stations were only partly operational or not at all active this month. Prospects are good however that stations at Burlage, Gent, Zoersel and Alphen will deliver results again in the near future. In Humain a new camera was added to the network, delivering results since 8 February. Some more new cameras will be added to our network in the coming weeks.

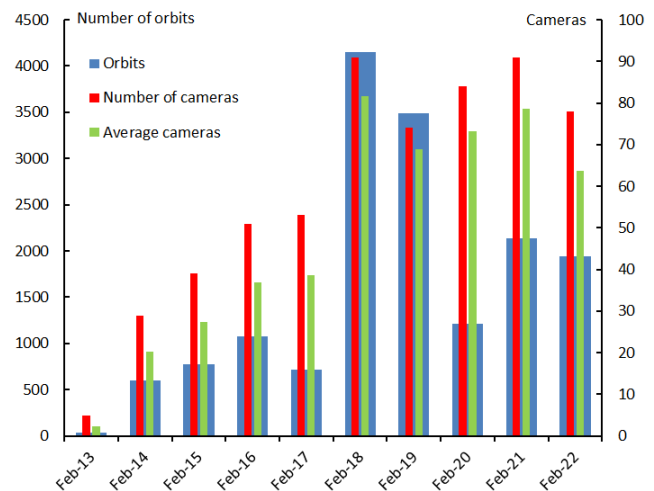


Figure 1 – Comparing February 2022 to previous months of February in the CAMS BeNeLux history. The blue bars represent the number of orbits, the red bars the maximum number of cameras running in a single night and the green bars the average number of cameras running per night.

Table 1 – February 2022 compared to previous months of February.

Year	Nights	Orbits	Stations	Max. Cams	Min. Cams	Avg. Cams
2013	9	38	6	5	–	2.3
2014	21	601	12	29	–	20.3
2015	21	777	14	39	–	27.4
2016	24	1075	17	51	13	36.9
2017	16	717	18	53	20	38.6
2018	26	4147	22	91	48	81.7
2019	24	3485	18	74	50	68.8
2020	24	1215	22	84	62	73.1
2021	25	2136	26	91	60	78.6
2022	23	1939	24	78	49	63.7
Total	213	16130				

## 3 Conclusion

The results for February 2022 are the fourth best during 10 years of CAMS BeNeLux.

## Acknowledgment

Many thanks to all participants in the CAMS-BeNeLux network for their dedicated efforts. The CAMS-BeNeLux team was operated by the following volunteers during the month of February 2022:

*Hans Betlem* (Woold, CAMS 3071, 3072 and 3073), *Jean-Marie Biets* (Wilderen, Belgium, CAMS 379, 380, 381 and 382), *Ludger Boergerding* (Holdorf, Germany, RMS 3801), *Martin Breukers* (Hengelo, Netherlands, CAMS 320, 321, 322, 323, 324, 325, 326 and 327, RMS 319, 328 and 329), *Seppe Canonaco* (Genk, RMS 3818, RMS 3819), *Pierre de Ponthiere* (Lesve, Belgium, RMS 3816), *Tammo Jan Dijkema* (Dwingeloo, Netherlands, RMS 3199), *Isabelle Ansseau*, *Jean-Paul Dumoulin*, *Dominique Guiot* and *Christian Walin* (Grapfontaine, Belgium, CAMS 814 and 815, RMS 3814, RMS 3817), *Uwe Glässner* (Langenfeld, Germany, RMS 3800), *Luc Gobin* (Mechelen, Belgium, CAMS 3890, 3891, 3892 and 3893), *Tioga Gulon* (Nancy,

France, CAMS 3900 and 3901), *Robert Haas* (Alphen aan de Rijn, Netherlands, CAMS 3160, 3161, 3162, 3163, 3164, 3165, 3166 and 3167), *Robert Haas* (Texel, Netherlands, CAMS 811, 812 and 813), *Kees Habraken* (Kattendijke, Netherlands, RMS 378), *Klaas Jobse* (Oostkapelle, Netherlands, CAMS 3030, 3031, 3032, 3033, 3034, 3035, 3036 and 3037), *Carl Johannink* (Gronau, Germany, CAMS 3100, 3101 and 3102), *Reinhard Kühn* (Flatzby, Germany, RMS 3802), *Hervé Lamy* (Dourbes, Belgium, CAMS 394 and 395), *Hervé Lamy* (Humain Belgium, CAMS 816, RMS 3821), *Hervé Lamy* (Ukkel, Belgium, CAMS 393), *Koen Miskotte* (Ermelo, Netherlands, CAMS 3051, 3052, 3053 and 3054), *Tim Polfliet* (Gent, Belgium, CAMS 396, RMS 3820), *Steve Rau* (Zillebeke, Belgium, CAMS 3850, 3852, RMS 3851, RMS 3853), *Paul and Adriana Roggemans* (Mechelen, Belgium, RMS 3830 and 3831, CAMS 3832, 3833, 3834, 3835, 3836 and 3837), *Hans Schremmer* (Niederkruechten, Germany, CAMS 803).

# March 2022 report CAMS BeNeLux

Carl Johannink

Am Ollenkamp 4, 48599 Gronau, Germany

c.johannink@t-online.de

A summary of the activity of the CAMS BeNeLux network during the month of March 2022 is presented. This month was good for a total of 10436 multi-station meteors resulting in 3189 orbits, a record number for March.

## 1 Introduction

Meteor activity in March is now reaching the lowest level for northern latitudes. The sunny weather at the end of February continued throughout March, resulting in a record number of orbits.

## 2 March 2022 statistics

When we look at the mean temperatures, March shows a peculiar pattern. The whole month was nearly one degree warmer than normal. But there was a striking difference between mean temperatures during daytime and nighttime. Maximum temperatures were nearly 3 degrees higher than normal, on the opposite, minimum temperatures were more than 1 degree below normal. That could mean only two things: a lot of sunshine at daytime, and a lot of clear skies at night.

In fact, the BeNeLux had a record month of March for sunshine. Approximately 255 hours of sunshine is more than 20% higher than the sunniest March between 1901 and 2021. This month would even get a top-10 ranking for sunshine in June, July or August, what emphasizes the unique situation in March 2022.

As a result, only 2 nights remained without any orbit this month. CAMS BeNeLux collected 10436 multi-station meteors this month, resulting in a total of 3189 orbits.

The number of orbits derived from more than two stations was, due to the clear weather at a fairly high level of approximately 73.1%. On average 70.6 cameras were active during the nights this month. This number is lower than last year (78.9), because for different reasons some stations were only partly active or not active at all this month.

The station at Ermelo suffered irreparable hardware problems at the end of March. Prospects are good however that this station as well as the stations at Burlage and Zoersel will again deliver results in the near future. Fortunately, the station at Gent is active again since early April.

Some more new cameras will be added to our network next month.

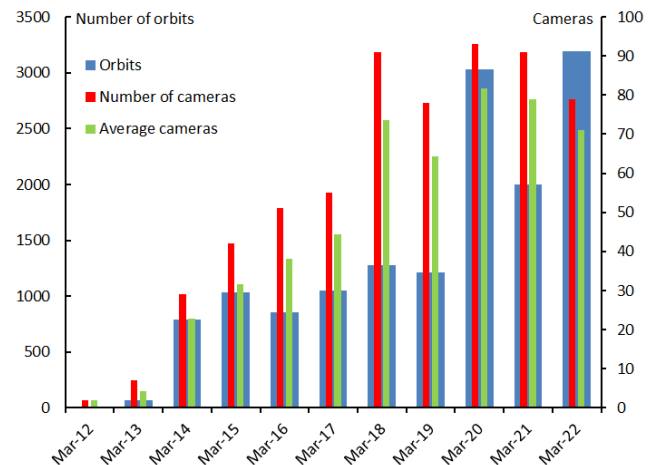


Figure 1 – Comparing March 2022 to previous months of February in the CAMS BeNeLux history. The blue bars represent the number of orbits, the red bars the maximum number of cameras running in a single night and the green bars the average number of cameras running per night.

Table 1 – March 2022 compared to previous months of March.

Year	Nights	Orbits	Stations	Max. Cams	Min. Cams	Mean Cams
2012	2	12	2	2	–	2.0
2013	10	69	6	7	–	4.2
2014	24	793	12	29	–	22.8
2015	23	1033	14	42	–	31.7
2016	23	856	16	51	12	38.2
2017	26	1048	19	55	20	44.4
2018	25	1280	22	91	53	73.5
2019	29	1215	20	78	54	64.4
2020	27	3026	25	93	66	81.7
2021	28	1998	27	91	59	78.9
2022	29	3189	24	79	58	70.6
Total	246	14519				

## 3 Conclusion

The results for March 2022 are the best during 11 years of CAMS BeNeLux.

## Acknowledgment

Many thanks to all participants in the CAMS-BeNeLux network for their dedicated efforts. The CAMS-BeNeLux team was operated by the following volunteers during the month of March 2022:

*Hans Betlem* (Woold, CAMS 3071, 3072 and 3073), *Jean-Marie Biets* (Wilderden, Belgium, CAMS 379, 380, 381 and 382), *Ludger Boergerding* (Holdorf, Germany, RMS 3801), *Martin Breukers* (Hengelo, Netherlands, CAMS 320, 321, 322, 323, 324, 325, 326 and 327, RMS 319, 328 and 329), *Giuseppe Canonaco* (Genk, RMS 3818, RMS 3819), *Pierre de Ponthiere* (Lesve, Belgium, RMS 3816 and 3826), *Bart Dessoy* (Zoersel, Belgium, CAMS 397, 398, 804, 805 and 806), *Tammo Jan Dijkema* (Dwingeloo, Netherlands, RMS 3199), *Isabelle Anseau*, *Jean-Paul Dumoulin*, *Dominique Guiot and Christian Walin* (Grapfontaine, Belgium, CAMS 814 and 815, RMS 3814, RMS 3817), *Uwe Glässner* (Langenfeld, Germany, RMS 3800), *Luc Gobin* (Mechelen,

Belgium, CAMS 3890, 3891, 3892 and 3893), *Tioga Gulon* (Nancy, France, CAMS 3900 and 3901), *Robert Haas* (Alphen aan de Rijn, Netherlands, CAMS 3160, 3161, 3162, 3163, 3164, 3165, 3166 and 3167), *Robert Haas* (Texel, Netherlands, CAMS 811, 812), *Kees Habraken* (Kattendijke, Netherlands, RMS 378), *Klaas Jobse* (Oostkapelle, Netherlands, CAMS 3030, 3031, 3032, 3033, 3034, 3035, 3036 and 3037), *Carl Johannink* (Gronau, Germany, CAMS 3100, 3101, 3102, 3103 and 3104), *Reinhard Kühn* (Flatzby, Germany, RMS 3802), *Hervé Lamy* (Dourbes, Belgium, CAMS 394 and 395, RMS 3825), *Hervé Lamy* (Humain Belgium, CAMS 816, RMS 3821), *Hervé Lamy* (Ukkel, Belgium, CAMS 393), *Koen Miskotte* (Ermelo, Netherlands, CAMS 3051, 3052, 3053 and 3054), *Tim Polfliet* (Gent, Belgium, CAMS 396, RMS 3820), *Steve Rau* (Zillebeke, Belgium, CAMS 3850, 3852, RMS 3851, RMS 3853), *Paul and Adriana Roggemans* (Mechelen, Belgium, RMS 3830 and 3831, CAMS 3832, 3833, 3834, 3835, 3836 and 3837), *Hans Schremmer* (Niederkruechten, Germany, CAMS 803).

# Radio meteors February 2022

Felix Verbelen

Vereniging voor Sterrenkunde & Volkssterrenwacht MIRA, Grimbergen, Belgium

felix.verbelen@skynet.be

An overview of the radio observations during February 2022 is given.

## 1 Introduction

The graphs show both the daily totals (*Figure 1 and 2*) and the hourly numbers (*Figure 3 and 4*) of “all” reflections counted automatically, and of manually counted “overdense” reflections, overdense reflections longer than 10 seconds and longer than 1 minute, as observed here at Kampenhout (BE) on the frequency of our VVS-beacon (49.99 MHz) during the month of February 2022.

The hourly numbers, for echoes shorter than 1 minute, are weighted averages derived from:

$$N(h) = \frac{n(h-1)}{4} + \frac{n(h)}{2} + \frac{n(h+1)}{4}$$

During this month local and unidentified noise and interference was moderate to high, and due to a variety of technical problems the counts from February 17<sup>th</sup> to 21<sup>st</sup> proved unreliable and were therefore left out, with the exception of a reflection longer than 1 minute on February 18<sup>th</sup>.

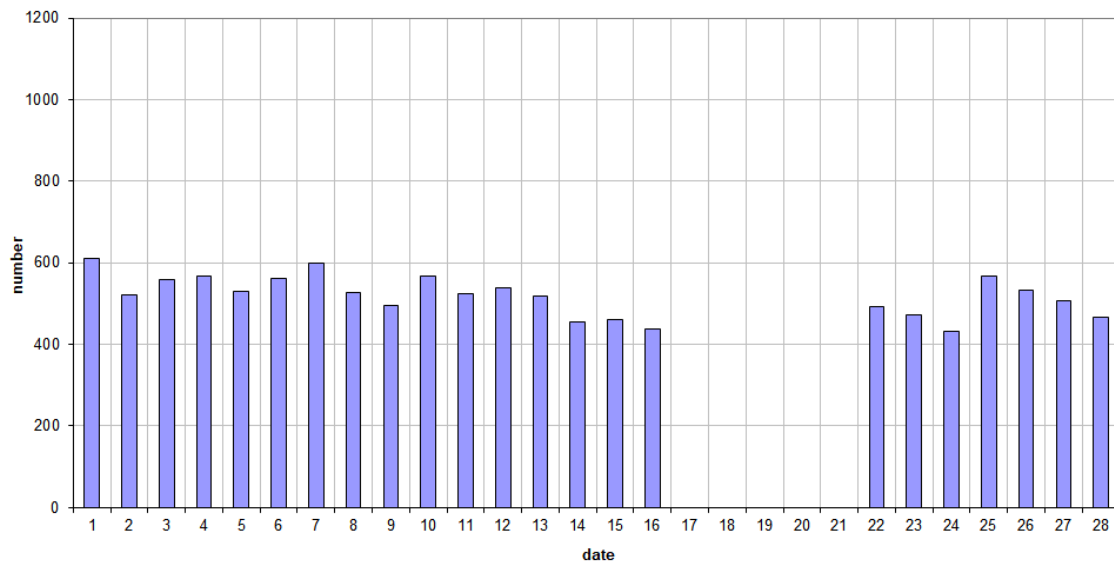
Weak to moderate lightning activity was recorded on 4 days.

In fact, there were no real highlights this month and as expected the general activity remained low. Only 2 reflections longer than 1 minute were observed here. SpecLab pictures of these, together with another interesting long reflection are shown in *Figures 5–7*. In addition to the usual graphs, you will also find the raw counts in cvs-format<sup>15</sup> from which the graphs are derived.

The table contains the following columns: day of the month, hour of the day, day + decimals, solar longitude (epoch J2000), counts of “all” reflections, overdense reflections, reflections longer than 10 seconds and reflections longer than 1 minute, the numbers being the observed reflections of the past hour.

<sup>15</sup> [https://www.meteornews.net/wp-content/uploads/2022/03/202202\\_49990\\_FV\\_rawcounts.csv](https://www.meteornews.net/wp-content/uploads/2022/03/202202_49990_FV_rawcounts.csv)

**49.99MHz - RadioMeteors February 2022**  
**daily totals of "all" reflections** (automatic count\_Mettel5\_7Hz)  
*Felix Verbelen (Kamphenout)*



**49.99MHz - RadioMeteors February 2022**  
**daily totals of all overdense reflections**  
*Felix Verbelen (Kamphenout)*

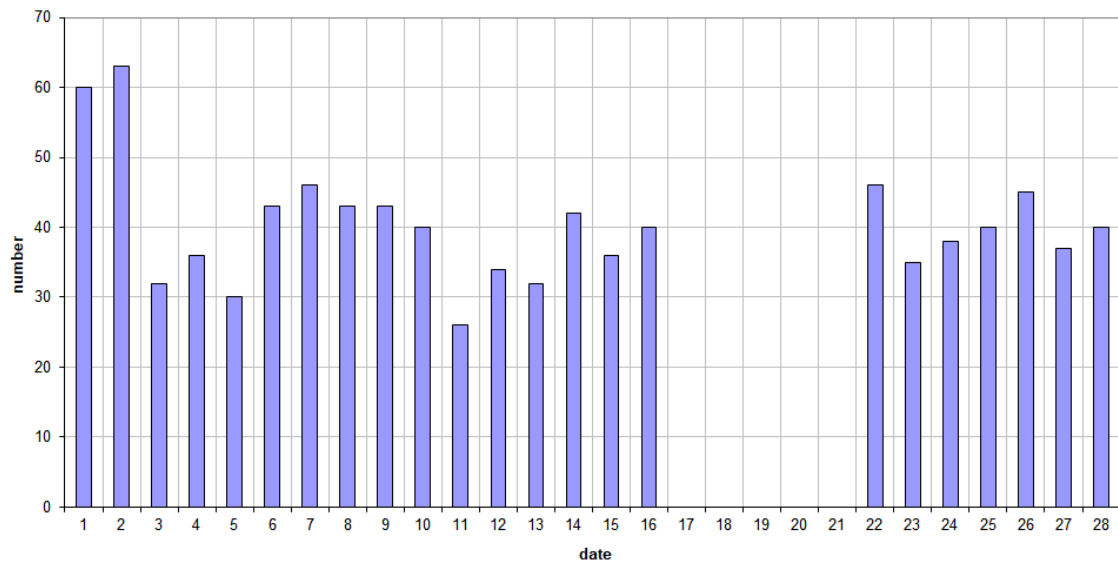
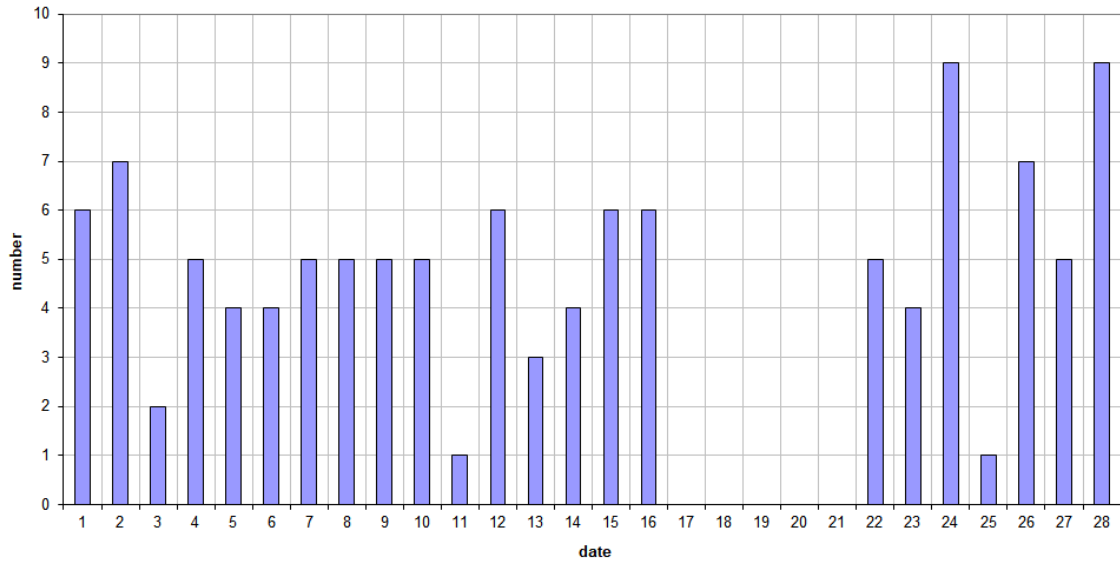


*Figure 1* – The daily totals of “all” reflections counted automatically, and of manually counted “overdense” reflections, as observed here at Kamphenout (BE) on the frequency of our VVS-beacon (49.99 MHz) during February 2022.

**49.99MHz - RadioMeteors February 2022**  
**daily totals of reflections longer than 10 seconds**  
*Felix Verbelen (Kamphenhout)*



**49.99MHz - RadioMeteors February 2022**  
**daily totals of reflections longer than 1 minute**  
*Felix Verbelen (Kamphenhout)*

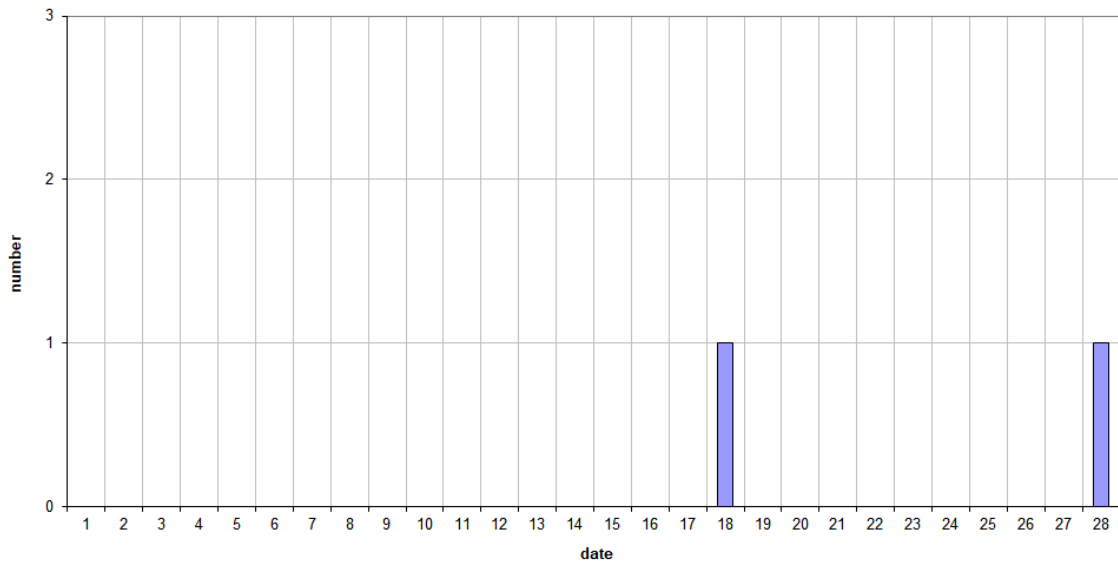
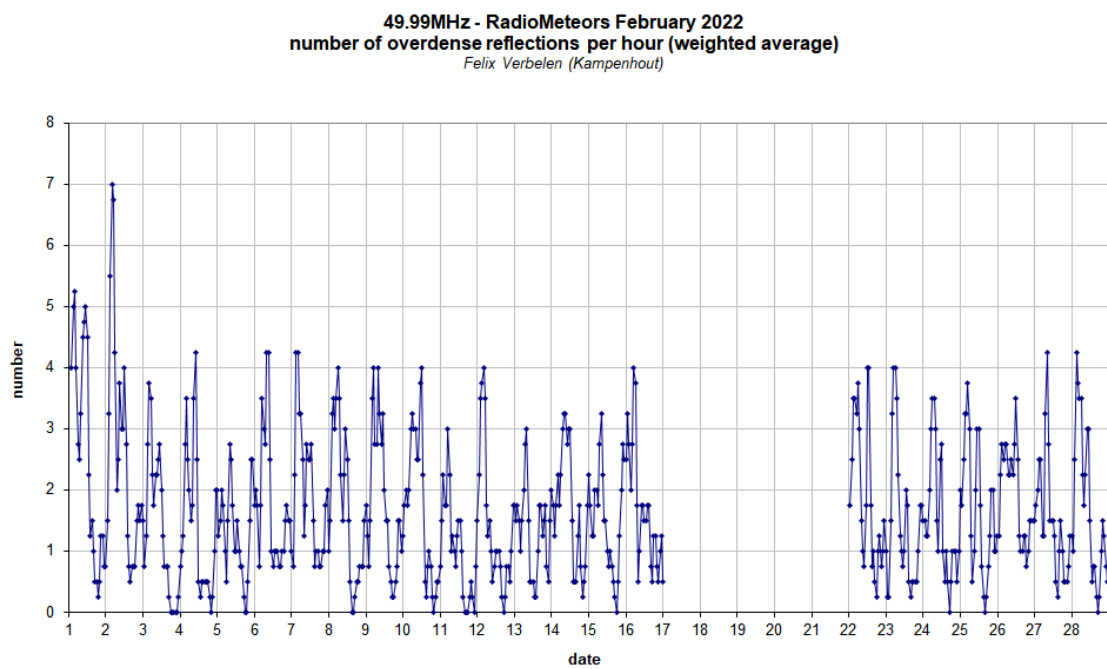
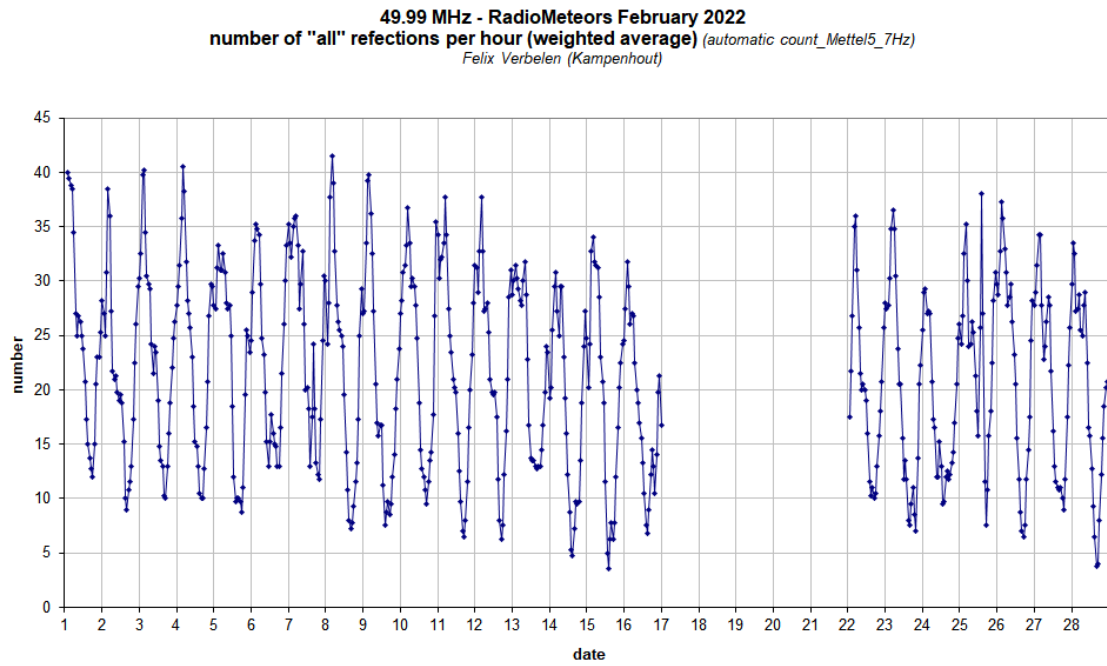
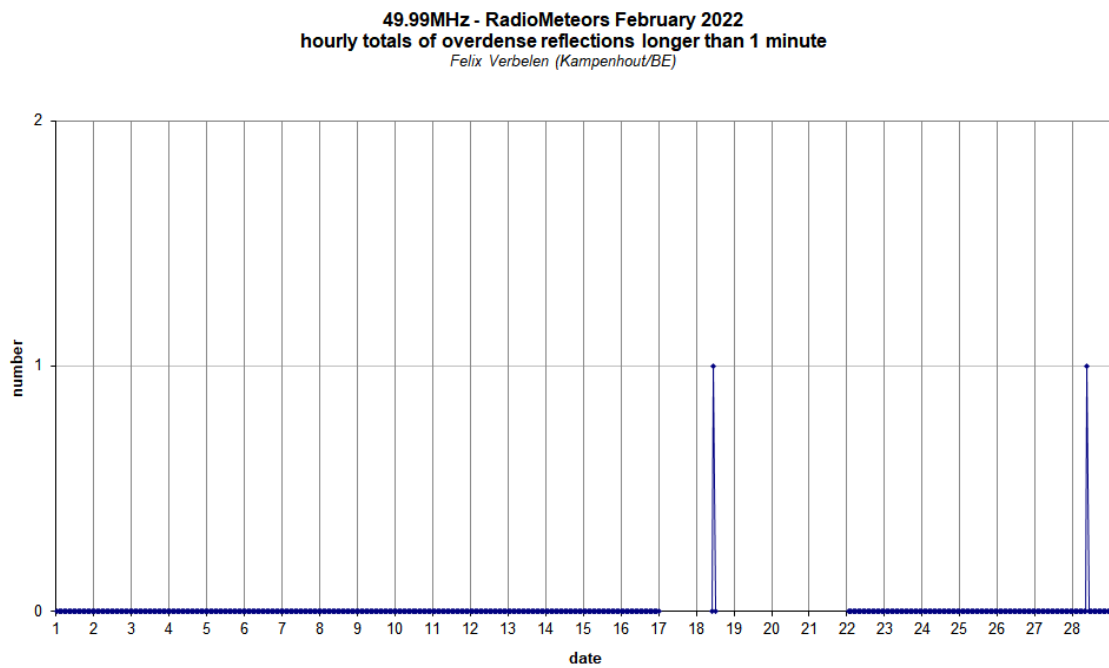
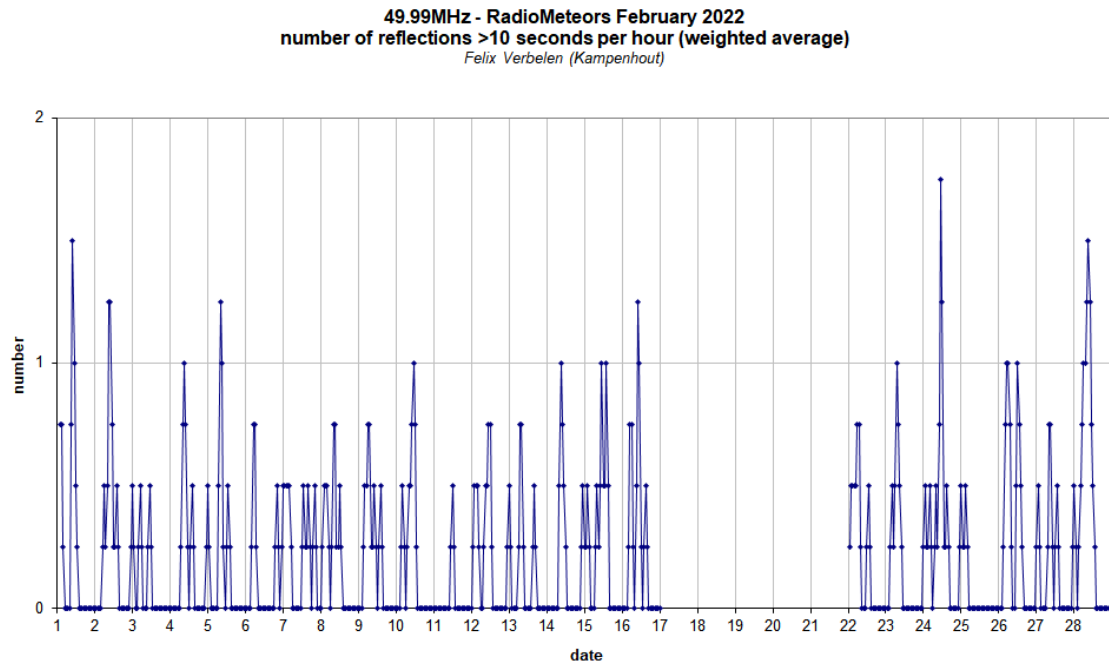


Figure 2 – The daily totals of overdense reflections longer than 10 seconds and longer than 1 minute, as observed here at Kamphenhout (BE) on the frequency of our VVS-beacon (49.99 MHz) during February 2022.



*Figure 3* – The hourly numbers of “all” reflections counted automatically, and of manually counted “overdense” reflections, as observed here at Kampenhout (BE) on the frequency of our VVS-beacon (49.99 MHz) during February 2022.



*Figure 4* – The hourly numbers of overdense reflections longer than 10 seconds and longer than 1 minute, as observed here at Kamphenhout (BE) on the frequency of our VVS-beacon (49.99 MHz) during February 2022.

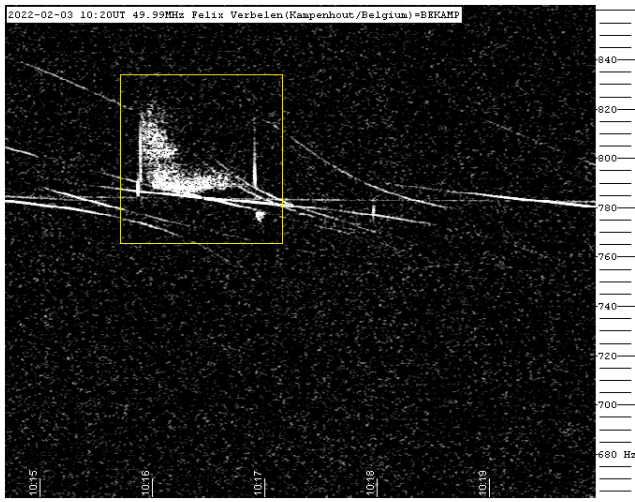


Figure 5 – Meteor reflection 3 February 2022, 10<sup>h</sup>20<sup>m</sup> UT.

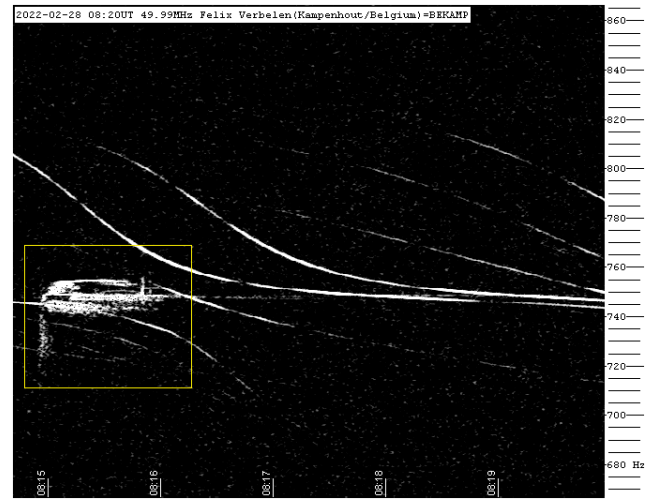


Figure 7 – Meteor reflection 28 February 2022, 08<sup>h</sup>20<sup>m</sup> UT.

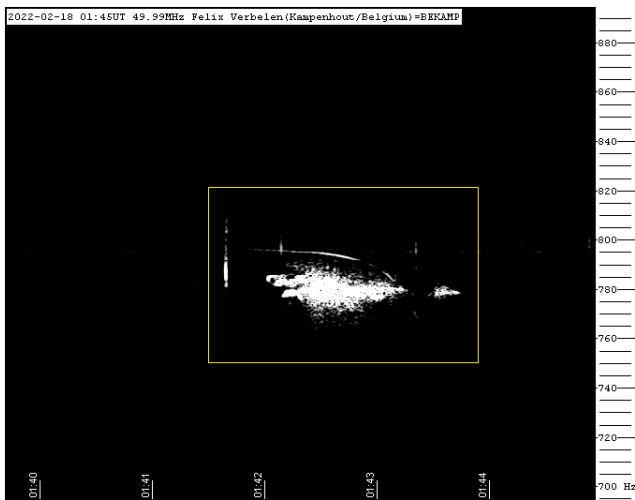


Figure 6 – Meteor reflection 18 February 2022, 01<sup>h</sup>45<sup>m</sup> UT.

# Radio meteors March 2022

Felix Verbelen

Vereniging voor Sterrenkunde & Volkssterrenwacht MIRA, Grimbergen, Belgium

felix.verbelen@skynet.be

An overview of the radio observations during March 2022 is given.

## 1 Introduction

The graphs show both the daily totals (*Figure 1 and 2*) and the hourly numbers (*Figure 3 and 4*) of “all” reflections counted automatically, and of manually counted “overdense” reflections, overdense reflections longer than 10 seconds and longer than 1 minute, as observed here at Kampenhout (BE) on the frequency of our VVS-beacon (49.99 MHz) during the month of March 2022.

The hourly numbers, for echoes shorter than 1 minute, are weighted averages derived from:

$$N(h) = \frac{n(h-1)}{4} + \frac{n(h)}{2} + \frac{n(h+1)}{4}$$

On 1 and 4 March there were interruptions due to maintenance work near our beacon, so data for those periods are missing.

Local interference and unidentified noise remained low for most of the month apart from sometimes strong noise

caused by solar eruptions (*Figure 5*), but this was of course interesting in itself.

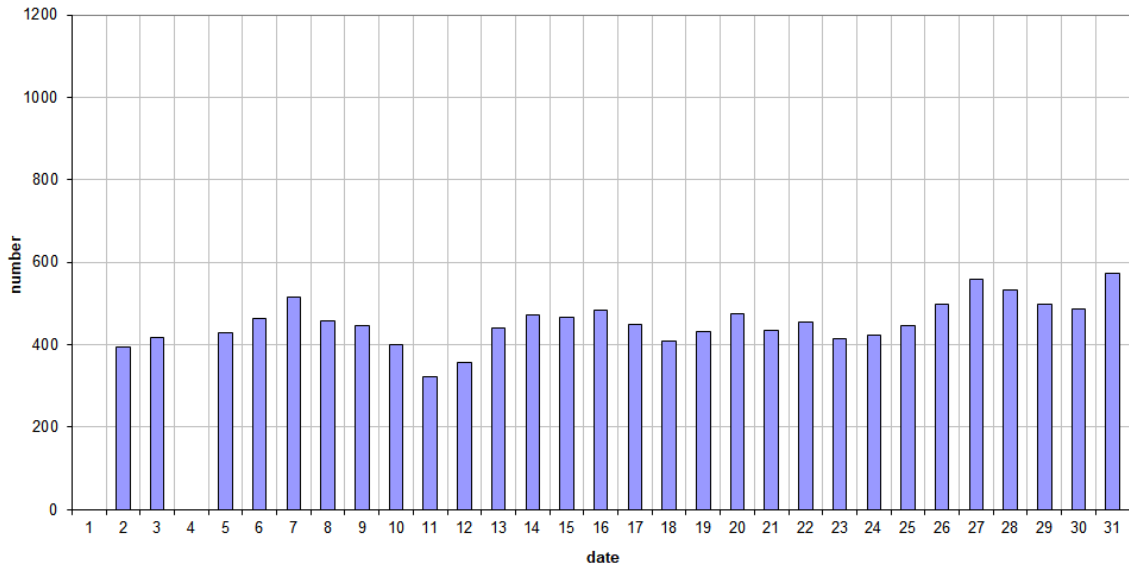
No lightning activity was recorded during this the month. As expected, overall shower activity remained low, with no real highlights, but there were some interesting minor showers such as the Zeta Cygnids on March 24<sup>th</sup>. In addition to the usual graphs, you will also find the raw counts in cvs-format<sup>16</sup> from which the graphs are derived.

Only 4 reflections lasting more than 1 minute were observed this month, 2 of which were rather faint. (*Figures 6 to 9*).

The table contains the following columns: day of the month, hour of the day, day + decimals, solar longitude (epoch J2000), counts of “all” reflections, overdense reflections, reflections longer than 10 seconds and reflections longer than 1 minute, the numbers being the observed reflections of the past hour.

<sup>16</sup>[https://www.meteornews.net/wp-content/uploads/2022/04/202203\\_49990\\_FV\\_rawcounts.csv](https://www.meteornews.net/wp-content/uploads/2022/04/202203_49990_FV_rawcounts.csv)

**49.99MHz - RadioMeteors March 2022**  
**daily totals of "all" reflections** (automatic count\_Mettel5\_7Hz)  
*Felix Verbelen (Kamphenhout)*



**49.99MHz - RadioMeteors March 2022**  
**daily totals of all overdense reflections**  
*Felix Verbelen (Kamphenhout)*

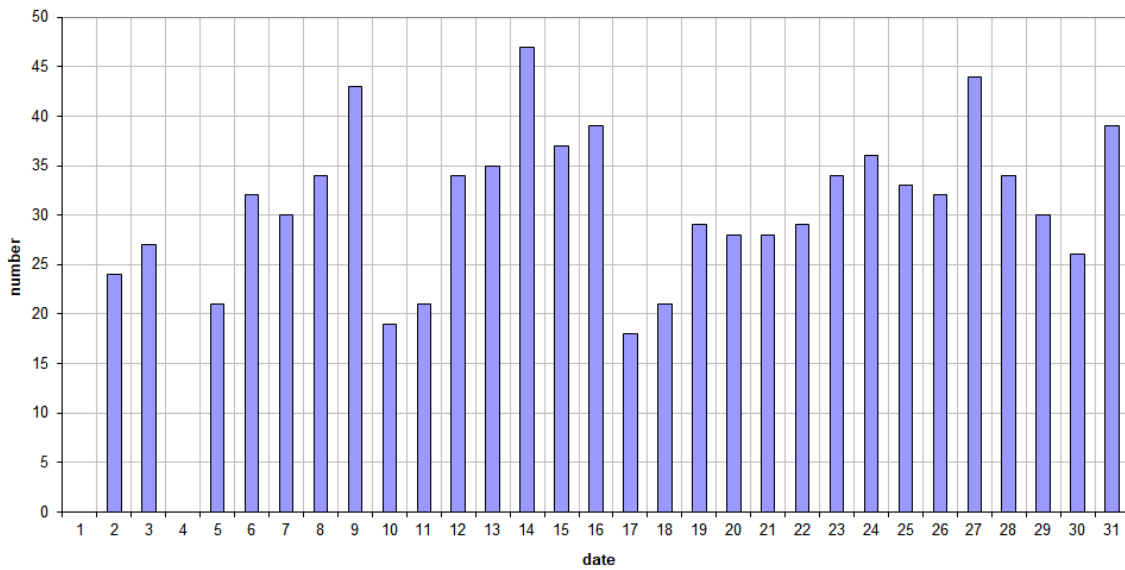
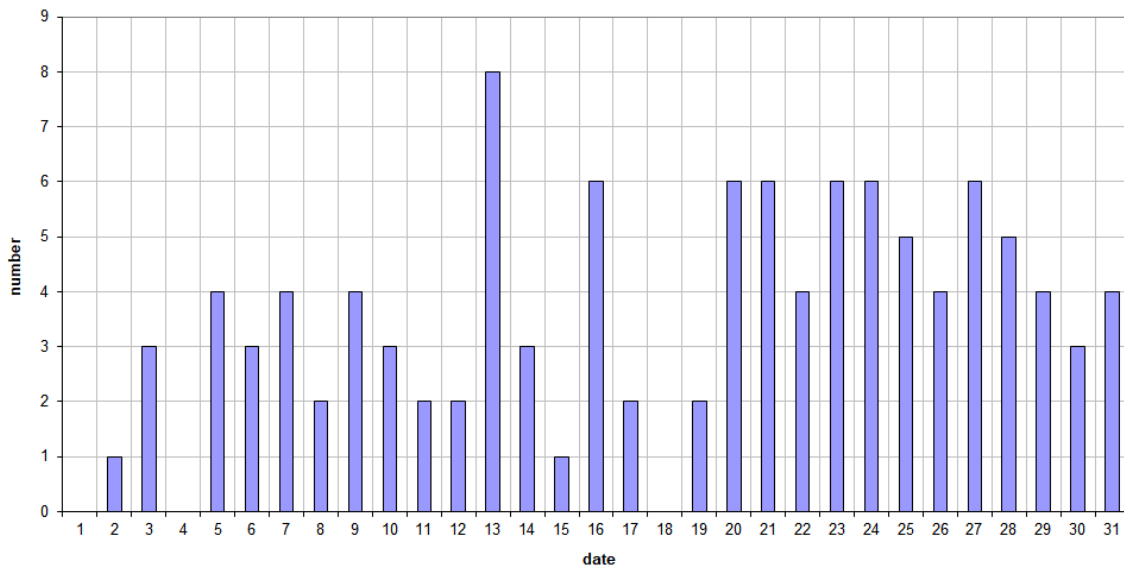


Figure 1 – The daily totals of “all” reflections counted automatically, and of manually counted “overdense” reflections, as observed here at Kamphenhout (BE) on the frequency of our VVS-beacon (49.99 MHz) during March 2022.

**49.99MHz - RadioMeteors March 2022**  
**daily totals of reflections longer than 10 seconds**  
*Felix Verbelen (Kamphenhout)*



**49.99MHz - RadioMeteors March 2022**  
**daily totals of reflections longer than 1 minute**  
*Felix Verbelen (Kamphenhout)*

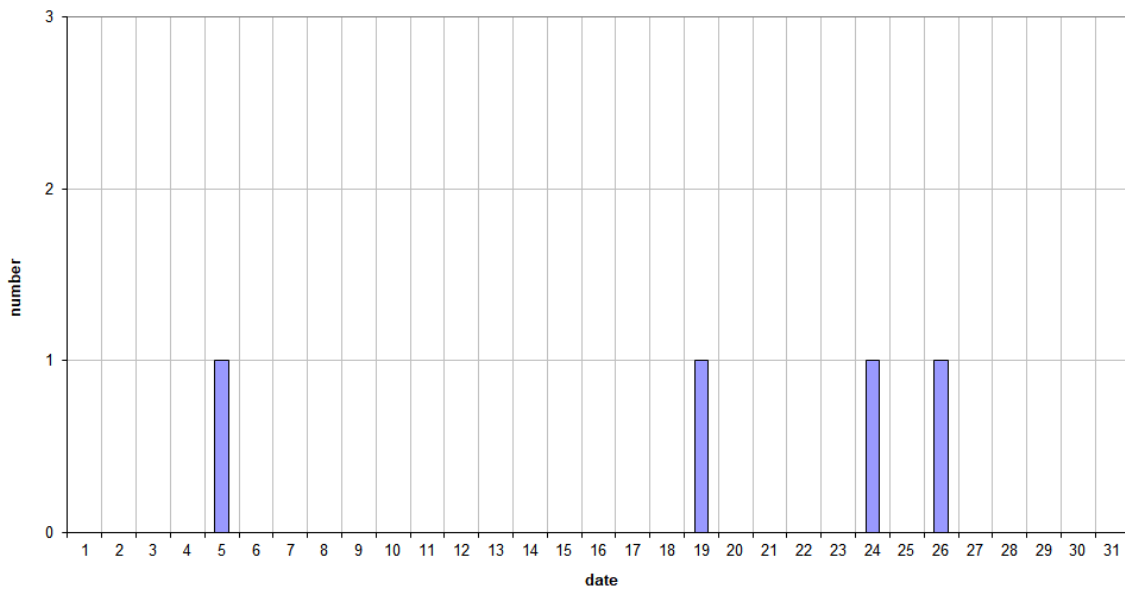


Figure 2 – The daily totals of overdense reflections longer than 10 seconds and longer than 1 minute, as observed here at Kamphenhout (BE) on the frequency of our VVS-beacon (49.99 MHz) during March 2022.

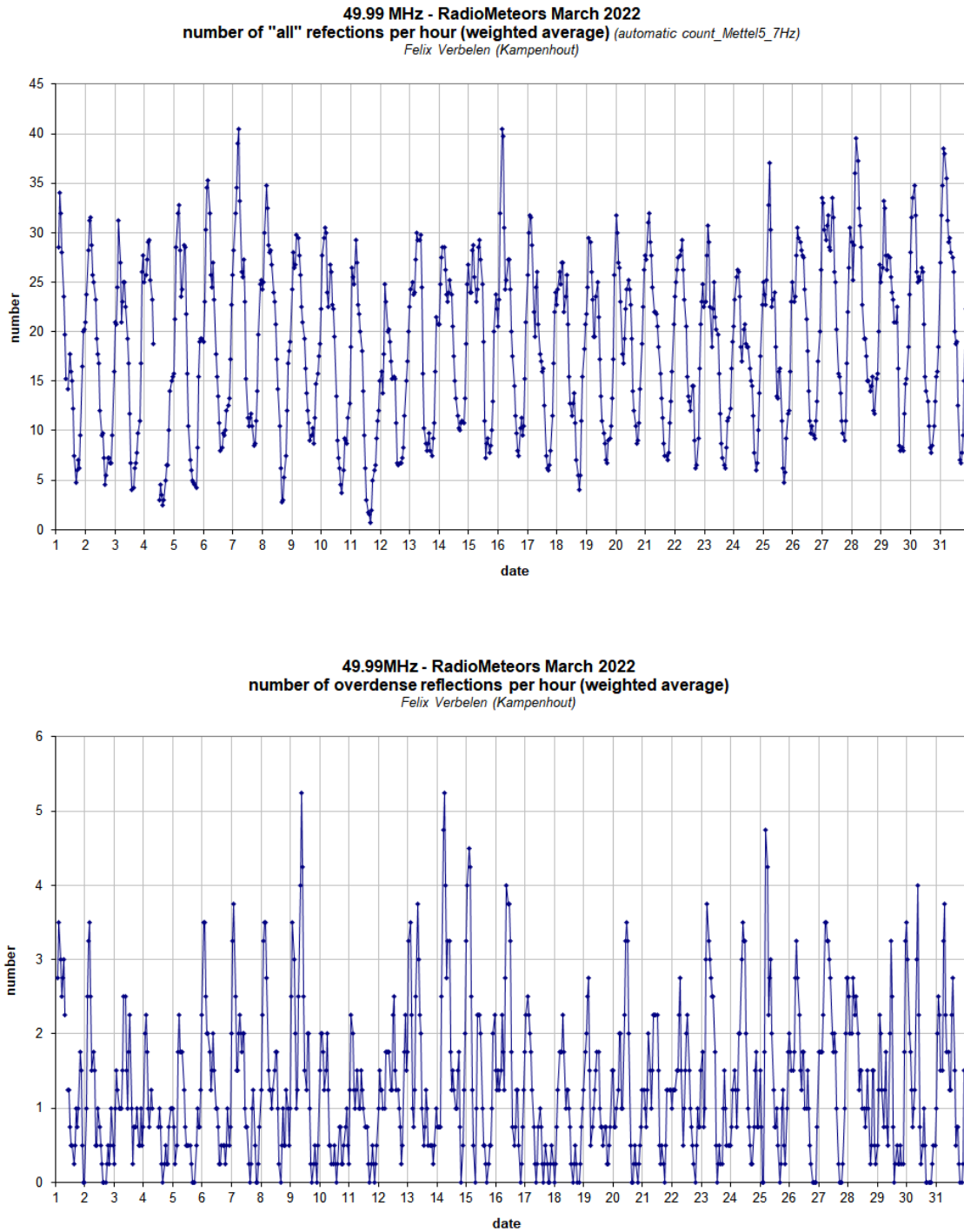


Figure 3 – The hourly numbers of “all” reflections counted automatically, and of manually counted “overdense” reflections, as observed here at Kamphenhout (BE) on the frequency of our VVS-beacon (49.99 MHz) during March 2022.

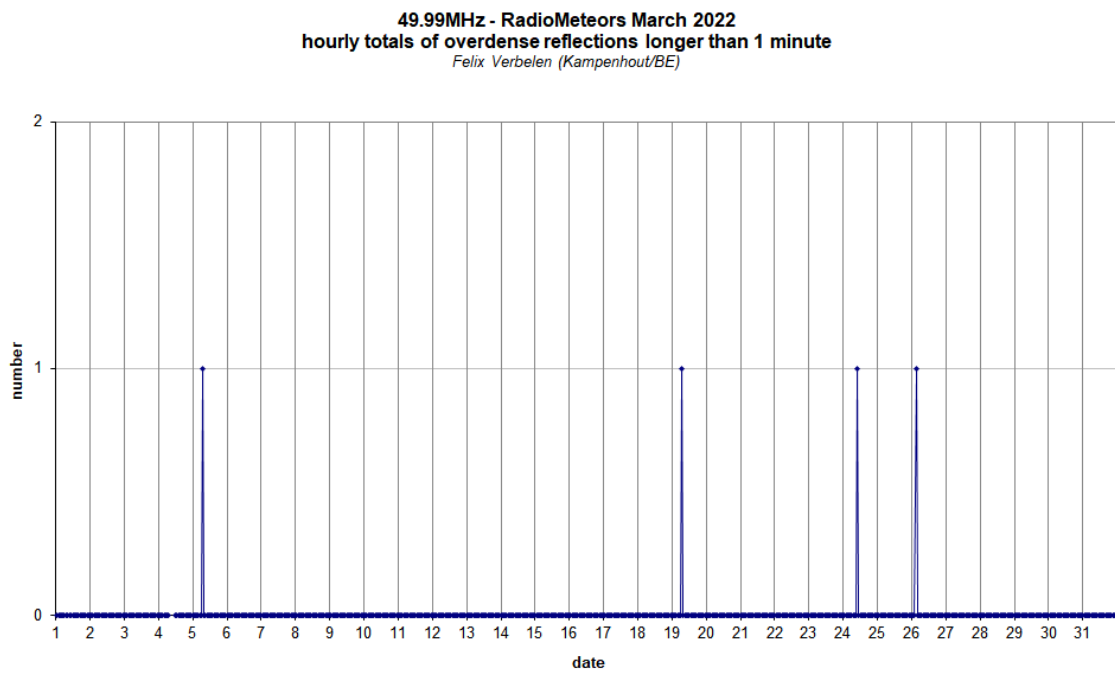
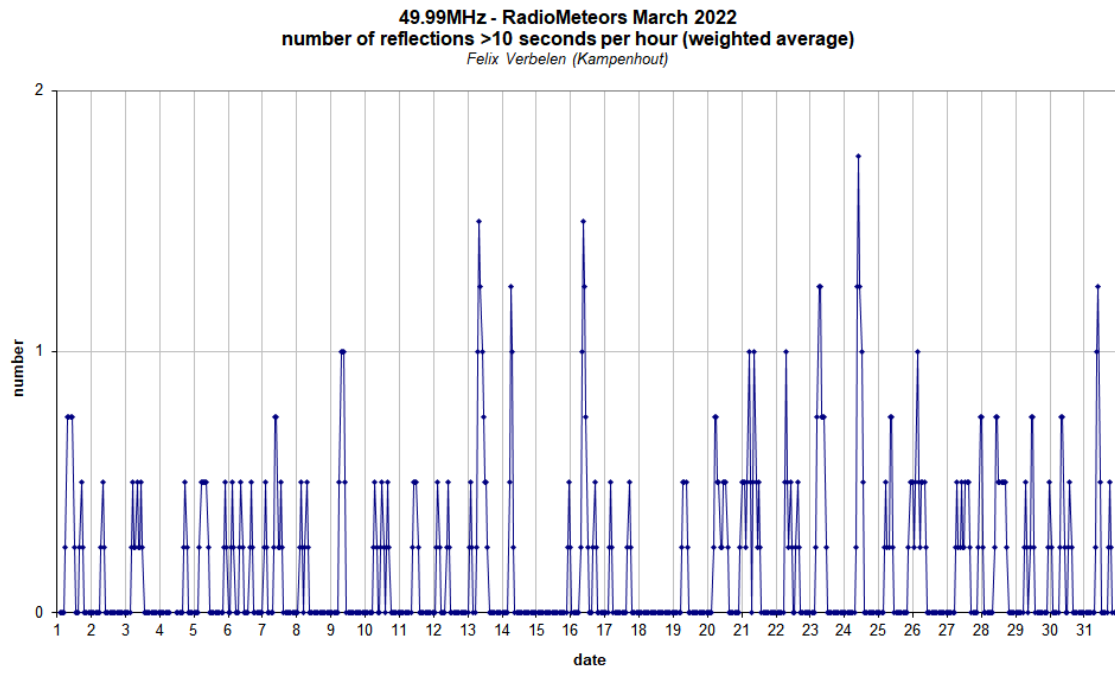


Figure 4 – The hourly numbers of overdense reflections longer than 10 seconds and longer than 1 minute, as observed here at Kamphenhout (BE) on the frequency of our VVS-beacon (49.99 MHz) during March 2022.

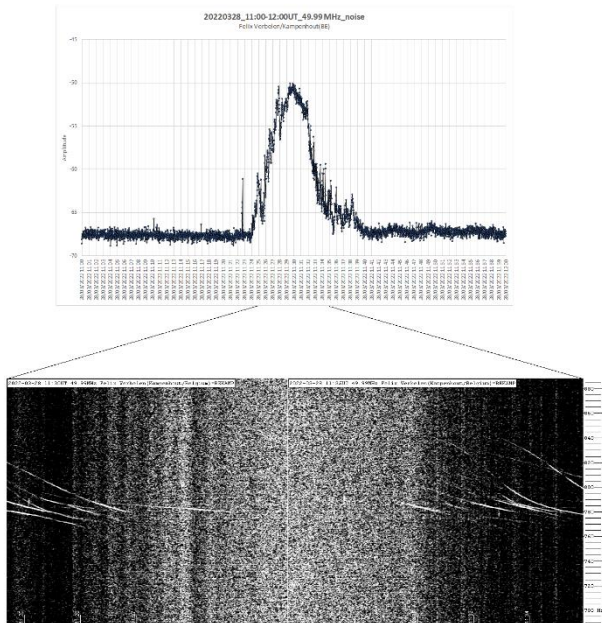


Figure 5 – Solar eruption 28 March 2022.

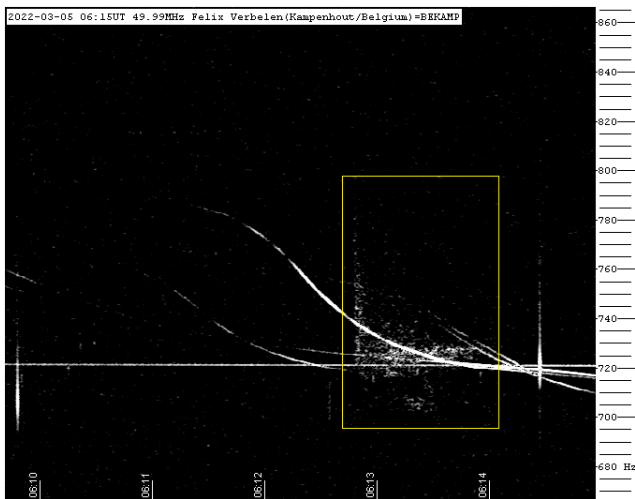


Figure 6 – Meteor reflection 5 March 2022, 06<sup>h</sup>15<sup>m</sup> UT.

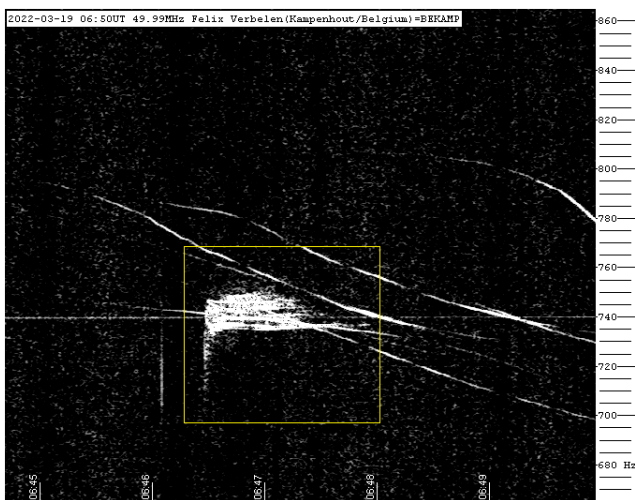


Figure 7 – Meteor reflection 19 March 2022, 06<sup>h</sup>50<sup>m</sup> UT.

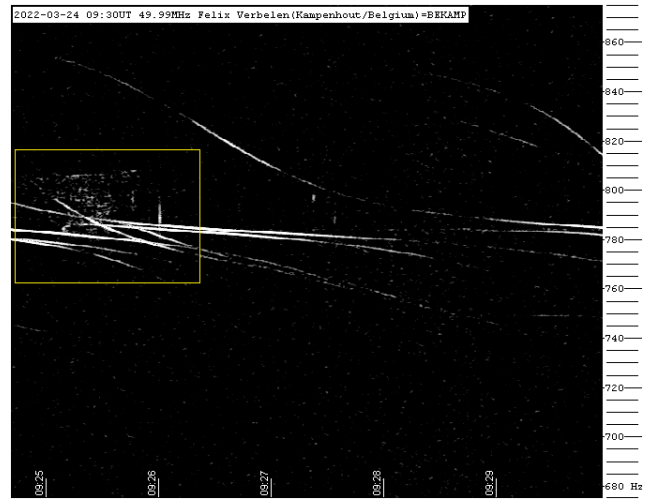


Figure 8 – Meteor reflection 24 March 2022, 09<sup>h</sup>30<sup>m</sup> UT.

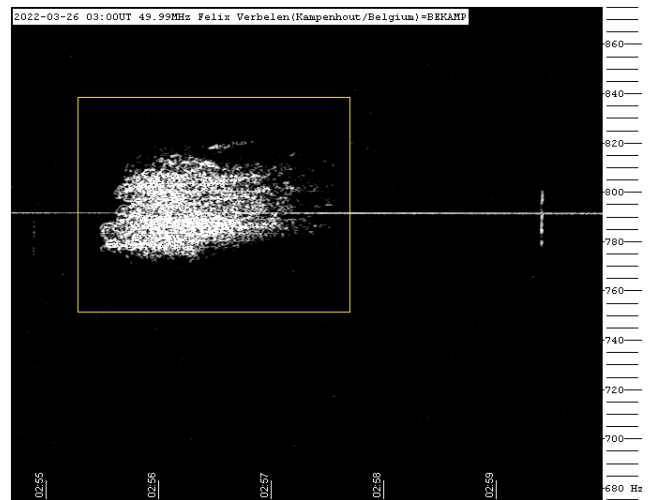


Figure 9 – Meteor reflection 26 March 2022, 03<sup>h</sup>00<sup>m</sup> UT.



The mission of MeteorNews is to offer fast meteor news to a global audience, a swift exchange of information in all fields of active amateur meteor work without editing constraints. MeteorNews is freely available without any fees. To receive a notification: <https://www.meteornews.net/newsletter-signup/>

You are welcome to contribute to MeteorNews on a regular or casual basis, if you wish to. Anyone can become an author or editor, send an email to us. For more info read: <https://meteornews.net/writing-content-for-emeteornews/>

MeteorNews account manager: Richard Kacerek [rickzkm@gmail.com](mailto:rickzkm@gmail.com).

The running costs for website hosting are covered by a team of sponsors. We want to thank the 2022-2023 sponsors: Anonymous (3x), Mikhail Bidnichenko, Gaetano Brando, Trevor C, Nigel Cunnington, Paul Hyde, K. Jamrogowicz, Dave Jones, Richard Kacerek, Richard Lancaster, Joseph Lemaire, Mark McIntyre, Hiroshi Ogawa, Paul Mohan, Lubos Neslusan, BillR, Whitham D. Reeve, John Schlin, Ann Schroyens and Denis Vida.

Financial support is still needed and welcome:  
[https://www.justgiving.com/crowdfunding/meteor-news?utm\\_term=JJBjmJpzV](https://www.justgiving.com/crowdfunding/meteor-news?utm_term=JJBjmJpzV)

### **Contributing to this issue:**

- *Aceituno J.*
- *Aimee A.I.*
- *Ávila D.*
- *Betzler A. S.*
- *Cambell-Burns P.*
- *de Guindos E.*
- *de Sousa O. F.*
- *Gómez-Hernández B.*
- *Gómez-Martínez J.*
- *Greaves J.*
- *Izquierdo J.*
- *Johannink C.*
- *Kacerek R.*
- *Madiedo J. M.*
- *Ortiz J. L.*
- *Palacián J.*
- *Roggemans P.*
- *San Segundo A.*
- *Santos-Sanz P.*
- *Tosar B.*
- *Verbelen F.*
- *Vida D.*
- *Yanguas P.*

---

ISSN 2570-4745 Online publication <https://meteornews.net>

Listed and archived with ADS Abstract Service: <https://ui.adsabs.harvard.edu/search/q=eMetN>

#### **MeteorNews Publisher:**

Valašské Meziříčí Observatory, Vsetínská 78, 75701 Valašské Meziříčí, Czech Republic

---